The Dissertation Committee for Heonjoo Ha certifies that this is the approved version of the following dissertation:

Functional Polymer/Graphene Oxide Composites
Synthesis, Characterization and Applications

Committee:

Christopher J. Ellison, Supervisor

Carlton G. Willson

Benny D. Freeman

Deji Akinwande

Functional Polymer/Graphene Oxide Composites
Synthesis, Characterization and Applications

by

Heonjoo Ha, B.S.; M.S.

Dissertation

Presented to the Faculty of the Graduate School of

The University of Texas at Austin

in Partial Fulfillment

of the Requirements

for the Degree of

Doctor of Philosophy

The University of Texas at Austin

August 2016

Dedication

To my family and all those who have helped

Acknowledgements

During my time in the University of Texas at Austin, I have had the privilege of collaborating with many talented people, and these experiences have influenced me personally and professionally in ways that I will not forget. I would like to start by thanking my advisor, Christopher J. Ellison for his guidance and encouragement. A true advisor is someone who wants nothing more than to help students stand on their own. I am very grateful to meet such an advisor who gave me strength and courage during my Ph.D. studies. I would also like to thank the committee members for their valuable time and advice during my time at the University of Texas at Austin. I would like to further thank Dr. Freeman, Dr. Nagai, Dr. Milliron, and Dr. Yu for allowing me to collaborate with their group and publish great papers together. All of them have been invaluable to my career.

I would like to specially thank my father, Dr. KiRyong Ha, for his expertise in FTIR analysis and all of the advice he gave me to fulfill my studies. He was always there to help me and has given many important suggestions for all of my projects. I am very grateful to have such a polymer expert as my family member. My Ph.D. years would have not been possible without the financial support from Kwanjeong Educational Foundation. They have supported my stipend that has given me many advantages compared to others, and I am thankful for their support.

I have enjoyed working with all of the past and present Ellison group members during my stay in Austin. Many thanks to Dr. Dustin Janes, Dr. Kadhir Shanmuganathan, Dr. Sateesh Peddini, Dr. Amanda Jones, Dr. Zhenpeng Li, Dr. Joon Hee Cho, Yunping Fei, Sunshine Zhou, Dr. Yichen Fang, Chae Bin Kim, Reika Katsumata, Melanie

Merrick, Alysha Helenic, and Han Xiao for their opinions on my research. Additional thanks go to my collaborators, Dr. Amita Joshi, Dr. Jong Wook Kim, Ye Shi, Wontae Joo, Jaesung Park, and Shota Ando for their enthusiasm and support in publishing many papers together.

Finally, I would like to thank my parents for their encouragement and my wife, Ji Young Hwang for always being there for me without any complaints. She made me live every moment, and will always be my companion, my inspiration. I would like to thank my daughter, Mina Ha, for simply coming into my life.

Functional Polymer/Graphene Oxide Composites
Synthesis, Characterization and Applications

Heonjoo Ha, Ph.D.

The University of Texas at Austin, 2016

Supervisor: Christopher J. Ellison

Polymer nanocomposites have been identified as a growth area for the last several decades. The synergy between inorganic and organic compounds has played a major role in developing advanced functional materials for many emerging applications, including enhancing physical/chemical properties of base polymers, replacing metal counterparts, and introducing new energy storage materials, among others. While a number of carbon based nanoparticles have been considered as nanofiller material, significant research effort has been devoted to studies on graphene and its graphene oxide (GO) or reduced graphene oxide (rGO) derivatives.

Graphenes are 2D sheets of carbonaceous material that possess extraordinary mechanical properties, thermal and electrical conductivities, and high surface area. However, most of the methods that have been developed to mass produce graphenes often require costly and tedious purification, along with associated high energy consumption, to achieve the most attractive forms of the material. One of the solutions to reduce the cost of synthesizing graphene while preserving its excellent properties is to use a precursor such as GO. While preparing GO, GO sheets can be functionalized with numerous reactive groups including carboxylic acids, hydroxyls, and epoxides that can be exploited for materials design.

The work in this thesis outlines the synthesis of functional polymer/GO composites by utilizing secondary interactions, such as hydrogen bonding and π-π interactions, and covalent bonds between functional polymer and GO sheets. To understand the impact of these approaches, a fundamental investigation directed towards characterizing various chemical and physical properties for a range of GO-containing materials is discussed in full detail. In addition, different functional polymer/GO composites proposed in this work are evaluated for their utility in a number of different applications. Finally, it is expected that these composite materials will be cost-effective, commercially relevant and reasonable to scale-up for mass production. Therefore, this research will not only contribute to enriching fundamental knowledge but it also has potential to impact society and the economy.

Table of Contents

List of Tables

List of Figures

Chapter 1: Introduction and Background

1.1. Background and Significance

Significant research effort in the last several decades has been devoted to studies on polymer nanocomposites [1]. The synergy between inorganic and organic compounds has played a major role in developing advanced functional materials for many emerging applications by enhancing physical/chemical properties of base polymers, replacing metal counterparts, and introducing new energy storage materials, among others. A number of carbon based nanoparticles of various forms, such as carbon black (CB), buckminsterfullerene (fullerene), carbon nanotubes (CNTs), graphene and its graphene oxide (GO) or reduced graphene oxide (rGO) derivatives (see Figure 1.1 for schematic images of various carbon materials), have been incorporated within many different polymer matrices. While the fundamentals regarding mechanical and electrical property enhancements of composite materials have been well-studied, a comprehensive understanding of the fundamental science of interactions between functional polymers and carbon materials, as well as the tunability of various properties by tailoring the chemical or secondary interactions in these systems have not been fully elucidated. Additionally, there still remains a need for reducing costs and developing eco-friendly, simple fabrication methods that could further stimulate mass production and drive widespread commercialization. These aspects are particularly critical, otherwise replacing existing materials in applications will not become a reality.

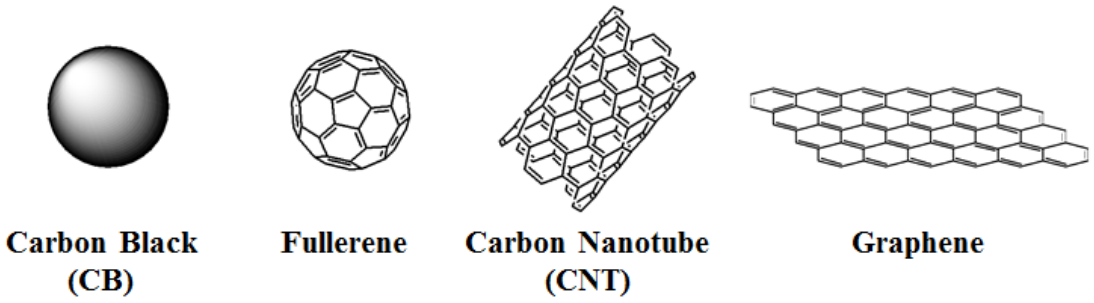

Figure 1.1. Carbon nanomaterials incorporated in polymer nanocomposites.

Therefore, this thesis outlines research directed towards methods to synthesize highly functional materials that incorporate carbon nanomaterials by developing fundamental understanding of the chemical nature of each component and engineering optimized combinations, ideally to realize synergistic properties. In this study, the main focus will be on triggering chemical (covalent bonds) and secondary interactions (such as hydrogen bonds and π-π interactions) between polymers and carbon-based nanofillers in order to synthesize a composite material that can be used in applications such as sensors, oil absorbers and gas barrier/separation membranes, etc.

1.2. Graphene and Graphene Oxide

Among a variety of choices for the nanofiller portion of a nanocomposite, graphene and GO has been very widely studied in the past decade. Figure 1.2 depicts the number of publications related to carbon nanomaterials for the past decade. Since the discovery of graphene in 2004 [2], studies related to graphene have been growing exponentially and it is expected to continue in 2016.

Graphenes are 2D sheets of carbonaceous material that possess extraordinary mechanical properties, thermal and electrical conductivities, and high surface area [2,3]. However, most of the methods that have been discovered to mass produce graphenes often require costly and tedious purification, along with associated high energy

consumption to achieve the most attractive forms of the material [4,5]. One of the solutions to reduce the cost of synthesizing graphene while preserving its excellent properties is to use an oxidized precursor such as GO. GO is commonly prepared using the modified Hummers's method, which combines chemical functionalization with physical exfoliation through vigorous stirring or sonication of high purity graphite precursors [6]. Through this process, the resulting GO sheets can be functionalized with numerous reactive groups including carboxylic acids, hydroxyls, and epoxides [7], that can be exploited in other reactions. A schematic view of graphene and GO is presented in Figure 1.3.

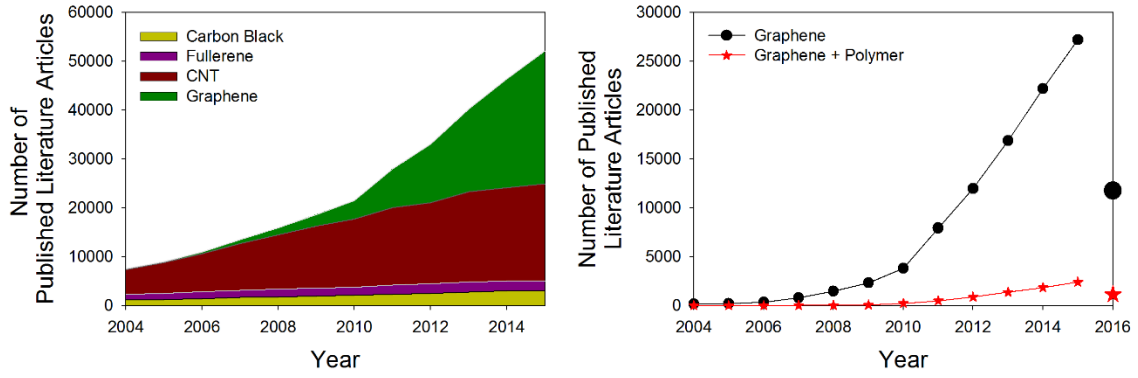

Figure 1.2. (Left) Annual number of published literature articles related to carbon nanomaterials from 2004 to 2015. (Right) Annual number of published literature articles related to 'graphene' and 'graphene' with 'polymer'. 2016 values are numbers as of June 7th. All the numbers have been collected from topical searches in Web of Science.

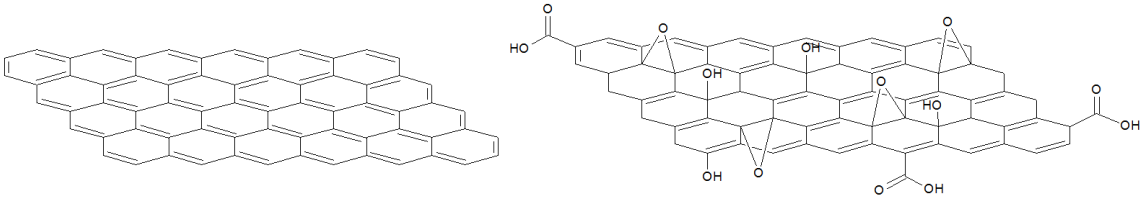

Figure 1.3. (Left) Structural model of graphene and (Right) GO.

1.3. TRANSFORMING GRAPHENE OXIDE TO REDUCED GRAPHENE OXIDE

An additional step in the chemical processing of graphite is often implemented to reduce the resulting GO to form so-called rGO using chemical agents such as hydrazine [8], hydriodic acid (HI) [9], ascorbic acid [10], and heat [11], etc. Due to the extensive oxidation of the graphite during the Hummer's method, GO is generally not electrically conductive and it possesses other properties that differ from pristine graphene (see Figure 1.5) [12]. However, it is possible to partially restore the electrical conductivity and other properties bringing them closer to pristine graphene by reducing GO to rGO. In fact, it is possible to continuously tune the electrical/thermal conductivity, optical properties, hydrophobicity, etc. by carefully controlling the chemistry (i.e., degree of oxidation) of the graphene derivative sheets. A major focus of this thesis research is directed towards exploiting the residual functional groups in GO or rGO such that a range of new nanocomposite systems can be generated. This work revealed that a wide range of properties (e.g., densities ranging from 5 mg/cm^3 to 1.2 g/cm^3, dense and foamed materials, electrically conductive and insulating materials, etc.) can be realized by simply tailoring specific covalent and/or secondary bonds between the polymer and GO or rGO components.

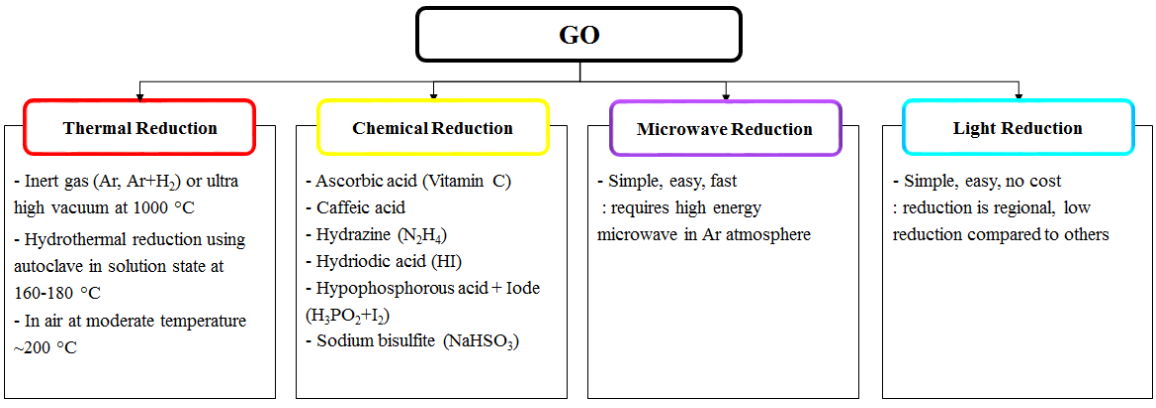

Figure 1.4. Summary of methods to convert GO to rGO.

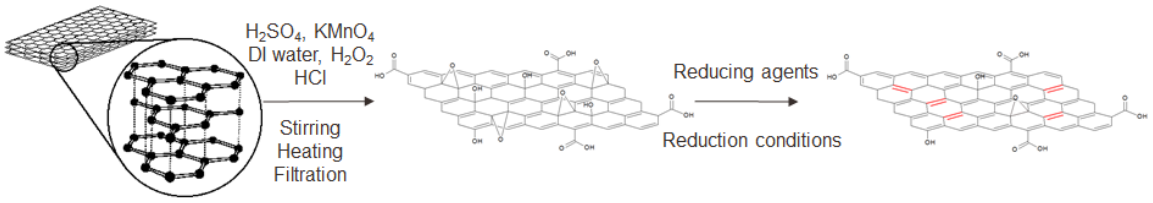

Graphite	**Graphene oxide**	**Reduced graphene**
Stacked **graphenes**	(GO)	**oxide** (rGO)
Conductive	Insulating	Conductive
Hydrophobic	Hydrophilic	Hydrophobic

Figure 1.5. Comparing the properties of GO and rGO.

1.4. SUMMARY

This study aims to synthesize functional polymer/GO composites for use in various applications, such as temperature/pressure sensors, repositionable adhesives, oil absorbers, gas barrier/separation membranes, etc. This wide range of applications is possible due to the unique chemical and physical properties of GO and rGO, such as high electrical conductivity and mechanical integrity, in combination with the processability and versatility of polymers. To make these objectives feasible, strategies to effectively disperse GO, reduce GO, and utilize a range of specific interactions (see Figure 1.6) between polymers and GO or rGO will be discussed. In addition, strategies to optimize the content of polymer and graphene nanofiller to obtain a range of interesting and useful materials, from solid gels to ultra-lightweight aerogels, will be introduced as well. Finally, the approaches developed as part of this thesis are simple and straightforward producing composite materials that are likely to be cost-effective, commercially relevant and reasonable to scale-up for mass production. Therefore, this research has the potential to not only contribute to enriching fundamental knowledge but it also has potential to impact society and the economy.

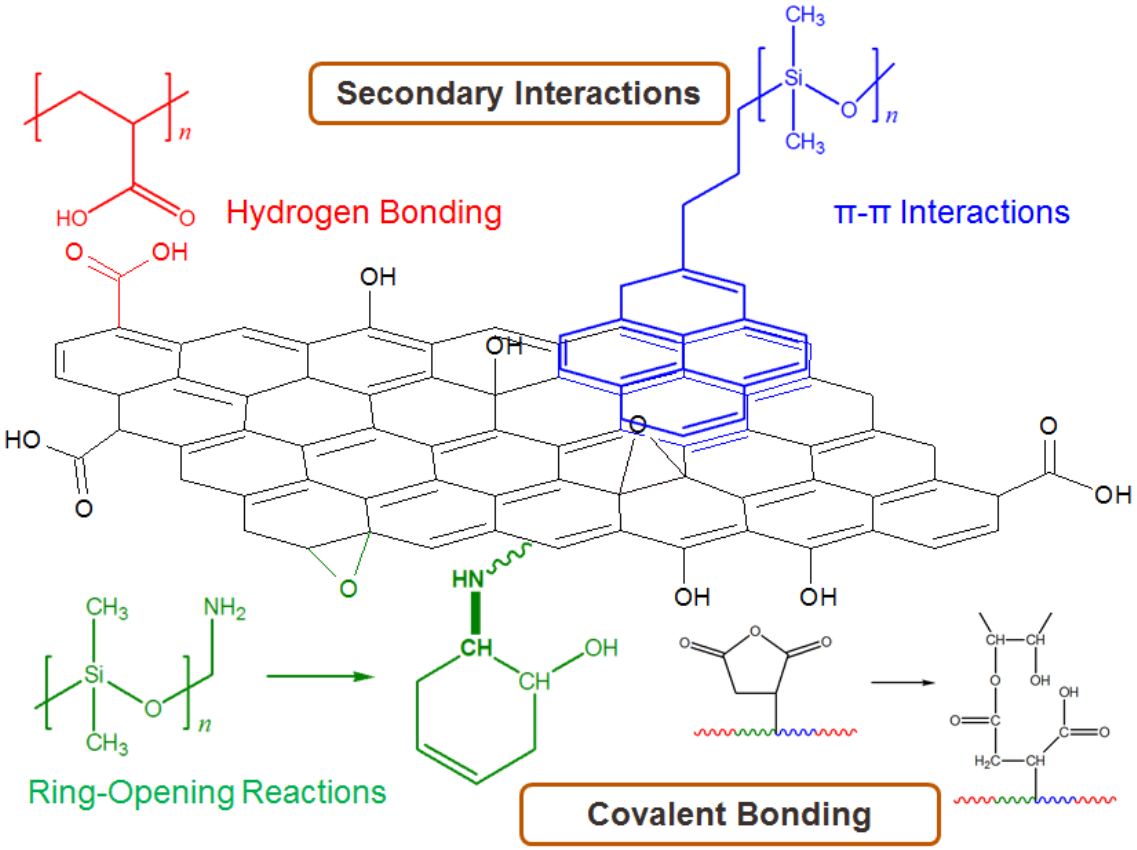

Figure 1.6. Possible routes to synthesize functional polymer/GO composites.

This dissertation contains a total of six Chapters, including the Introduction. Chapter 2 outlines methods for synthesizing thermally crosslinked poly(acrylic acid)/rGO aerogels along with mechanical property characterization and discussion of their potential utility in applications. In Chapter 3, the synthesis of several pyrene end-labeled poly(dimethylsiloxane) materials is presented followed by an investigation of their thermal stimuli-responsive behavior and utility in GO composite materials. The synthesis and gas permeability of highly elastic telechelic poly(dimethylsiloxane)/GO composite elastomers are presented in Chapter 4. Chapter 5 presents the gas transport properties of telechelic poly(dimethylsiloxane)/GO composites by systematically studying their gas transport behavior as a function of GO concentration. Analysis of experimental data with

various models, combined with an investigation of each sample's morphology and gas transport properties, are also discussed in this chapter. In the final chapter, the major conclusions from this thesis are presented, along with recommendations for future work.

1.5. REFERENCES

[1] Paul DR, Robeson LM. Polymer nanotechnology: Nanocomposites. Polymer (Guildf) 2008;49:3187–204. doi:10.1016/j.polymer.2008.04.017.

[2] Novoselov KS, Geim AK, Morozov S V, Jiang D, Zhang Y, Dubonos S V, et al. Electric field effect in atomically thin carbon films. Science 2004;306:666–9. doi:10.1126/science.1102896.

[3] Geim AK, Novoselov KS. The rise of graphene. Nat Mater 2007:183–91. doi:http://dx.doi.org/10.1038/nmat1849.

[4] Chabot V, Higgins D, Yu A, Xiao X, Chen Z, Zhang J. A review of graphene and graphene oxide sponge: material synthesis and applications to energy and the environment. Energy Environ Sci 2014;7:1564. doi:10.1039/c3ee43385d.

[5] Zurutuza A, Marinelli C. Challenges and opportunities in graphene commercialization. Nat Nanotechnol 2014;9:730–4. doi:10.1038/nnano.2014.225.

[6] Ha H, Shanmuganathan K, Ellison CJ. Mechanically Stable Thermally Crosslinked Poly(acrylic acid)/Reduced Graphene Oxide Aerogels. ACS Appl Mater Interfaces 2015;7:6220–9. doi:10.1021/acsami.5b00407.

[7] Dreyer DR, Park S, Bielawski CW, Ruoff RS. The chemistry of graphene oxide. Chem Soc Rev 2010;39:228–40. doi:10.1039/b920539j.

[8] Stankovich S, Dikin D a., Piner RD, Kohlhaas K a., Kleinhammes A, Jia Y, et al. Synthesis of graphene-based nanosheets via chemical reduction of exfoliated graphite oxide. Carbon N Y 2007;45:1558–65. doi:10.1016/j.carbon.2007.02.034.

[9] Pei S, Zhao J, Du J, Ren W, Cheng HM. Direct reduction of graphene oxide films into highly conductive and flexible graphene films by hydrohalic acids. Carbon N Y 2010;48:4466–74. doi:10.1016/j.carbon.2010.08.006.

[10] Zhang J, Yang H, Shen G, Cheng P, Zhang J, Guo S. Reduction of graphene oxide via L-ascorbic acid. Chem Commun (Camb) 2010;46:1112–4. doi:10.1039/b917705a.

[11] Yang D, Velamakanni A, Bozoklu G, Park S, Stoller M, Piner RD, et al. Chemical analysis of graphene oxide films after heat and chemical treatments by X-ray photoelectron and Micro-Raman spectroscopy. Carbon N Y 2009;47:145–52. doi:10.1016/j.carbon.2008.09.045.

[12] Dikin DA, Stankovich S, Zimney EJ, Piner RD, Dommett GHB, Evmenenko G, et al. Preparation and characterization of graphene oxide paper. Nature 2007;448:457–60. doi:10.1038/nature06016.

Chapter 2: Mechanically Robust Thermally Crosslinked Poly(acrylic acid)/Graphene Oxide Aerogels[1]

2.1. OVERVIEW

The first attempt at synthesizing functional polymer/GO composites focused on utilizing both hydrogen bonding interactions and chemical crosslinking between poly(acrylic acid) (PAA) and GO in the form of an aerogel. GO aerogels, high porosity (> 99%) low density (~3-10 mg/cm^3) porous materials with GO pore walls, are particularly attractive due to their light weight, high surface area and potential use in environmental remediation, super-hydrophobic and super-oleophilic materials, energy storage, etc. However, pure GO aerogels are generally weak and delicate which complicates their handling and potentially limits their commercial implementation. The focus of this work was to synthesize highly elastic, mechanically robust aerogels that are easy to handle without substantially sacrificing their high porosity or low density. To overcome this challenge, a small amount of readily available and thermally crosslinkable PAA was intermixed with GO to enhance the mechanical integrity of the aerogel without disrupting other desirable characteristic properties. This method is a straight-forward procedure that does not include multistep or complicated chemical reactions and it produces aerogels that can reversibly support up to 10,000 times their weight with full recovery of their original volume. Finally, pressure sensing capabilities were demonstrated and their oil absorption capacities were measured to be around 120 g oil/g aerogel which highlights their potential use in practical applications.

[1] Ha H (Designed and performed experiments, wrote and edited the paper), Shanmuganathan K, Ellison CJ. Mechanically Stable Thermally Crosslinked Poly(acrylic acid)/Reduced Graphene Oxide Aerogels. ACS Appl Mater Interfaces 2015;7:6220–9. doi:10.1021/acsami.5b00407.

2.2. INTRODUCTION

Converting GOs or rGOs into a low density, highly porous co-continuous 3D network with physical and chemical crosslinks has been of significant interest for the past few years [1,2]. These high surface area materials have mass densities of ~3-10 mg/cm^3 with porosities > 99% and are usually referred as GO sponges, aerogels, or aerographites. Unfortunately, these aerogels are often found to be extremely weak and delicate to handle due to the weak van der Waals interactions between adjacent graphene sheets that leads to a brittle skeleton [1,2]. To improve the mechanical properties of the aerogel, small amounts of additives, such as CNTs or ethylenediamine (EDA) [3,4], which can form secondary interactions with the GO sheets, have been incorporated. An alternative approach is to introduce chemical crosslinks to the system that can effectively reinforce the mechanical properties of the delicate aerogels. However, it is critical to limit the amount of non-GO material that is used to enhance the mechanical properties of the aerogel; two potential consequences of "diluting" the GO are pore structure collapse and attrition of other desirable properties of the aerogel. Furthermore, the chemical crosslinking reactions must occur after the aerogels are formed or simultaneously during aerogel formation, to reduce the possibility of damage or disruption of the structure of the GO aerogels.

Recently, Hong et al. [5], successfully demonstrated a highly durable and elastic GO aerogel by taking advantage of the self-assembly of poly(vinyl alcohol) using glutaraldehyde as a chemical/covalent crosslinker for this polymer. This study achieved excellent compressibility and good performance of the aerogel as an electrochemical capacitor, which was one of the first published uses of polymers as mechanical property enhancers in GO aerogels. However, the density of their material was relatively high

(~10 mg/cm^3) and the preparation steps accompanied several chemical reaction procedures which could complicate mass production.

Herein, we describe a new strategy to overcome the limitations of brittle all-GO aerogels by intermixing a small amount of readily available and thermally crosslinkable PAA. This strategy is capable of greatly enhancing the mechanical properties while simultaneously maintaining all other attractive properties (i.e., high porosity, electrical conductivity, low density, high surface area, etc.) of the GO aerogels. This is a low cost, simple and straight-forward approach that does not include complicated or multistep chemical reactions. We report here the general approach that was developed, along with the effect of molecular weight and concentration of the thermally crosslinkable polymer additive, on the structure and properties of reduced GO aerogels (termed XPAA/rGO aerogels herein). We also demonstrate how the attractive properties of these mechanically robust aerogels can be useful in applications, such as super-absorbents and pressure sensors.

2.3. EXPERIMENTAL SECTION

2.3.1. Materials

Several different PAA samples with viscosity average molecular weights (M_v) of 450,000 and 1,250,000 were purchased from Sigma-Aldrich and used without any further purification. 55% HI solution was chosen as the reducing agent for GOs, and was purchased from Sigma-Aldrich. Sulfuric acid, potassium permanganate, hydrogen peroxide, and hydrochloric acid to prepare GO from preoxidized graphite were purchased from Fisher Scientific and used as-received. Preoxidized graphite from Bay Carbon Inc. (SP-1) was used to prepare GO.

2.3.2. Preparation of GO

GO was synthesized according to the Hummer's method with slight modification as described in detail elsewhere [6]. Briefly, preoxidized graphite (5 g) was added to concentrated sulfuric acid (98 %, 125 ml) in an ice bath. Potassium permanganate (15 g) was added slowly using a spatula with vigorous stirring of the solution. The mixture was stirred at 35 °C for 2 hours. Then, deionized water (DI water, 230 ml) was carefully added using a pipet followed by terminating with DI water (700 ml) and 30% hydrogen peroxide solution (12.5 ml). Dilute hydrochloric acid solution with DI water in a volume ratio of 1:10 were used to remove residual manganese salt and excess acid products. Subsequently, the solution was washed with DI water until the pH of the rinsed water reached neutral. Finally, this solution was filtered using a vacuum assisted Büchner funnel and the filtrate converted into a thick slurry of GO in water. The aqueous dispersion of GO was lyophilized under vacuum for later use.

2.3.3. Preparation of PAA/GO Aerogels

The GO to PAA ratio for all of the samples prepared in this study are represented as the relative weight percentage of PAA to 100 parts GO. For example, 450 kDa/25 indicates PAA having a viscosity average molecular weight of 450 kDa was used in a weight ratio of GO to PAA of 100:25. The corresponding amount of PAA was added to DI water (10 ml) using a 20 ml scintillation vial at room temperature for 12 hours with vigorous stirring. After confirming complete dissolution of PAA in DI water, dried GO (50 mg) was added to the solution to make a 5 mg GO/ml concentrated solution. Additional stirring using a stir bar was performed for 2 hours and then the solution was sonicated using a 400 W probe sonicator (Branson Digital Sonifier 450) with 10 % amplitude for 10 minutes (24 kJ) in an ice bath. This process assisted in the complete exfoliation of GO in DI water and homogeneously mixed GO with PAA throughout the

solution. After sonication, the solution was transferred to a 15 ml plastic vial with a wide open neck using a glass pipet. This solution was freeze-dried by immersing into liquid nitrogen for 2 minutes then pulling vacuum at room temperature for 48 hours. The resulting aerogels (a physical mixture of PAA and GO at this stage) were low density, dark brown spongy-like materials with weak mechanical properties. It is noteworthy that, if the GO was not completely exfoliated during the sonication step and/or if the aerogels were not completely dried during the vacuum step, the aerogels displayed significant shrinkage.

2.3.4. Preparation of XPAA/rGO Aerogels

After obtaining PAA/GO aerogels, all of the materials were removed from the plastic vial and then placed in a glass chamber containing HI vapor at room temperature for 24 hours. Reducing the GO to rGO during this procedure changed the color of the aerogels from dark brown to metallic black. To eliminate the residual HI vapor and simultaneously thermally crosslink PAA to poly(acrylic anhydrides) (XPAA), the resulting rGO aerogels were heated at 160 °C for 24 hours in a vacuum oven.

2.3.5. Characterization of XPAA/rGO Aerogels

Thermal properties of the PAA were characterized by differential scanning calorimetry (DSC; Mettler Toledo DSC1). Heating and cooling rates of 20 °C/min were used for all experiments, and the midpoint value during the second heating curve was used for glass transition temperature (T_g) analysis. The chemical crosslinking reaction of PAA was investigated using attenuated total reflection Fourier transform infrared spectroscopy (ATR-FTIR; Thermo Nicolett 6700). Scanning electron microscopy (SEM; Zeiss Supra 40V) was used to study the morphology of the aerogels and the cycled compression/release mechanical experiments were performed using a rheometer (TA

Instruments AR-2000ex). The rheometer was equipped with a Peltier plate at the bottom and a 40 mm parallel plate at the top. All of the compression/release cycle experiments were performed at room temperature for 10 consecutive cycles with a compression /release speed of 1,000 μm/sec. Since the height of the aerogels differs slightly sample to sample, a constant starting height value of 14,000 μm was set for every experiment. After loading the sample on the Peltier plate, the sample was compressed to 14,000 μm and the normal force was zeroed to eliminate any residual stress present before actual measurements. All of the data for normal stress were recalculated using the exact diameter of the aerogels by multiplying the reported values with the area of the parallel plate and dividing by the actual area of the aerogels. GOs used in this study were further characterized using X-ray diffraction (XRD; Rigaku R-axis Spider) to measure the diffraction of the material, and X-ray photoelectron spectroscopy (XPS; Kratos) to compare the composition of the GOs before and after reduction. CasaXPS software (v 2.3.16) was used to perform curve fitting in which a Shirley background was assumed.

The density and porosity of the aerogels were calculated according to Equation 1 and 2:

$$\varepsilon = (1 - \rho / \rho_0) \times 100 \quad (1)$$

$$\rho_0 = \rho_{0,PAA} \times w_{PAA} + \rho_{0,Graphite} \times w_{GO} \quad (2)$$

where ε is percent porosity, ρ is the mass density of the aerogel sample calculated from the weight of the aerogel divided by the volume, ρ_0 is the theoretical nonporous mass density and w is the weight fraction of each component of the material. The density for graphite and PAA was taken as 2.2 g/cm^3 ($\rho_{0,Graphite}$) and 1.2 g/cm^3 ($\rho_{0,PAA}$), respectively.

Mechanical integrity was tested by holding the sample by hand and attempting to cut the sample with a razor blade and a pair of scissors; mechanically poor samples fractured in a brittle fashion while mechanically robust samples could be cleanly

sectioned all the way through during cutting. Oil absorption performance was conducted by immersing a small portion of aerogel into a large quantity of 6 different oils. The duration of immersion was uniformly held at 2 minutes. After removing the samples from the oil, samples were gently rolled on a piece of filter paper in every direction to get rid of excess oil adhered to the surface of the aerogels. Three consecutive tests were performed and the data are presented as average values with standard deviation as the error bar. Pressure sensor performance was conducted using a LED lamp with two pieces of Cu foil as the electrodes contacting both ends of the aerogels. The resistivity of the material as a function of % compressive strain was measured using a rheometer (TA Instruments AR-2000ex). A multimeter (Fluke 179 True RMS Multimeter) was used to quantitatively measure the resistivity of the material by placing two pieces of Cu foil attached to glass slides in between the parallel plates of the rheometer and the sample to be tested. The sample was squeezed to different % compressive strains while resistivity measurements were collected.

2.4. RESULTS AND DISCUSSION

In order to fully understand the procedures required to prepare XPAA/rGO aerogels, separate fundamental studies on reducing GO to rGO by HI vapor and thermally crosslinking PAA were first investigated.

2.4.1. Vapor Reduction of GO to rGO

A combination of studies of the GO and rGO aerogels (i.e., no polymer), including solubility in DI water before and after reduction, XRD spectra and XPS spectra, demonstrated the effective reducing capability of HI vapor (quantitatively by XRD and XPS in Figure 2.1 and qualitatively by solubility/hydrophilicity in Figure A.1

at Appendix A). XRD indicating the interlayer spacing of the GO sheets in the GO aerogel (made from freeze drying a thick aqueous slurry of GO), rGO sheets in the rGO aerogel after HI vapor reduction followed by thermal annealing at 160 °C for 24 hours, and as-received preoxidized graphite are compared in Figure 2.1a. The GO aerogel and graphite showed an intrinsic peak of 11° (d-spacing = 8.03 Å) and 26.6° (d-spacing = 3.45 Å), respectively, while the rGO aerogel did not exhibit any peaks [4]. This provides clear evidence that GO could be effectively reduced to rGO by using HI vapor as the reducing agent. Unlike the hydrothermal method that employs high temperature reduction (often autoclave assisted) in an aqueous environment [7], introducing vapor phase reducing agents at ambient pressure can prevent rGOs from restacking through capillary forces and structural mobility facilitated by surrounding water. Notably, reduction of GO to rGO also results in formation of strong π electron interactions between sheets during/following the reduction step that can play an important role in the final structure and mass density of the aerogel.

Furthermore, XPS survey and C 1s spectra peaks show that the oxygen containing groups have been mostly removed by HI vapor (Figure 2.1b to 2.1d). The main oxygen containing components of GO arising from C=O (288.1 eV) and C-O (286.7 eV) groups are significantly reduced, while C=C, C-C (286.4 eV) becomes dominant in rGO, as shown by one single peak with a shoulder at higher binding energy (comparing Figure 2.1c and 2.1d). Given that a small portion of C=O and C-O groups from GO still remain after the reduction step, it is postulated that these residual functional groups (e.g., acid, hydroxyl or epoxide) could allow PAAs to form hydrogen bonds or even covalent bonds with the rGO sheets during subsequent thermal annealing steps. By performing simple water solubility experiments of GO and rGO aerogels (Figure A.1 in Appendix A), the

hydrophilicity of these aerogels were reduced dramatically after reduction, which is in good agreement with the XPS and XRD data in Figure 2.1.

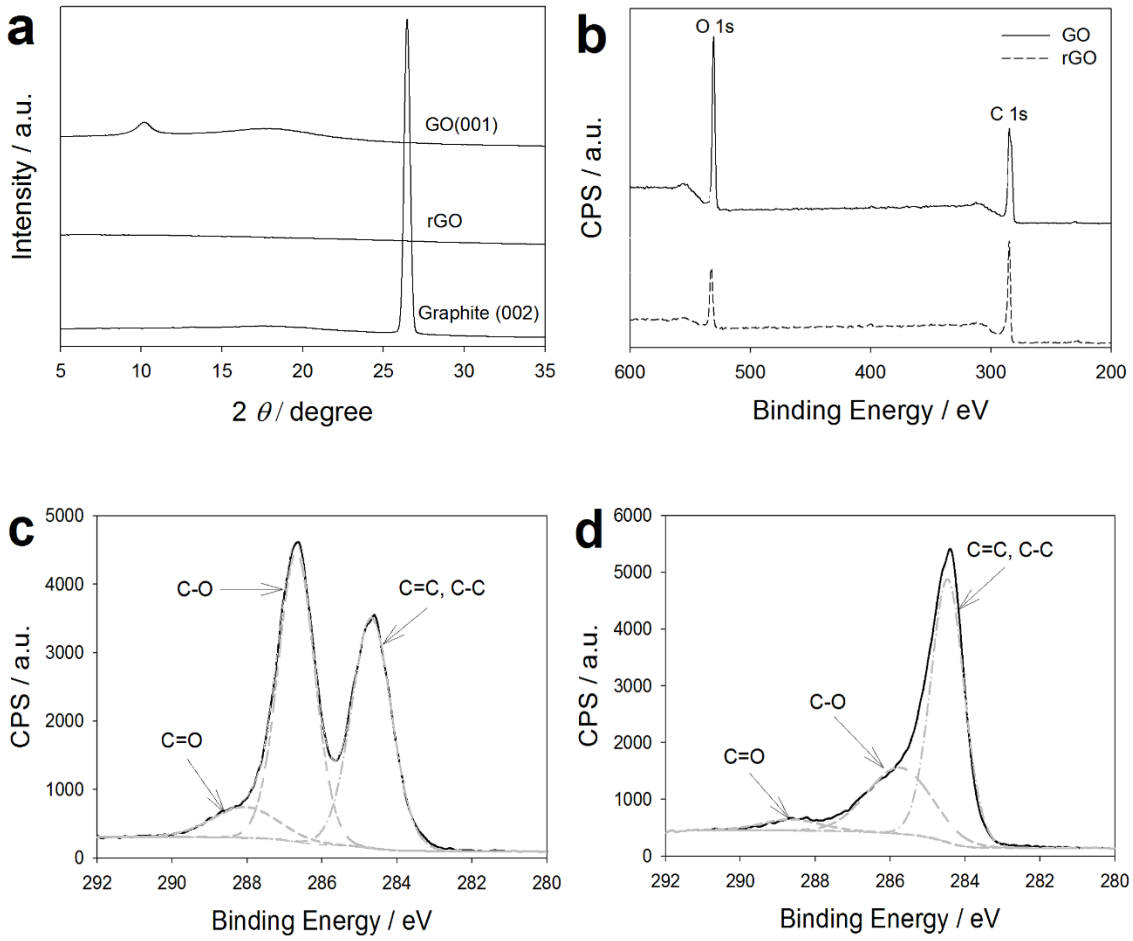

Figure 2.1. (a) XRD spectra of GO and rGO aerogels compared to that of preoxidized graphite. (b) XPS survey and C 1s spectra for (c) GO and (d) rGO after HI reduction and 24 hours at 160 °C in vacuum. Adapted with permission from reference [8]. Copyright 2015 American Chemical Society.

2.4.2. Crosslinking Reaction Kinetics of PAA to XPAA

It has been reported by others that adjacent carboxylic acid groups in PAA can react with each other making intermolecular and intramolecular anhydrides forming

XPAA by simple heating [9,10]. In order to understand the crosslinking reaction/anhydride formation and its kinetics, two different PAA samples with different molecular weights (M_v = 450 kDa and 1,250 kDa) were investigated during thermal annealing at 160 °C in a vacuum oven for up to 24 hours. Figure 2.2 summarizes associated DSC and FTIR data. The crosslinking reactions for 450 kDa PAA were expectedly accompanied by distinctive changes in T_g with annealing time (Figure 2.2a) that occurred rapidly nearing a plateau after ~8 hours of annealing (thermograms shown in Figure 2.2c and calculated T_g values in Table A.1). On the other hand, the high molecular weight 1,250 kDa PAA exhibited a slower reaction (as indicated by T_g) with a much broader range between T_g onset and endset (Figure 2.2b and Table A.1), possibly due to lower polymer mobility associated with higher M_v that could slow migration of nearby acrylic acid groups.

Although the reaction conversion kinetics for PAA can be determined indirectly by DSC, absorbance spectra obtained using FTIR are far more indicative of the chemical changes. As illustrated in Figure 2.2d, 450 kDa and 1,250 kDa PAA both exhibited characteristic peaks of PAA, as expected. Before annealing, peaks associated with carboxylic acid pendent groups, that is, C=O stretching and C-O stretching coupled with O-H bending, were each assigned at 1703 cm^{-1} and 1150-1300 cm^{-1}, respectively. However, after annealing PAA at 160 °C for 24 hours, the position for the carbonyl group (C=O) was broadened and shifted to a higher frequency by ~45 cm^{-1}, while C-O stretching shifted to a lower frequency region at ~900-1200 cm^{-1}. In addition, due to the formation of anhydride linkages during thermal annealing, a new peak appeared at 1820 cm^{-1}, which was assigned to the in-phase C-O stretching of the anhydride [11]. Because the FTIR spectra for the 450 kDa and 1,250 kDa PAA were nearly identical after 24 hours of annealing at 160 °C and the T_g was no longer evolving, it can be concluded that

the reaction was essentially completed for both cases. This reaction endpoint is likely representative of the vanishing mobility of crosslinking reactions as the anhydride formation proceeds rather than achieving 100% anhydride.

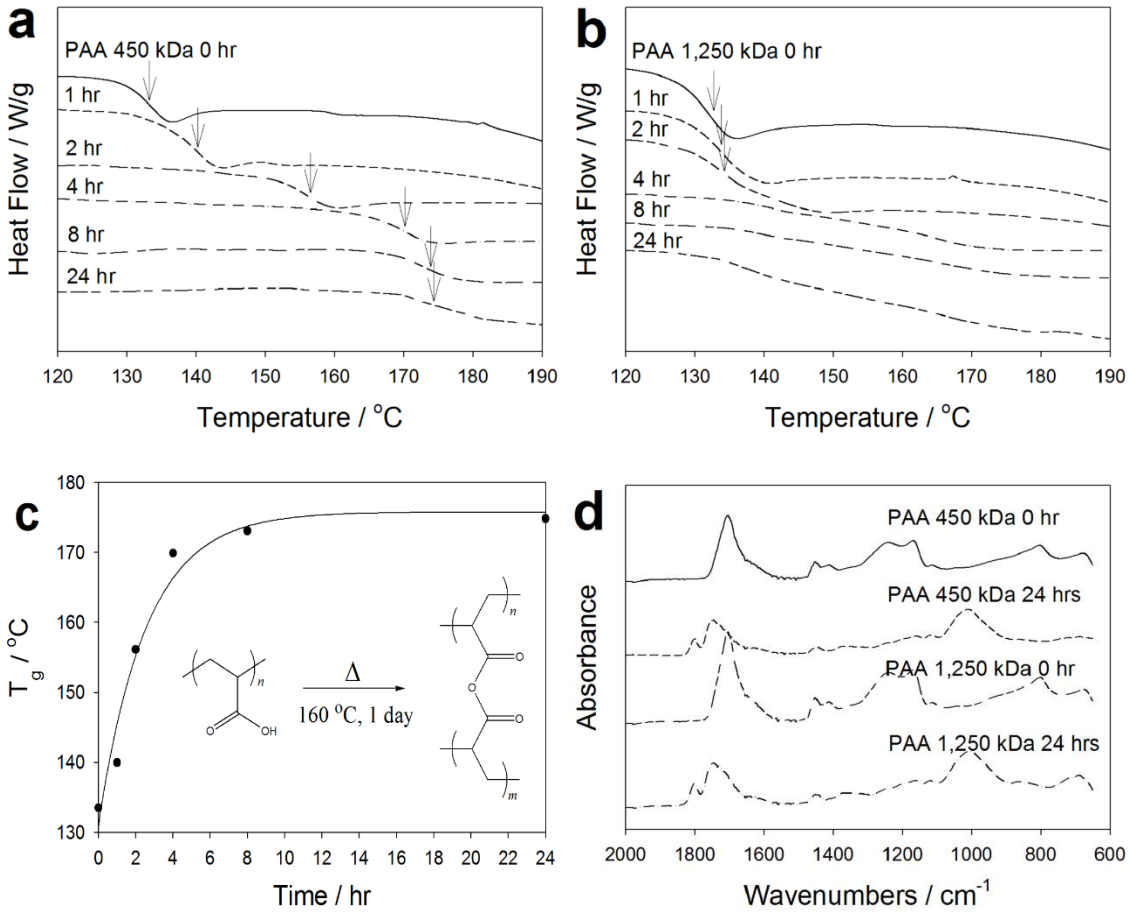

Figure 2.2. DSC curves indicating T_g (arrows) for PAA with M_v of (a) 450 kDa and (b) 1,250 kDa after annealing at 160 °C under vacuum for different times. (c) T_g of 450 kDa PAA depending on the annealing time and (d) FTIR spectra before and after annealing PAA. FTIR spectra and DSC thermograms have been shifted vertically for clarity but are otherwise on the same scale. Adapted with permission from reference [8]. Copyright 2015 American Chemical Society.

2.4.3. Morphology and Properties of XPAA/rGO

Thermally crosslinked PAA/rGO aerogels (called XPPA/rGO aerogels henceforth) were prepared by the simple procedure illustrated in Figure 2.3. Although mechanical properties are improved simply by adding PAA to the GO aerogel precursor, the greatest mechanical property enhancement occurred after the GO was reduced to rGO and the PAA was thermally crosslinked to form XPAA. As discussed earlier, HI vapor reduced a large portion of the GO to rGO. The following thermal annealing process under vacuum not only crosslinks PAA to XPAA, but also slightly further reduced GO to rGO (data not shown). Figure A.2 qualitatively demonstrates the associated changes in hydrophilicity from PAA/GO and XPAA/rGO aerogels, which shows that the hydrophilic PAA/GO aerogels were significantly swollen with water and disintegrated into pieces compared to hydrophobic XPAA/rGO aerogels that remained intact and floating even after submersion in DI water for 24 hours. This result can be explained by both the hydrophobic nature of the rGO compared with that of GO and the crosslinking of PAA. Intermediate stage PAA/rGO samples (i.e., after reduction but before thermal crosslinking) also floated and remained intact because water could not penetrate the hydrophobic rGO porous structure (not shown).

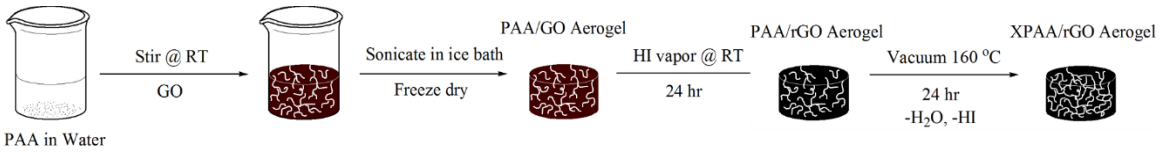

Figure 2.3. Scheme for process of preparing XPAA/rGO aerogels. Adapted with permission from reference [8]. Copyright 2015 American Chemical Society.

Several aspects of the overall process can affect the final porosity and density. For example, the concentration of GO in DI water was fixed at 5 mg/ml to obtain a regular

porous structure after freeze-drying. It has been demonstrated in previous studies [12,13] that this particular structure provides maximum load transfer and mechanical property improvements for GO aerogels; data from the present study confirms this conclusion and is shown in Figure A.3. After successfully converting the PAA/GO aerogels into XPAA/rGO aerogels, the densities (~4.38-6.69 mg/cm^3) and porosities (~99.6-99.8%) of all of the samples prepared for this study demonstrated the effectiveness of the overall process, because the intrinsic low density and high porosity of the aerogels were not adversely affected in any step. It is important to note that forming pure PAA aerogels was not possible and the structures simply collapsed during freeze-drying, possibly due to the mobility of PAA chains in the presence of a good solvent (DI water). A summary of the resulting material's densities and porosities are listed in Table 2.1, as calculated from Equations 1 and 2.

Table 2.1. Calculated density and porosity of the XPAA/rGO aerogels and theoretical nonporous density of the precursor mixture. Adapted with permission from reference [8]. Copyright 2015 American Chemical Society.

Sample	**Theoretical nonporous density**	**Aerogel density**	**Aerogel porosity**
	ρ_0 [g/cm^3]	**ρ [mg/cm^3]**	**ε [%]**
rGO 5 mg/ml	2.20	3.67	99.8
450 kDa/25	2.00	4.38	99.8
450 kDa/50	1.87	5.08	99.7
450 kDa/75	1.77	5.48	99.7
1,250 kDa/25	2.00	4.18	99.8
1,250 kDa/50	1.87	5.12	99.7
1,250 kDa/75	1.77	6.69	99.6

One of the main reasons for using PAA as the reinforcement polymer is not only because PAA is capable of forming thermal crosslinks in a simple thermal annealing

procedure, but also because PAA can exhibit attractive interactions with GO while being completely soluble in DI water. Due to the nature of the hydrophilic carboxylic acid pendent group, PAA can form strong hydrogen bonds with carboxylic acid, hydroxyl and epoxy groups on the surface of GO sheets [14–18]. These strong interactions allowed PAA to effectively adhere to the GO surface, as shown in Figure 2.4a. After the PAA/GO aerogels are formed by freeze drying, the PAAs appear to form a stringy, dendritic structure positioned within the pores and adhered on the surface of the GO (Figure 2.4a and 2.4b).

Interestingly, the concentration and M_v of PAA used in the PAA/GO precursor both strongly affected the morphology of the PAA/GO aerogels. As illustrated in Figure A.4, as the 450 kDa PAA concentration was increased (Figure A.4a to A.4c), the stringy, dendritic PAA formed more densely within the aerogel skeleton as expected, while maintaining a fairly regular pore structure. However, as the M_v increased to 1,250 kDa, the PAA was not dispersing as evenly throughout the aerogels as evidenced by a less regular porous structure (representative SEM images in Figure A.4d to A.4f) with higher overall aerogel mass density (Table 2.1). This is possibly due to the lesser overall mobility of the high M_v polymer. Stringy, dendritic PAA was not observed in the pores at the highest PAA concentrations (Figure A.4e to A.4f). Even so, all the aerogels in Figure A.4d to A.4f still displayed significantly enhanced mechanical integrity compared to aerogels without PAA added, similarly to the 450 kDa samples; however, the elasticity deteriorated either due to the less regular pore structure or highly entangled polymer. These mechanical property details will be discussed in a later section.

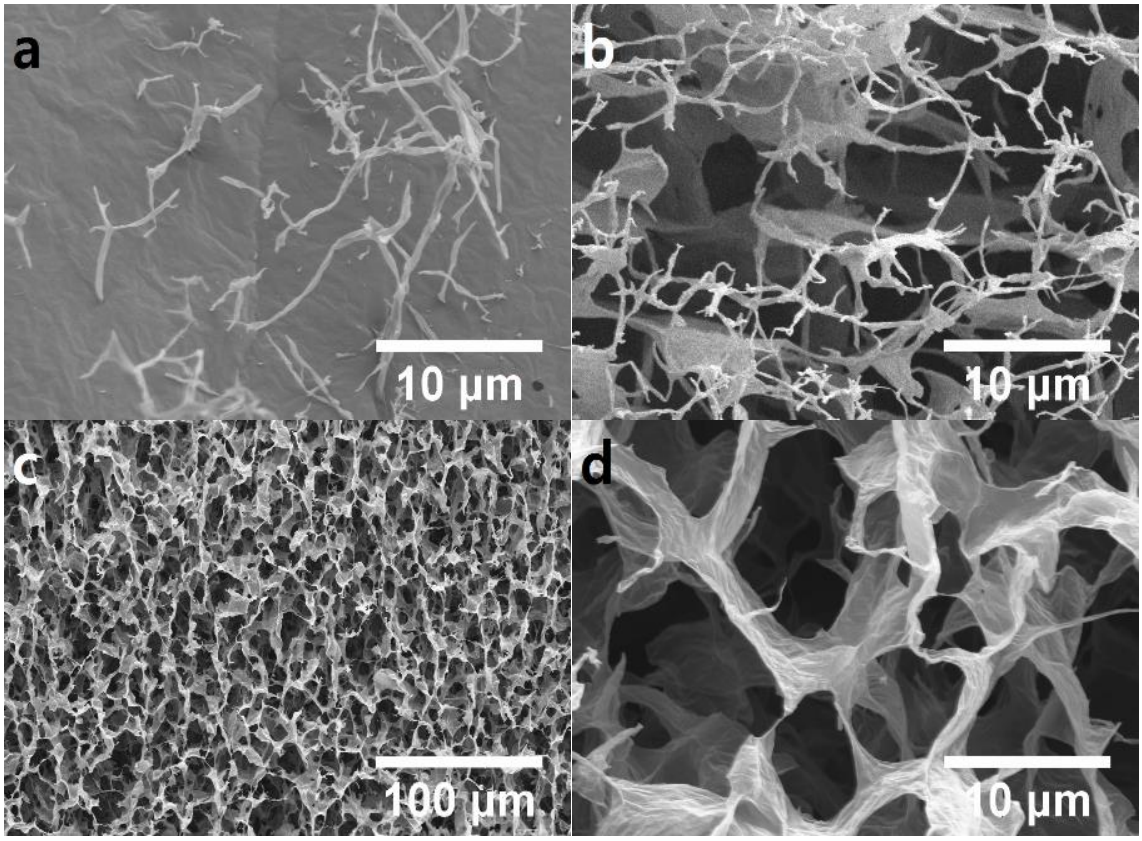

Figure 2.4. Selected SEM images of PAA/GO 450 kDa/50 aerogels showing (a) adherence of PAA on GO surfaces, (b) PAA dendritic strings inside the pores before thermal annealing and the corresponding XPAA/rGO aerogel after thermal annealing at (c) low and (d) high magnification. Adapted with permission from reference [8]. Copyright 2015 American Chemical Society.

After reducing GO and crosslinking PAA, the XPAA can adhere to rGO by hydrogen bonding interactions or covalent bonds, both of which contribute to the enhancement in the overall stiffness and mechanical integrity by interconnecting nearby GO sheets creating an elastic web-like structure as the pore walls. Interestingly, the stringy, dendritic structure of PAA evolves during thermal annealing/crosslinking to a morphology where XPAA appears mostly adhered to rGO sheets with a few XPAA bridges between sheets (Figure 2.4c and 2.4d). As expected, the overall properties of the final XPAA/rGO aerogels can depend strongly on the concentration and M_v of the PAA

added during preparation, similar to PAA/GO aerogels. The morphologies were investigated for all of the samples (Figure A.5). Identical to the PAA/GO aerogels, intermixing high concentrations of high M_v PAA tended to produce XPAA/rGOs with less regular pores and largely XPAA coated rGO sheets; therefore, the optimum concentration and M_v of PAA was found to be 450 kDa/50, 450 kDa/75 and 1,250 kDa/25. Putting all this chemical and structural information together, a proposed schematic illustration of the morphology of the aerogels at different stages is presented in Figure 2.5.

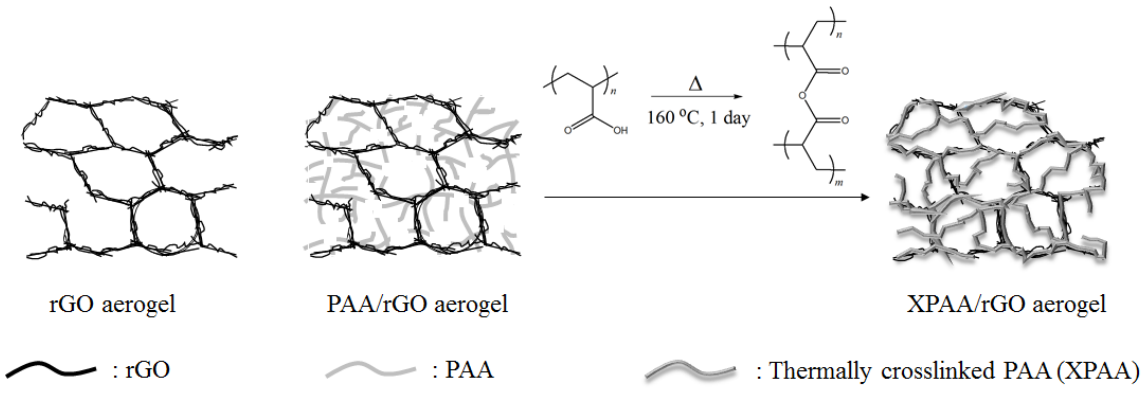

Figure 2.5. Scheme of proposed morphology of the XPAA/rGO aerogels compared to a neat rGO aerogel. Adapted with permission from reference [8]. Copyright 2015 American Chemical Society.

These morphological findings strongly correlated with the mechanical performance in compression and release cycles. As summarized in Figure 2.6, intermixing a small amount of PAA and thermally crosslinking the structure resulted in an increase as large as 2,400% in the maximum normal stress (related to compression modulus) during the 1st cycle (Figure 2.6a), whereas a maximum of 500% increase in the maximum normal stress could be achieved during the 10th cycle (summary in Figure 2.6b; all 10 cycles of all samples shown in Figure A.6). The maximum normal stress

values continuously decreased and reached an asymptotic point with increasing number of compression/release cycles (Figure 2.6b). The hysteresis between the first cycle and subsequent cycles can be attributed to permanent polymer and rGO structural deformation/reorganization, mainly caused during the first compression. This conclusion is supported by observing different cross-sectional SEM images of the compressed aerogel samples that show some fractured structural elements that appear as dangling threads (selected samples shown in Figure A.7). The incorporation of a small amount of PAA for both the 450 kDa/25 and 1,250 kDa/25 cases showed little or no enhancement in the maximum normal stress. However, as the concentration increased, the improvement became more pronounced (Figure 2.6c). Although the maximum normal stresses for all of the samples was reduced after 10 repeated cycles, most of the XPAA/rGO aerogels still exhibited much higher normal stresses compared with that of the pure rGO aerogel.

Samples such as 450 kDa/50 and 450 kDa/75 featured full recovery to the original volume after each and every compression/release cycle (Figure 2.7a); however, for the case of the 1,250 kDa/50 and 1,250 kDa/75 samples, some permanent deformation was observed with each subsequent cycle, resulting in a large permanent deformation at the end of the experiment (Figure 2.7b). Again, this permanent deformation was strongly related to the morphological structure of these aerogels (Figure A.5), where a large amount of high M_v PAA appeared to wet the GO surface instead of forming elastic bridging PAA elements as shown in Figure 2.4.

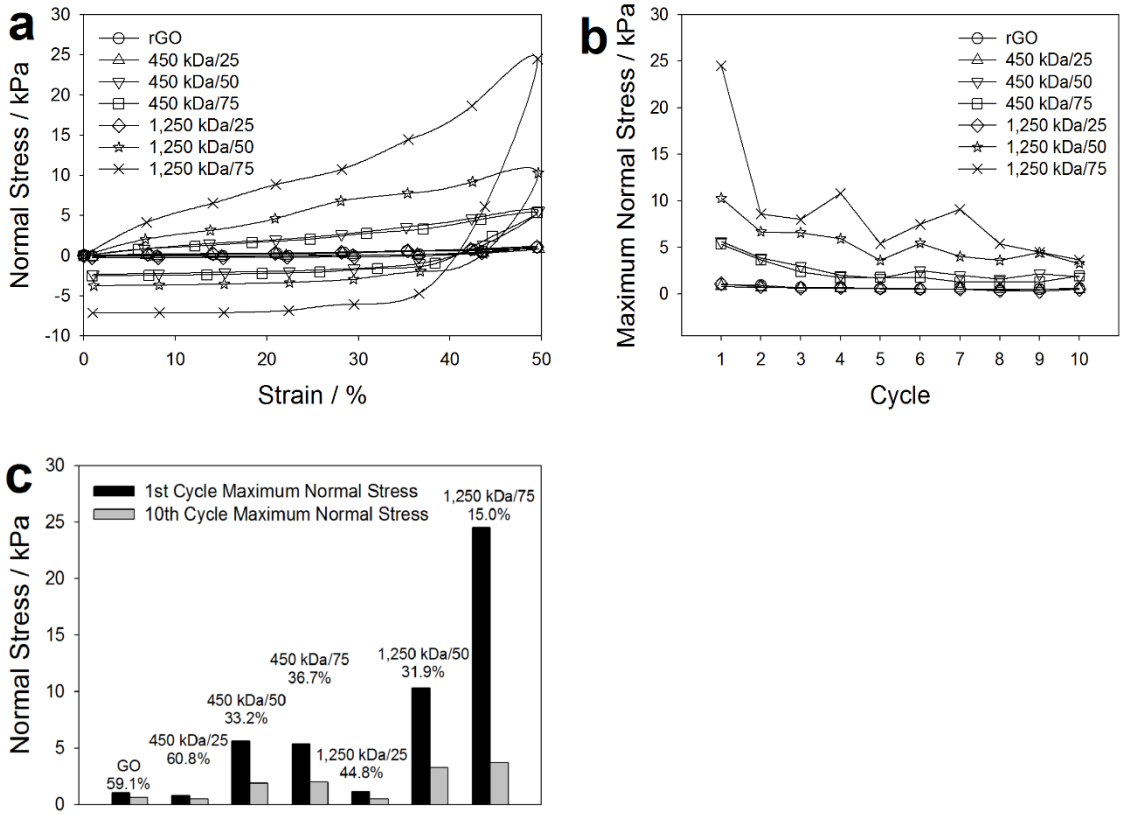

Figure 2.6. (a) Overlay of the 1st compression/release cycle test for strains up to 50% from XPAA/rGO aerogels with various concentrations and molecular weights of PAA. (b) The corresponding maximum normal stress values for consecutive cycles. (c) The percentage of maximum stress values remaining after 10 cycles compared to that of the 1st cycle. Adapted with permission from reference [8]. Copyright 2015 American Chemical Society.

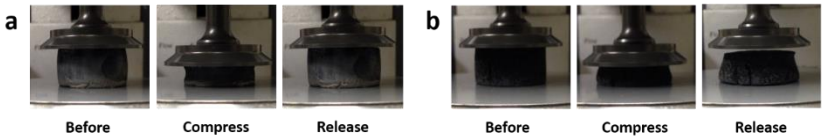

Figure 2.7. Digital images showing the compressibility of (a) 450 kDa/50 and (b) 1,250 kDa/75 XPAA/rGO aerogels during the 10th compression/release cycle. Adapted with permission from reference [8]. Copyright 2015 American Chemical Society.

2.4.4. Applications

Despite the ultralight aspect and high surface area of rGO aerogels (without PAA) that has driven interest in various potential applications, they are typically extremely delicate and fragile, requiring careful handling to prevent them from breaking or collapsing. Practical application of these materials requires robustness during handling and deployment; therefore, the qualitative mechanical integrity of the pure rGO aerogels and the XPAA/rGO aerogels was compared. Attempts to hold rGO aerogels or cut them with a razor blade or a pair of scissors were nearly impossible without significantly disrupting the original form or fracturing them completely (demonstration shown in Figure A.8). However, by applying the method for forming XPAA/rGO aerogels described in this research, it was possible to firmly hold and cut aerogels cleanly without disrupting the original state of the sample (Figure A.9a and A.9b) due to the strong interactions between the rGOs and PAAs and the unique elastic crosslinked polymer structure that reinforces the aerogel. Apart from the large improvement in the handle-ability and mechanical integrity of the sample, this material features excellent recovery when subjected to a weight more than 10,000 times its own weight. Figure 2.8 demonstrates ~50 mg of an aerogel sample supporting a 500 g weight leading to large structural deformation. This XPAA/rGO aerogel immediately recovered back to its original state when the weight was removed without reducing the initial height or volume of the aerogel. This supporting weight ratio is equivalent of a 65 kg man holding 9 space shuttles or 125 African elephants without causing any irreversible damage. This finding was truly remarkable considering the combination of the supporting weight ratio of the XPAA/rGO aerogels and its very low density, which is nearly ~200 times lighter than water. It is noteworthy that several other studies have shown use of GO and rGO aerogels as rigid, non-elastic supports for similar weight ratios. In our view, the mechanically

robust and elastic character of the XPPA/rGO aerogels, demonstrated here by their ability to support significant weight with full recovery of their original volume, highlights a new and highly attractive feature of the present materials.

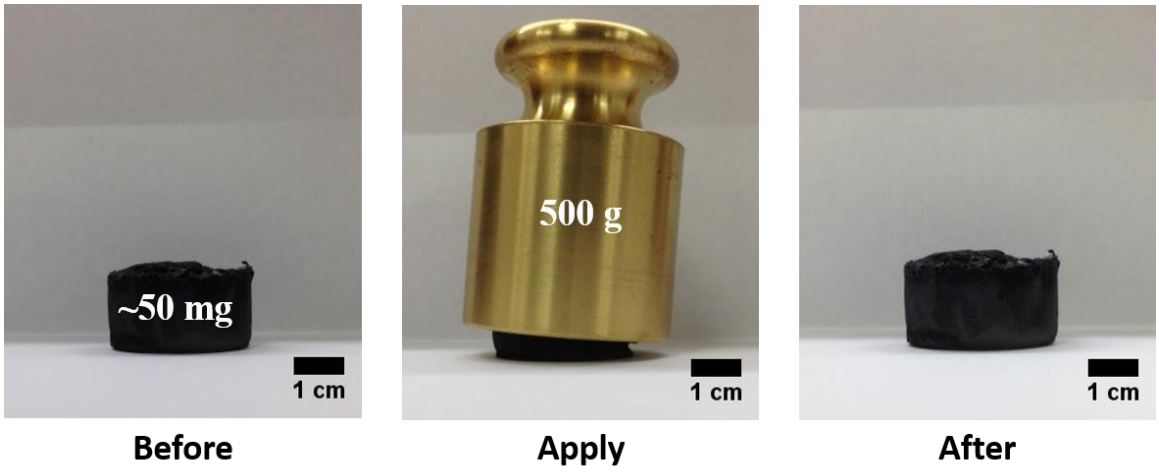

Figure 2.8. Images of aerogels before, during and after application of a 500 g weight. Adapted with permission from reference [8]. Copyright 2015 American Chemical Society.

To ensure that incorporating PAA did not disrupt other attractive properties of rGO aerogels, we demonstrated the performance of XPAA/rGO aerogels as a super-absorbent and pressure sensor (super-absorbent in Figure 2.9 and pressure sensor in Figure A.10). A series of different oils were prepared to confirm the super-oleophilicity of the XPAA/rGO aerogels (Figure 2.9a). The average absorption capacity for 6 different oils was approximately 120 g oil/g aerogel, which is the range of other aerogels [19–21]. The performance of the XPAA/rGO aerogels as a super-absorbent was also visualized using gasoline colored with a fluorescent dye, which clearly demonstrated its capability as a potential material for environmental remediation (Figure 2.9b).

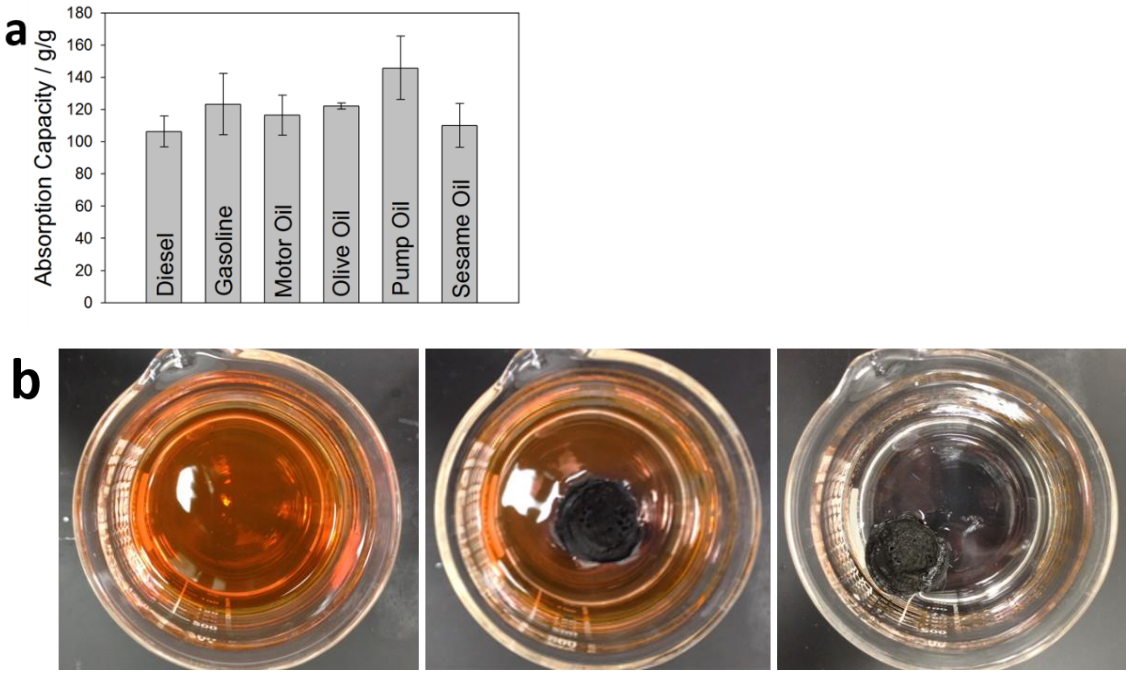

Figure 2.9. Oil absorption capacity comparison for different oils/solvents. (a) Absorption capacities for various oils expressed as g oil/g aerogel. (b) A visual demonstration of oil absorption using gasoline as the absorbed solvent from t=0 (leftmost image) to t=35s (rightmost image). Adapted with permission from reference [8]. Copyright 2015 American Chemical Society.

Finally, exploiting the fact that XPAA/rGO aerogels have excellent recovery after large deformation (Figure 2.8.), this material also performed well as a pressure sensor (Figure A.10). To quantitatively measure the resistance during compression, a simple experimental set-up was used as shown in Figure 2.10a. By compressing the material, the pressure applied to the XPAA/rGO aerogels affected the number of conductive pathways, which increased the conductivity of the material. The resistance of 450 kDa/50 without compression had an average value of 37.4 kΩ but reached an asymptotic point around ~2 kΩ when the sample was compressed over 70% (Figure 2.10b). This resistance range made it possible to modulate light emitted from a LED lamp with a 6 V battery using the XPAA/rGO as one element in the circuit pathway. The LED intensity increased with

applied pressure/compressive strain as more conductive pathways were introduced, and it was completely reversible for consecutive cycles (Figure 2.10c).

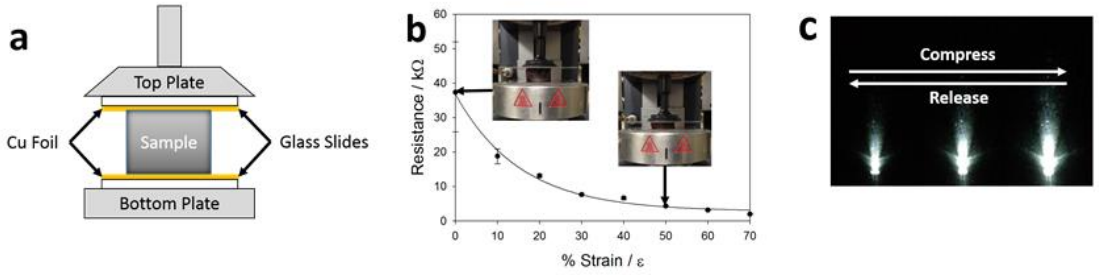

Figure 2.10. Pressure sensing capabilities of 450 kDa/50 XPAA/rGO through modulation of resistivity. (a) Schematic view of the experiment conducted to measure the resistivity of the material during compression between parallel plates in a rheometer. (b) Changes in resistance depending on the % compressive strain applied. Inset images show different states in the experiments. (c) Light intensities obtained from an LED lamp in a dark room during compression and release. The light intensity varies reversibly depending on the pressure applied to the XPAA/rGO aerogels. Adapted with permission from reference [8]. Copyright 2015 American Chemical Society.

2.5. CONCLUSIONS

By taking advantage of this new process to incorporate XPAA into rGO aerogels, the delicate and fragile nature of rGO aerogels could be greatly improved. The process proposed in this work is not only simple and straightforward, but also cost-effective and does not include complicated or multistep chemical reactions. XPAA/rGO aerogels are ultralight, highly compressible and mechanically robust, due to strong interactions (both covalent and h-bonding) between rGO with PAA and the unique XPPA network morphology that reinforces the mostly rGO pore walls. Even after being subjected to a weight 10,000 times heavier than the sample, the aerogel was capable of fully recovering its original volume. In addition, the XPAA/rGO aerogels retained higher maximum

normal stresses during consecutive compression and release cycles than pure rGO aerogels indicating an increased and sustained compressive modulus. The material could easily be handled and cut or trimmed without affecting other attractive properties of the aerogel. Furthermore, the performance as a super-absorbent and pressure sensor was not adversely affected by incorporation of XPAA. This approach could enable more versatile usage of graphitic aerogels in many commercial applications, such as environmental remediation, super-hydrophobic and super-oleophilic materials, energy storage, etc.

2.6. REFERENCES

[1] Chabot V, Higgins D, Yu A, Xiao X, Chen Z, Zhang J. A review of graphene and graphene oxide sponge: material synthesis and applications to energy and the environment. Energy Environ Sci 2014;7:1564. doi:10.1039/c3ee43385d.

[2] Nardecchia S, Carriazo D, Ferrer ML, Gutiérrez MC, del Monte F. Three dimensional macroporous architectures and aerogels built of carbon nanotubes and/or graphene: synthesis and applications. Chem Soc Rev 2013;42:794–830. doi:10.1039/c2cs35353a.

[3] Sun H, Xu Z, Gao C. Multifunctional, Ultra-Flyweight, Synergistically Assembled Carbon Aerogels. Adv Mater 2013;25:2554–60. doi:10.1002/adma.201204576.

[4] Hu H, Zhao Z, Wan W, Gogotsi Y, Qiu J. Ultralight and highly compressible graphene aerogels. Adv Mater 2013;25:2219–23. doi:10.1002/adma.201204530.

[5] Hong J-Y, Bak BM, Wie JJ, Kong J, Park HS. Reversibly Compressible, Highly Elastic, and Durable Graphene Aerogels for Energy Storage Devices under Limiting Conditions. Adv Funct Mater 2014:n/a – n/a. doi:10.1002/adfm.201403273.

[6] Hummers WS, Offeman RE. Preparation of Graphitic Oxide. J Am Chem Soc 1958;80:1339–1339. doi:10.1021/ja01539a017.

[7] Bi H, Xie X, Yin K, Zhou Y, Wan S, He L, et al. Spongy graphene as a highly efficient and recyclable sorbent for oils and organic solvents. Adv Funct Mater 2012;22:4421–5. doi:10.1002/adfm.201200888.

[8] Ha H, Shanmuganathan K, Ellison CJ. Mechanically Stable Thermally Crosslinked Poly(acrylic acid)/Reduced Graphene Oxide Aerogels. ACS Appl Mater Interfaces 2015;7:6220–9. doi:10.1021/acsami.5b00407.

[9] Blanco-Fuente H, Anguiano-Igea S, Otero-Espinar FJ, Blanco-Méndez J. Kinetics of anhydride formation in xerogels of poly(acrylic acid). Biomaterials 1996;17:1667–75. doi:10.1016/0142-9612(96)87646-0.

[10] La Y-H, Edwards EW, Park S-M, Nealey PF. Directed Assembly of Cylinder-Forming Block Copolymer Films and Thermochemically Induced Cylinder to Sphere Transition: A Hierarchical Route to Linear Arrays of Nanodots. Nano Lett 2005;5:1379–84. doi:10.1021/nl0506913.
[11] Dong J, Ozaki Y, Nakashima K. Infrared, Raman, and Near-Infrared Spectroscopic Evidence for the Coexistence of Various Hydrogen-Bond Forms in Poly(acrylic acid). Macromolecules 1997;30:1111–7. doi:10.1021/ma960693x.
[12] Qiu L, Liu D, Wang Y, Cheng C, Zhou K, Ding J, et al. Mechanically Robust, Electrically Conductive and Stimuli-Responsive Binary Network Hydrogels Enabled by Superelastic Graphene Aerogels. Adv Mater 2014;26:3333–7. doi:10.1002/adma.201305359.
[13] Qiu L, Liu JZ, Chang SLY, Wu Y, Li D. Biomimetic superelastic graphene-based cellular monoliths. Nat Commun 2012;3:1241. doi:10.1038/ncomms2251.
[14] Sun S, Wu P. A one-step strategy for thermal- and pH-responsive graphene oxide interpenetrating polymer hydrogel networks. J Mater Chem 2011;21:4095. doi:10.1039/c1jm10276a.
[15] Shen J, Yan B, Li T, Long Y, Li N, Ye M. Mechanical, thermal and swelling properties of poly(acrylic acid)–graphene oxide composite hydrogels. Soft Matter 2012;8:1831. doi:10.1039/c1sm06970e.
[16] Huang Y, Zeng M, Ren J, Wang J, Fan L, Xu Q. Preparation and swelling properties of graphene oxide/poly(acrylic acid-co-acrylamide) super-absorbent hydrogel nanocomposites. Colloids Surfaces A Physicochem Eng Asp 2012;401:97–106. doi:10.1016/j.colsurfa.2012.03.031.
[17] Lee S, Lee H, Sim JH, Sohn D. Graphene oxide/poly(acrylic acid) hydrogel by ??-ray pre-irradiation on graphene oxide surface. Macromol Res 2014;22:165–72. doi:10.1007/s13233-014-2025-x.
[18] Faghihi S, Gheysour M, Karimi A, Salarian R. Fabrication and mechanical characterization of graphene oxide-reinforced poly (acrylic acid)/gelatin composite hydrogels. J Appl Phys 2014;115. doi:10.1063/1.4864153.
[19] Li R, Chen C, Li J, Xu L, Xiao G, Yan D. A facile approach to superhydrophobic and superoleophilic graphene/polymer aerogels. J Mater Chem A 2014;2:3057. doi:10.1039/c3ta14262k.
[20] Bi H, Xie X, Yin K, Zhou Y, Wan S, Ruoff RS, et al. Highly enhanced performance of spongy graphene as an oil sorbent. J Mater Chem A 2014;2:1652–6. doi:10.1039/C3TA14112H.
[21] Wang Y, Yadav S, Heinlein T, Konjik V, Breitzke H, Buntkowsky G, et al. Ultra-light nanocomposite aerogels of bacterial cellulose and reduced graphene oxide for specific absorption and separation of organic liquids. RSC Adv 2014;4:21553. doi:10.1039/c4ra02168a.

Chapter 3: Thermal Stimuli-responsive Behavior of Pyrene End-functionalized PDMS Through Tunable π-π Interactions[2]

3.1. OVERVIEW

Another way to synthesize functional polymer/GO composites is to exploit π-π interactions between pyrene containing polymer and the GO basal plane. For this study, pyrene end-functionalized, telechelic poly(dimethyl siloxane) (PDMS) materials were synthesized and their response to different thermal stimuli was evaluated. The incorporation of pyrene end-groups introduces π-π interactions that facilitate a broad range of thermally responsive properties, in some circumstances forming pyrene nanocrystals that serve as physical crosslinks leading to elastic materials. By employing different PDMS main-chain lengths, samples exhibiting a 7 orders of magnitude change in storage modulus (G') in response to thermal stimuli were produced by modifying only the end-groups (0.6 wt % of all polymer segments). Repeated thermal cycling during rheological experiments revealed that π-π interactions and crystallization/melting kinetics of pyrene chain-ends plays a key role in their thermal responsiveness. The properties of these materials were tuned by adding free pyrene, neat PDMS or GO nanoparticles, making them attractive for many applications. For example, nanocomposites containing 1 wt% GO caused the melting temperature for pyrene crystal domains to more than double, and even induced pyrene end-group crystallization in samples that did not exhibit crystals in neat form. It is hypothesized that these features originate from π-π interactions between pyrene ends and GO surfaces.

---

[2] Ha H (Designed and performed experiments, wrote and edited the paper), Shanmuganathan K, Fei Y, Ellison CJ. Thermal stimuli-responsive behavior of pyrene end-functionalized PDMS through tunable Π-Π interactions. J Polym Sci Part B Polym Phys 2016;54:159–68. doi:10.1002/polb.23805.

3.2. INTRODUCTION

Stimuli-responsive polymers, also known as “smart polymers”, are materials that undergo large changes in their properties (e.g. color, transparency, conductivity, permeability, shape, etc.) in response to one or more stimuli, such as temperature, pH, heat, light, force, etc [1–3]. Due to their inherently rapid response to a variety of stimuli, stimuli-responsive polymers could be useful in many applications including sensors, actuators, drug delivery systems, and self-healing materials [4–7]. Stimuli-responsive characteristics are usually driven by modulating chemical and physical interactions that enable the material to change dynamically in a rapid and often reversible way. Examples of the interactions that give rise to such extraordinary behavior include dynamic covalent bonds (chemical bonds) and non-covalent bonds (physical bonds), such as hydrogen bonds [8,9], ionic interactions [10–12], and π-π bond interactions [13–17].

Among the many possible ways to introduce stimuli-responsive properties, a rapidly growing area of interest is exploitation of π-π bond interactions, which refers to noncovalent bonding associated with nearby π electron containing functional groups such as aromatics. The term “π-π stacking”, or “π-π interactions” has been designated as misleading in some cases, because the term suggests a preferred face-to-face geometry, which is not observed in many situations [18,19]. In this work, the term “π-π interactions” is used only for those interactions between multiple planar aromatic units (e.g., pyrene with four fused planar aromatic units in this report), where extensive theoretical evidence [18–20] suggests preferential interactions in a largely face-to-face manner.

Pyrenes have recently garnered attention [20–24] as a molecule that readily participates in π-π interactions. Pyrenes strongly absorb light at wavelengths < 350 nm and can convert that light to heat, which can lead to the dissociation of the π-π

interactions; intuitively, heat alone can also induce dissociation of the π-π interactions. Due to the abundance of π bonds, this molecule can interact with other nanoparticles/molecules containing aromatic rings, such as CNTs, GOs, or graphenes, suggesting a useful design concept in nanocomposite materials. Recently, Parviz et al. demonstrated the strong π-π interactions between functionalized pyrene derivatives and graphenes led to enhanced stability of graphenes in aqueous dispersions [13]. Notably, pyrene derivatives improved dispersion stability more than surfactants or other polymers due to the reduction in surface energy of the dispersion via π-π interactions. In a later study, Parviz and coworkers also introduced a synthetic polysiloxane/graphene composite with pyrenes as the pendant side-groups of the polysiloxane. The addition of pyrenes to the polymer backbone enhanced the dispersion of graphenes in the composite and as a result, increased the electrical conductivity [14].

Pyrenes have also been explored as functional end groups in polymers. Several fundamental studies based on pyrene end-functionalized telechelic PDMS materials have been performed by Torkelson and coworkers. Kim and Torkelson first reported their solution state properties at room temperature and their tunability by thin film confinement using florescence spectroscopy [15]. They found the material properties strongly depended on the film thickness and confirmed that the energy of pyrene-pyrene dimer formation was approximately an order of magnitude higher than thermal energy. Later, Jones and Torkelson performed more detailed research on the crystallization of the pyrene nanocrystals and the thermal properties of the telechelic polymer [16,17]. They concluded that nanocrystals formed by pyrenyl units were 2-3 nm in size and contained approximately 18-30 pyrenyl end units. Furthermore, depending on the molecular weight (MW) of the polymer, physical crosslinking significantly affected the crystallization and mobility of the polymer chains. However, despite the promising properties of pyrene end-

functionalized polymers, to the best of our knowledge no fundamental studies on their rheological properties and thermoreversible behavior have been reported to date.

A major goal of this work was to synthesize pyrene end-functionalized telechelic polymers that respond rheologically to a thermal stimulus by modulating π-π interactions of the end-groups. For typical polymer molecular weights (i.e., 1-100 kg/mol), the pyrene chain ends are expected to represent less than 1 wt% of the host polymer repeat units. While the nanoconfined crystallization properties of similar materials have been studied previously, detailed understanding of the responsiveness of their flow properties to heating/cooling cycles and how their responsiveness is connected to their molecular architecture and structural organization is still lacking. Furthermore, approaches for tuning the thermal responsiveness will be demonstrated herein in order to expand the range of temperatures where a change in rheological response is triggered. Such materials could find application as tunable damping materials, heat or light sensors, conductive gels or light repositionable adhesives.

3.3. EXPERIMENTAL SECTION

3.3.1. Materials

Two aminopropyl terminated PDMS samples with viscosities of 100 and 1,000 cSt were purchased from Gelest, Inc., and used without any further purification. The compounds γ-oxo-1-pyrenebutyric acid (OPBA, Astatech, Inc.), N-hydroxysuccinimide (NHS, Acros), and N,N'-dicyclohexylcarbodiimide (DCC, Sigma-Aldrich) were used to synthesize γ-oxo-1-pyrenebutyric acid N-hydroxysuccinimide ester (OPBA NHS ester). HPLC grade tetrahydrofuran (THF), ethanol, and methanol were purchased from Fisher Scientific and used as-received during the synthesis procedure. Graphene oxide (GO) was

synthesized as described in Chapter 2 [25]. Table 3.1 summarizes the properties of the aminopropyl terminated PDMS provided by the manufacturer and the corresponding measurements made in this study. For clarity, the various synthesized polymers will be denoted by the presence of a pyrene end group (N for aminopropyl terminated polymer and P for polymer containing pyrene end groups) followed by the viscosity (100 or 1,000 cSt) of the precursor PDMS. For example, P100 represents pyrene end-functionalized PDMS synthesized using N100 precursor.

Table 3.1. Comparison of PDMS precursor properties. Adapted with permission from reference [26]. Copyright 2016 Wiley.

Sample Designation	Viscosity (cSt) Provided	Viscosity (cSt) Measured[a]	MW (g/mol) Provided	MW (g/mol) Measured[b]	% Amine	
					wt %	mol %
N100	100	100	5,000	5,000	0.6-0.7	2.9
N1000	1,000	880	25,000	23,600	0.11-0.12	0.6

[a] Measured as zero shear viscosity by a constant shear rate experiment. [b] Calculated by end group analysis from ^{1}H-NMR spectra (assuming all PDMS chains have 2 amino end groups).

3.3.2. Synthesis and Sample Preparation Procedures for Pyrene End-functionalized PDMS

Pyrene end-functionalized PDMS (P series) was synthesized as described in detail elsewhere [15]. A detailed scheme of the required chemical synthesis procedure is presented in Figure 3.1. Briefly, OPBA and NHS (1:1 mole ratio) were dissolved in a flask filled with THF and placed in an ice bath. In a separate beaker, 1.1 equivalents of DCC with respect to OPBA was dissolved in THF and transferred into a burette. The

DCC solution was then mixed drop-wise with the OPBA:NHS solution under agitation and reacted for an additional 24 hours at room temperature. After the reaction was completed, the solution was filtered, and the liquid filtrate was rotary evaporated to crystallize the OPBA NHS ester. These crystals were washed with ethanol by centrifuging several times before drying in a vacuum oven overnight. ^{1}H-NMR was used to determine the purity of the OPBA NHS ester (^{1}H-NMR spectrum presented in Figure B.1). The mass yield was ~70 wt%, while the conversion was nearly 100%, judging by the disappearance of the –COOH peak at 12.3 ppm.

After successfully synthesizing OPBA NHS ester, N series PDMS was reacted in THF with a 2-fold molar excess of OPBA NHS ester at 60 °C for 24 hours. The solution was rotary evaporated completely and extracted 10 times using excess cold methanol. After confirmation that free, unreacted OPBA NHS ester was removed, the material was dried in a vacuum oven at 60 °C for 12 hours to eliminate any residual solvent (^{1}H-NMR spectrum presented in Figure B.2). During multiple extractions, small molecular weight (MW) polymers were partially removed along with the solvent, which resulted in a slight increase in MW for all of the P series. By end-group analysis of the ^{1}H-NMR spectra, P100 MW was increased from 5,000 g/mol (N100) to 8,000 g/mol, whereas P1000 MW increased from 23,600 g/mol (N1000) to 25,600 g/mol.

Pure PDMS, OPBA NHS ester, or GO were mixed with P series PDMS in THF at room temperature and sonicated using a 400 W probe sonicator (Branson, Digital Sonifier 450) with 10% amplitude for 10 minutes (24 kJ) in an ice bath in order to study the tunability of the material properties. The solutions were cast on a PTFE dish and air dried for 3 days then dried in a vacuum oven at room temperature for 1 day. Additionally, the P100/1 wt% GO composite material was molded in a silicone elastomer mold by

heating it to 120 °C and slowly cooling back to room temperature so that the sample could be easily detached from the mold.

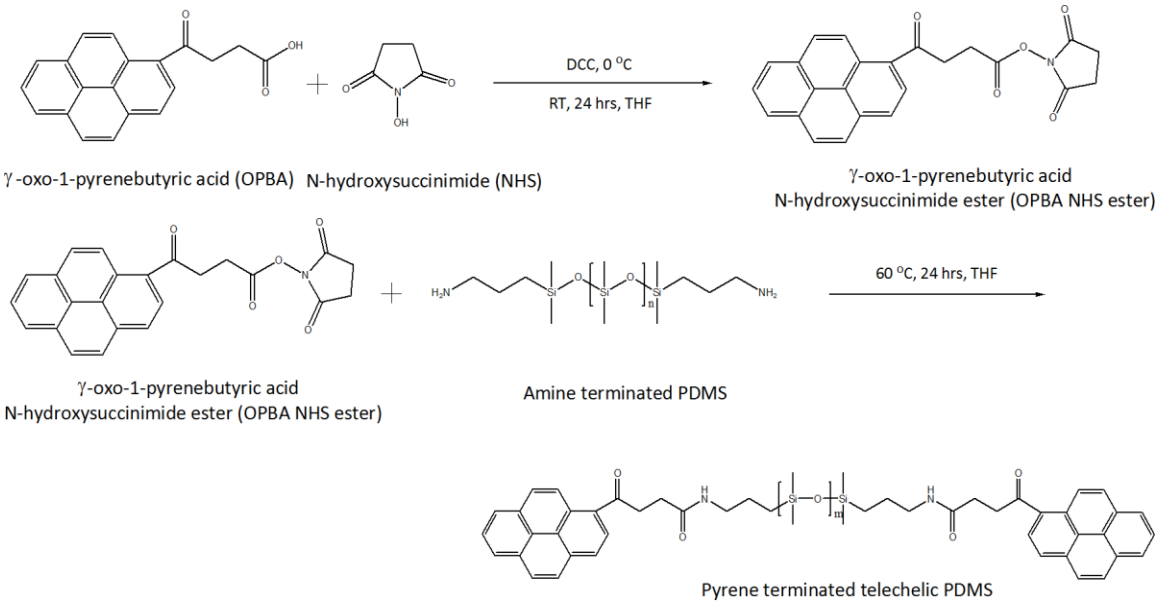

Figure 3.1. Reaction scheme for synthesizing OPBA NHS Ester (top) and telechelic pyrene end-functionalized PDMS denoted P Series (bottom). Adapted with permission from reference [26]. Copyright 2016 Wiley.

3.3.3. Characterization of Pyrene End-functionalized PDMS

^{1}H-NMR spectra for the N and P series PDMS were obtained by Varian Direct Drive 400 MHz instrument using deuterated chloroform solvent without any TMS. For the N series PDMS samples (NH_2-PDMS-NH_2), the -CH_2NH_2 peak and the -$SiCH_3$ peak were observed at 2.6 ppm and 0.0 ppm, respectively. For P series PDMS samples, characteristic peaks are -CH_2CONH at 2.7 ppm and 3.6 ppm, -CONH- at 5.7 ppm, and pyrene ends at 7.8-9.0 ppm. GPC (Viscotek, GPCmax VE 2001) equipped with a fluorescence detector with THF eluent was used to detect the presence of pyrene-

containing small molecules with an excitation wavelength of 340 nm and an emission wavelength of 394 nm. Due to the similar refractive index values between THF and PDMS, the MW was calculated based on ^{1}H-NMR end-group analysis instead of refractive index detection chromatography. Thermal properties of the product were measured using differential scanning calorimetry (DSC; Mettler Toledo DSC1). Heating and cooling rates of 20 °C/min were used for all experiments. The crystallization or melting temperature (T_c or T_m) was defined as the maximum or minimum peak points from the second cooling or second heating curves. All of the rheological experiments were conducted on a shear rheometer (TA Instruments, AR-2000EX) using a 20 mm parallel upper plate with a gap of 500 μm and a Peltier lower plate fixture for temperature control. First, strain sweep and time sweep experiments were conducted to identify the linear viscoelastic regime and to ensure the stability of the measured values over time. Crystallization kinetics were studied rheologically by heating the sample at 80 °C followed by quenching the sample to a desired temperature and performing an isothermal time sweep experiment for 10 minutes as the pyrene ends formed crystals. Temperature cycle experiments were conducted using a 5 °C/min ramp rate with 10 rad/s as the frequency.

3.4. Results and Discussion

3.4.1. Optical Appearance and Basic Flow Properties

As shown in Figure 3.2, after developing adequate washing and degassing procedures, transparent but light brown colored pyrene end-functionalized PDMS materials were obtained.

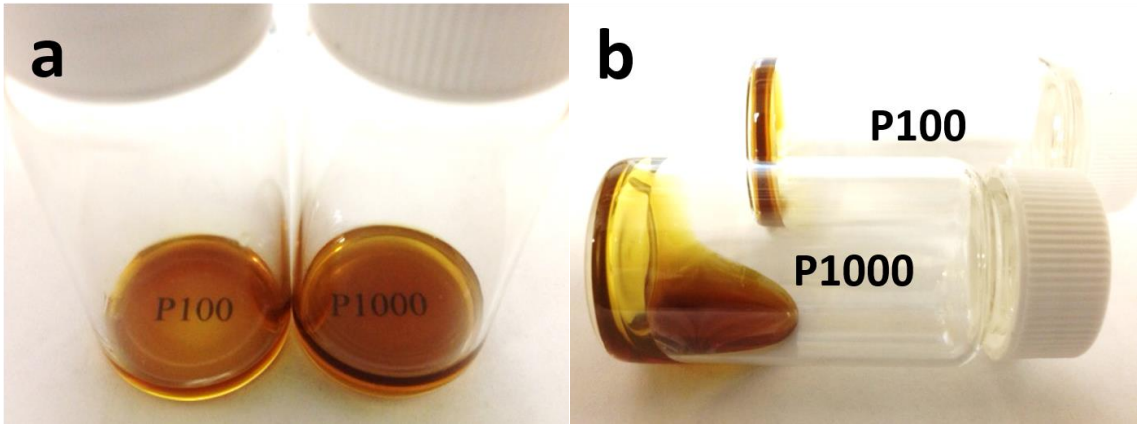

Figure 3.2. Optical images of pyrene-functionalized PDMS with two different molecular weights. a) P100 (left) and P1000 (right) both show optical transparency at room temperature, while b) P100 (top) forms a solid gel at room temperature and P1000 (bottom) flows like a viscous liquid. Adapted with permission from reference [26]. Copyright 2016 Wiley.

While MW had little impact on appearance in terms of transparency and color (Figure 3.2a), the precursor MW had a significant effect on the flow properties of the pyrene functionalized PDMS (Figure 3.2b). Interestingly, the polymer prepared with a lower MW precursor formed solid gels while that prepared with a higher MW precursor flowed as a viscous liquid. This phenomenon is attributed to a higher density of pyrene ends in the lower MW (P100) sample that facilitates formation of pyrene nanocrystals that serve as physical crosslinks. The driving force for producing nanocrystals is the formation of complementary π-π interactions with a binding energy of 20-26 kJ/mol [15,20], which is far above thermal energy at room temperature (kT ~2.4 kJ/mol), and the low solubility of pyrene in PDMS (solubility parameter δ_{pyrene} = 25.2 $MPa^{1/2}$, δ_{PDMS} = 15.1 $MPa^{1/2}$) [27,28]. The formation of pyrene nanocrystals and associated physical crosslinks is shown schematically in Figure 3.3. This structuring can induce thermoreversible elastomeric properties, which are addressed in more detail in later sections. In contrast, the lower concentration of pyrene ends associated with higher MW

PDMS (P1000) produces a material that is a viscous liquid (with ~40 times higher viscosity than the N1000 precursor) due to fewer pyrene end group interactions.

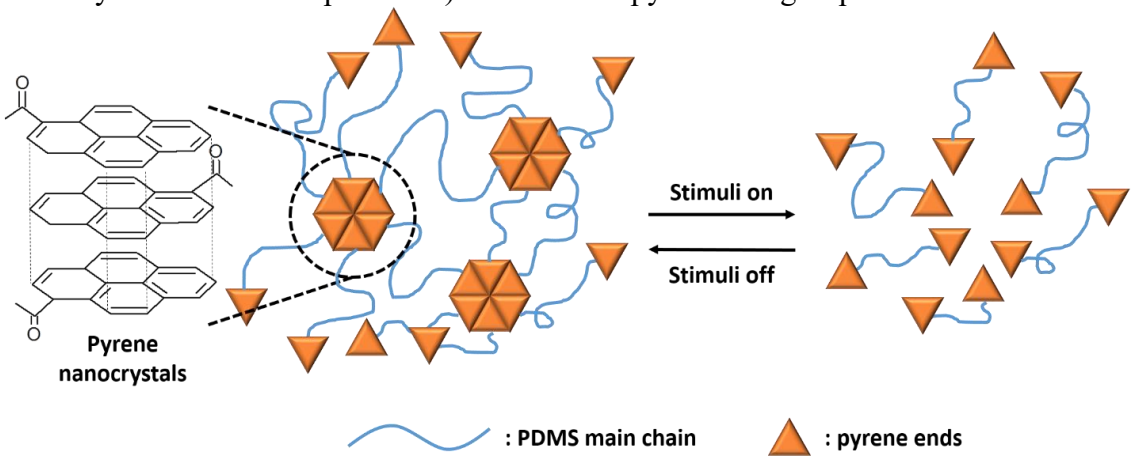

Figure 3.3. Schematic showing structuring and stimuli-responsive behavior of pyrene end-functionalized PDMS. Adapted with permission from reference [26]. Copyright 2016 Wiley.

Compared to N series PDMS samples which were optically transparent and uncolored as expected (Figure B.3), the presence of pyrene nanocrystals in P100 did not disrupt transparency, likely because the nanocrystal size is relatively small (2-3 nm) [17]. If the nanocrystal size were closer to the wavelength range of visible light, translucent or opaque optical properties would be expected. This suggests these materials could be used as UV light sensors or light repositionable adhesives, functions that would require high optical clarity.

3.4.2. Thermal Properties by DSC

The DSC thermograms in Figure 3.4 show that pyrene ends formed nanocrystals for P100, detected both as melting (upon heating; Figure 3.4a) and crystallization (upon cooling; Figure 3.4b) peaks. Prior work reported a single pyrene nanocrystal melting temperature at ~40 °C for low MW (5 and 7 kg/mol) pyrene end-functionalized PDMS,

whereas higher MW (ca. 25 kg/mol) PDMS required extensive annealing at low temperature in order to observe any pyrene nanocrystal melting behavior (T_m ~5-30 °C) [17]. However, in the present work (shown in Figure 3.4 DSC thermograms and associated Table 3.2 data), a bimodal pyrene melting peak was observed at 25.6 and 42.2 °C for the low MW pyrene functionalized PDMS material (P100). Similar to previous reports, no melting peak was observed for high MW P1000.

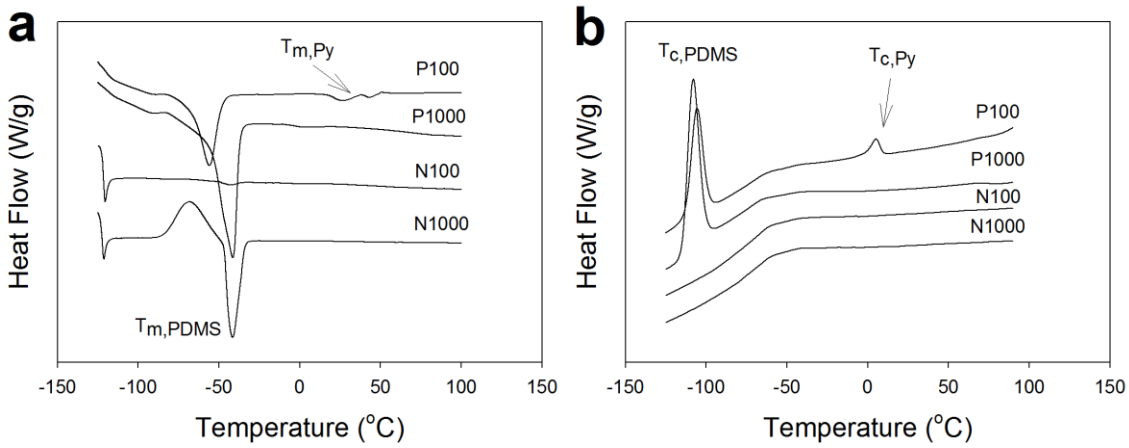

Figure 3.4. DSC thermograms for pyrene end-functionalized PDMS. a) 2nd heating curve and b) 2nd cooling curve with a 20 °C min^{-1} temperature ramp rate. Py indicates pyrene nanocrystal thermal properties while PDMS indicates thermal properties associated with the polymer main chain. Both melting temperatures (T_m) and crystallization temperatures (T_c) are identified. Adapted with permission from reference [26]. Copyright 2016 Wiley.

Table 3.2. Thermal properties of P100 and P1000 measured by DSC. T_c represents the crystallization temperature and T_m represents the melting temperature. Thermal properties derived from the polymer main chain are denoted as PDMS, whereas Py indicates the contribution due to the pyrene end. Adapted with permission from reference [26]. Copyright 2016 Wiley.

Sample	$T_{c,Py}$ (°C)	$T_{c,PDMS}$ (°C)	$T_{m,PDMS}$ (°C)	$T_{m,Py}$ (°C)
P100	4.9 ± 0.5	-105.8 ± 0.2	-56.6 ± 0.7	25.6 ± 1.5 42.2 ± 0.7
P1000	Not detected	-107.9 ± 0.1	-41.9 ± 0.4	Not detected

Interestingly, the melting temperature of the PDMS main chain ($T_{m,PDMS}$ in Figure 3.4a) in the P100 sample decreased to a lower temperature compared to the P1000 or N series samples. As the pyrene ends formed nanocrystals in P100, the polymer chain ends can be confined in physical crosslinks, and the overall mobility of the main chain can be reduced under these circumstances. Reduction in overall chain mobility is expected to result in smaller PDMS crystals and lower overall crystal content, which have correspondingly lower melting temperatures and reduced melting/crystallization peak areas [24]. In contrast, P1000 did not show any difference in $T_{m,PDMS}$ compared to N1000 precursor which once again clearly demonstrates the absence of the formation of pyrene nanocrystals in P1000.

However, all the P series exhibited a $T_{c,PDMS}$ during cooling (Figure 3.4b), indicative of the presence of favorable crystallization nucleation sites, allowing the P series main chain to nucleate faster than the N series. These nucleation sites are hypothesized to be provided by pyrene end groups in the P series, and in favor of this postulation, no cold crystallization was observed in any P series sample.

3.4.3. Rheological Properties During Heating and Cooling

Even though extensive information was obtained from DSC results, rheological studies provide additional understanding of the thermal properties. In fact, the inherently different behaviors of P100 and P1000 become more obvious when comparing the rheological properties of the materials, as illustrated in Figure 3.5. Modulus changes during heating (Figure 3.5a) and cooling cycles (Figure 3.5b) for the P series polymers are compared to the N series polymers (Figure 3.5c). As shown in Figure 3.5a, P100 had a broad and distinctive transition in the storage modulus G' over a wide temperature range from 20 °C to 60 °C during heating, whereas P1000 showed no significant

transition in the storage modulus. This result is in good agreement with DSC results and shows the significance of the π-π interactions of pyrene ends in controlling the properties of the material. Substituting amine end groups (consisting of less than 1 wt % of the whole polymer chain) with pyrene moieties drastically increased the storage modulus for P100 (more than 7 orders of magnitude compared to N100 near room temperature). Furthermore, the dramatic continuous reduction in P100 storage modulus with temperature clearly indicates that, although bimodal peaks were observed in the DSC results, the melting or disassociation of pyrene nanocrystals is continuous, and the actual gel point (i.e., where G' = G") of the transition was ~35 °C. These data are analogous with the image in Figure 3.2b where at room temperature P100 acts as a solid-gel indicated by a G' that is higher than G" (frequency sweep at 25 °C available in Figure B.4a).

P1000 exhibited a 2 orders of magnitude increase of in G' when compared to amine functionalized polymer (N1000), which is still a substantial increase given the low level of pyrene content. For P1000, the loss modulus (G") was higher than the storage modulus (G') at all measured temperatures, which is in good agreement with the liquid-like behavior observed in Figure 3.2b (frequency sweep at 25 °C available in Figure B.4b). In contrast, the N series rheological properties in Figure 3.5c did not exhibit any hysteresis or rheological transition behavior, which confirms that transforming the end group functionality is directly responsible for the large change in physical properties.

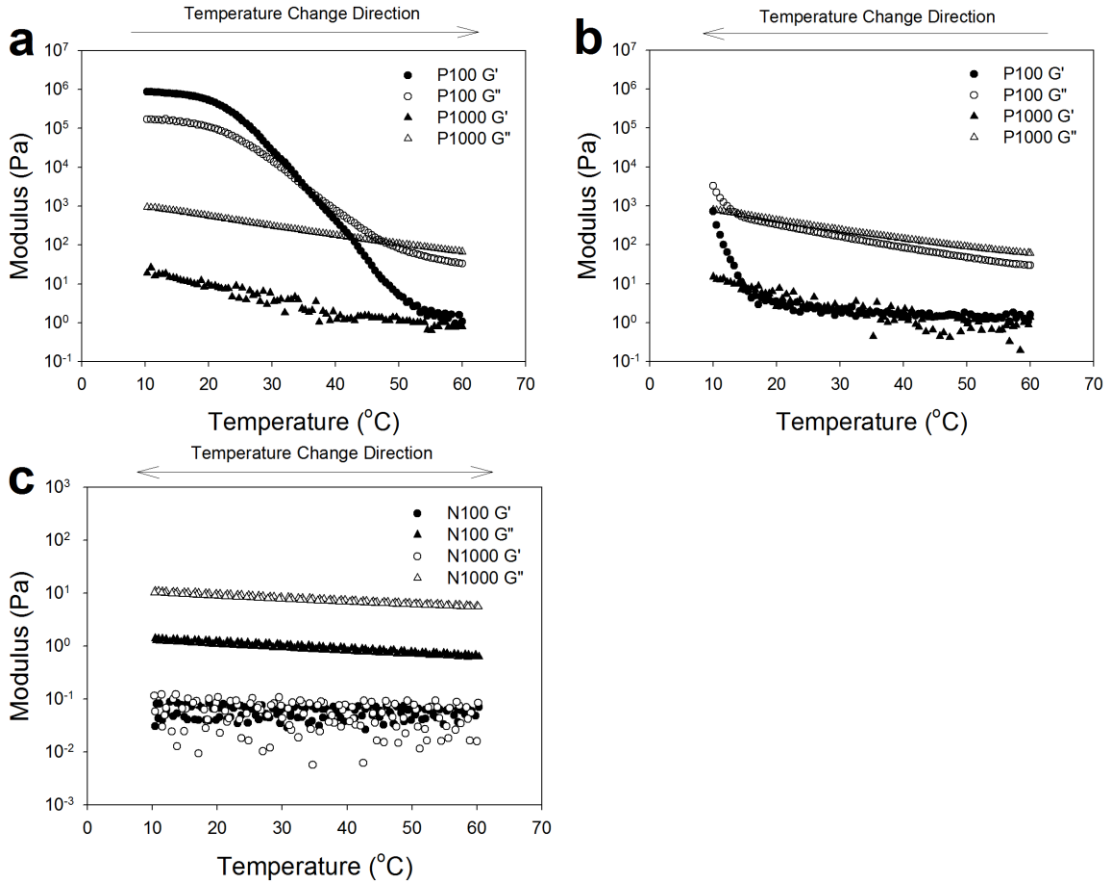

Figure 3.5. P series dynamic moduli as a function of temperature during (a) heating and (b) cooling at 5 °C/min. (c) Analogous N series heating and cooling curves. Adapted with permission from reference [26]. Copyright 2016 Wiley.

3.4.4. Rheological Properties Following a Rapid Thermal Quench

Reproducibility of the rheological data in this study required careful consideration of the development of pyrene associations and formation of nanocrystals, particularly for P100. Figure 3.6 depicts the isothermal rheology for both P100 and P1000 after heating the sample followed by rapid quenching to a given temperature. One can observe the impact of pyrene interactions (and pyrene crystallization in some cases) developing in time by tracking changes in the dynamic storage modulus, G'. As shown in Figure 3.6a,

the formation of pyrene nanocrystals in P100 was affected by the quench temperature with lower quench temperatures resulting in faster crystallization kinetics. In contrast, P1000 (Figure 3.6b) showed only small changes in modulus with time, even when annealing at lower temperatures than P100, indicating little to no crystal formation; this evolution was not observed for N1000. This result is in good agreement with the results discussed in previous sections.

By studying the crystallization kinetics, we concluded that at least 10 minutes of equilibration time was required for full crystallization at 25 °C. This information was critical for performing reproducible rheological experiments and for studying the thermal stimuli-responsiveness of the material in later sections.

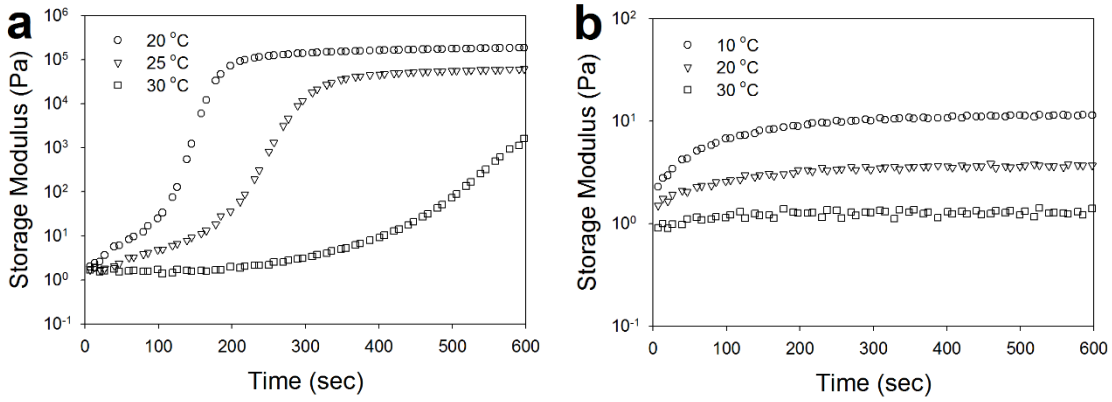

Figure 3.6. Isothermal dynamic rheology following a rapid temperature quench. Storage modulus G' evolution as a function of time and temperature for a) P100 and b) P1000. Adapted with permission from reference [26]. Copyright 2016 Wiley.

3.4.5. Rheological Properties During Programmed Thermal Cycling

Pyrene-functionalized PDMS samples were thermally cycled in order to demonstrate the ability of specimens to repeatedly recover their storage modulus (Figure 3.7). By modifying the temperature program, one can obtain a significant amount of information, such as the importance of pyrene crystallization kinetics, the role of π-π

interactions of the pyrene ends, the effect of MW (related to density of pyrene end interactions), continuity of the stimuli-responsiveness, etc. As shown in the top panels of Figure 3.7a and 3.7b, each sample underwent a variety of cyclic temperature tests. As shown in the study of the crystallization kinetics in the previous section, the storage modulus of P100 in Figure 3.7a did not recover to the original value without a sufficient amount of annealing at 10 °C (i.e., for 10 minutes or more) due to insufficient crystal formation. Even so, only a small deviation in the maximum storage modulus, G', was observed following the first cooling cycle with no subsequent annealing. During the second cooling cycle, where the material was cooled to 10 °C followed by extended annealing for about 10 minutes, the storage modulus G' was restored to its expected state representative of the maximum amount of pyrene crystals formed. A sufficient amount of equilibration time following temperature increases was also crucial for achieving full melting of pyrene crystals and stabilized modulus values. A consequence of this could be observed as a shoulder (e.g., right before the upturn in modulus at about 2,900 s in Figure 3.7a) when the samples were cooled without complete melting during the previous heating cycle. This resulted in some amount of remaining nanocrystals acting as nucleating agents for dissociated pyrene ends which accelerated the subsequent crystallization producing the shoulder. However, if the crystals were completely disassociated/melted during an isothermal period at 60 °C, a sharp increase in G' (e.g., right before the upturn in modulus at about 1,700 s in Figure 3.7a) could be obtained with consistency following the thermal quench. For P1000 (Figure 3.7b), little to no crystals were formed or regenerated during thermal cycling. Nonetheless, the viscosity of P1000 increased dramatically and was far more responsive to repeated temperature cycles compared to N1000 (identical heat cycle data for N100 and N1000 in Figure B.5),

elucidating the impact of modulating π-π interactions of pyrene end-groups with temperature in P1000.

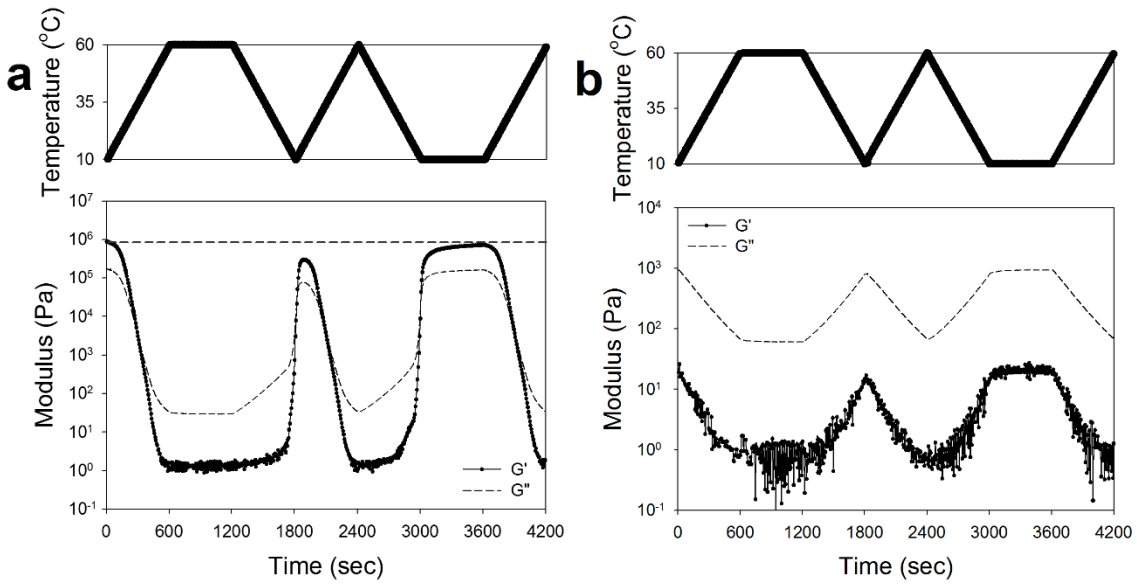

Figure 3.7. Dynamic moduli (bottom) during specified temperature cycles (top) for a) P100 and b) P1000. Dotted horizontal line indicates expected modulus value after extensive thermal annealing times. Adapted with permission from reference [26]. Copyright 2016 Wiley.

By including an isothermal annealing step in every thermal cycle, complete recovery of the rheological properties for P100 and P1000 can be observed over repeated cycles (Figure 3.8). P100 specimens oscillated from solid-like gels to viscous liquids depending on the temperature (the gel point was ca. 35 °C). Considering the very large rheological changes in response to temperature and complete reversibility, such materials could be used effectively as heat sensors, repositionable adhesives or in tunable damping systems.

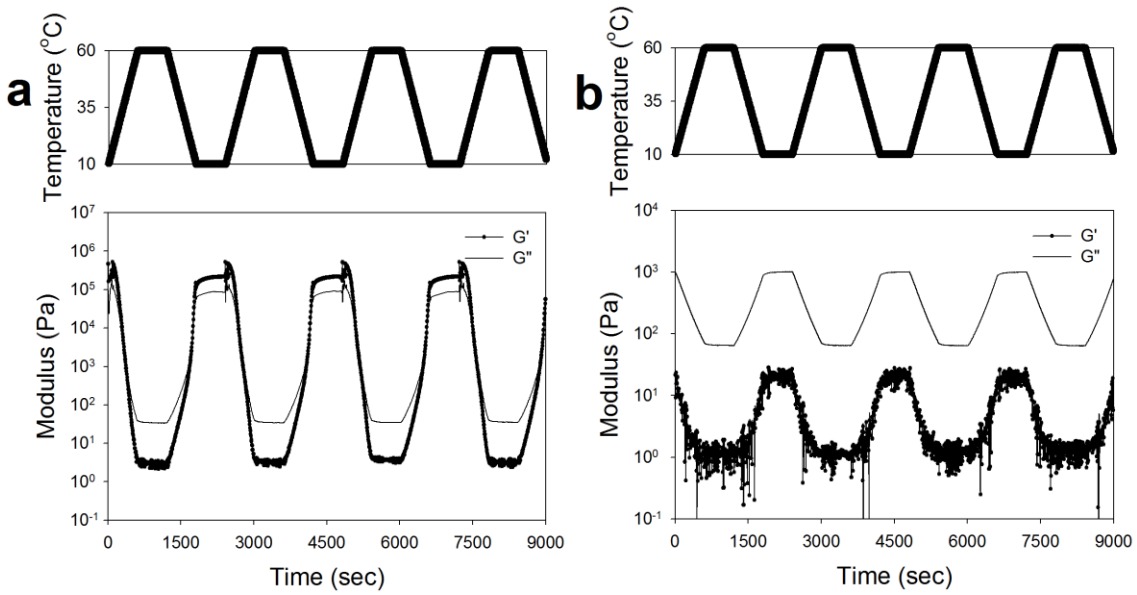

Figure 3.8. Dynamic moduli (bottom) during specified temperature cycles (top) for a) P100 and b) P1000 showing complete reversibility when thermal annealing steps are incorporated into every thermal cycle. Adapted with permission from reference [26]. Copyright 2016 Wiley.

3.4.6. Tunability of the Thermal Properties with Additives

Besides changing the MW of the PDMS precursor as highlighted in previous sections, the thermal properties of pyrene end-functionalized PDMS are tunable to various extents by the incorporation of N series PDMS or OPBA NHS ester additives as shown in Figure 3.9. For P100, the addition of 20 wt % N100 diluted the density of the pyrene ends in the system, which correspondingly reduced the pyrene melting temperature (Figure 3.9a). The addition of 5 wt % free pyrene (OPBA NHS ester) increased the likelihood of preferential interactions of the pyrene chain ends of P100 with free pyrene, which decreased the possibility of pyrene end-group nanocrystal formation. Free pyrene appears to act in a similar manner as excess free salt in an ionomer, which decreases the effective strength of ionic interactions between charge containing polymer chains often changing properties substantially. In this case, the free pyrene is more

mobile than the pyrene attached to chain ends and can effectively "shield" π-π interactions between adjacent pyrene chain ends. The effect of several different concentrations of both PDMS and OPBA NHS esters on the properties of P100 is also included in Figure B.6.

While the thermal properties of P100 were modified with polymeric and small molecule additives reducing T_m or eliminating pyrene nanocrystal formation altogether, GO nanoparticle additives appeared to result in a beneficial enhancement in the thermal properties of both P100 and P1000 (lower thermograms in Figures 3.9a and 3.9b). GO, having an abundance of double bonds and π electrons, can promote the P series pyrene end-groups to bond with their surfaces by π-π interactions. Therefore, incorporating 1 wt % of GO (0.44 vol %) resulted in an increase of $T_{m,Py}$ from 42 °C to 88 °C for P100. For P1000, $T_{m,Py}$ was observed at 86 °C; note that $T_{m,Py}$ was not previously observed in P1000 without additives. Due to this high melting temperature, both P100 and P1000 composites (1 wt % GO) showed solid-like behavior at room temperature after solution casting on a PTFE dish (Figure B.7). Because the material was solid and more robust than the pure P series, more detailed research on the GO composite was performed.

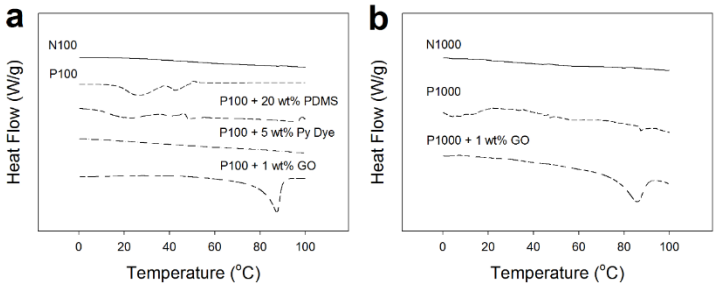

Figure 3.9. DSC thermograms collected upon second heat for (a) N100 precursor and P100 with pure N100 (PDMS), free pyrene (Py Dye; OPBA NHS Ester), or graphene oxide (GO) additives and (b) N1000 precursor and P1000 with GO additive. Adapted with permission from reference [26]. Copyright 2016 Wiley.

3.4.7. Nanocomposite Materials Based on π-π Interactions

The combination of π-π interactions between the P series pyrene end-groups and the GO nanoparticles in a nanocomposite and their expected stimuli-responsiveness to heat, could be beneficial for many potential applications. For GO and P100 composite materials, it was possible to cast this composite into a bar using a silicone elastomer mold as shown in Figure 3.10. The composite was free standing (Figure 3.10b) and flexible (Figure 3.10c), which clearly demonstrated the presence of robust π-π interactions between the polymer and GO. Pure P100, however, was a sticky gel-like solid, and was impossible to detach from the mold.

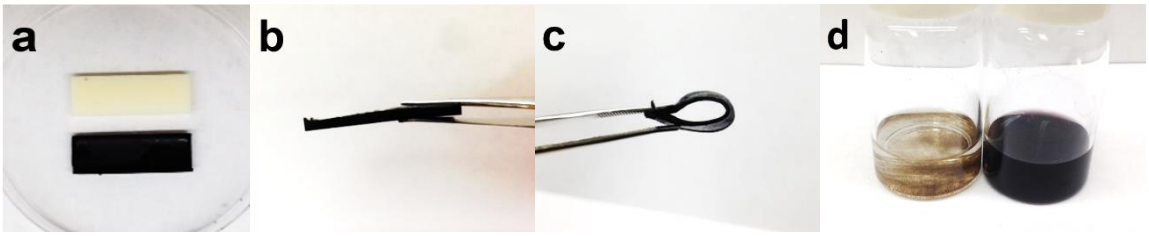

Figure 3.10. Images of P100/1 wt % GO composite materials (a) molded into a bar (bottom) of similar shape to a target test bar (top), (b) free standing/self-supporting bar sample with thickness of ~2 mm and (c) flexibility/elasticity of a bar sample with a thickness of ~0.95 mm. (d) Comparison of GO dispersion in THF with P100 (right) and without P100 (left). Adapted with permission from reference [26]. Copyright 2016 Wiley.

Pyrene end-functionalized PDMS can also be used as a surfactant for dispersing GO in THF solutions. Intrinsically, GOs do not disperse efficiently in THF (Figure 3.10d left). However, when a small amount (0.5 mg) of the pyrene-functionalized PDMS was incorporated in 3ml solution with GOs (Figure 3.10d right), the π-π interactions improved the dispersion and stability of the GO/THF solution. The solution was homogeneous and stable for more than a month.

3.5. CONCLUSIONS

Pyrene-functionalized PDMS materials were synthesized and their thermal and rheological properties were characterized. The process to synthesize pyrene end-functionalized PDMS was not only simple and straightforward, but also showed almost 100% conversion with a high mass yield. The MW of the PDMS, which correlates with pyrene end-group density, affected the thermal and rheological properties significantly. Low MW P100 was a solid gel-like material at room temperature, while high MW P1000 was a viscous liquid-like material. Both samples showed full restoration of rheological properties after thermal cycling when adequate equilibration/annealing time was applied to the material. In addition, the thermal properties of the material were tunable by simply mixing pure PDMS, free pyrene, or GO into pyrene-functionalized PDMS. The melting temperature for pyrene domains in P100 more than doubled by incorporating 1 wt % of GO to the system, and even induced pyrene end-group crystallization in P1000 that did not exhibit pyrene crystals in neat form. The stimuli-responsiveness and tunability of these materials in neat and nanocomposite forms, combined with their simplicity and versatility, makes them attractive for many potential applications.

3.6. REFERENCES

[1] Wojtecki RJ, Meador M a, Rowan SJ. Using the dynamic bond to access macroscopically responsive structurally dynamic polymers. Nat Mater 2011;10:14–27. doi:10.1038/nmat2891.

[2] White EM, Yatvin J, Grubbs JB, Bilbrey J a., Locklin J. Advances in smart materials: Stimuli-responsive hydrogel thin films. J Polym Sci Part B Polym Phys 2013;51:1084–99. doi:10.1002/polb.23312.

[3] Börner HG, Kühnle H, Hentschel J. Making “smart polymers” smarter: modern concepts to regulate functions in polymer science. J Polym Sci Part A Polym Chem 2010;48:1–14. doi:10.1002/pola.23727.

[4] Cabane E, Zhang X, Langowska K, Palivan CG, Meier W. Stimuli-responsive polymers and their applications in nanomedicine. Biointerphases 2012;7:1–27. doi:10.1007/s13758-011-0009-3.

[5] Cordier P, Tournilhac F, Soulié-Ziakovic C, Leibler L. Self-healing and thermoreversible rubber from supramolecular assembly. Nature 2008;451:977–80. doi:10.1038/nature06669.
[6] De Greef TF a., Kade MJ, Feldman KE, Kramer EJ, Hawker CJ, Meijer EW. Spacer-length-dependent association in polymers with multiple-hydrogen-bonded end groups. J Polym Sci Part A Polym Chem 2011;49:4253–60. doi:10.1002/pola.24868.
[7] Chen D, Yoon J, Chandra D, Crosby AJ, Hayward RC. Stimuli-Responsive Buckling Mechanics of Polymer Films. J Polym Sci Part B Polym Phys 2014;52:1441–61. doi:10.1002/polb.23590.
[8] Feldman KE, Kade MJ, De Greef TF a, Meijer EW, Kramer EJ, Hawker CJ. Polymers with multiple hydrogen-bonded end groups and their blends. Macromolecules 2008;41:4694–700. doi:10.1021/ma800375r.
[9] Feldman KE, Kade MJ, Meijer EW, Hawker CJ, Kramer EJ. Phase behavior of complementary multiply hydrogen bonded end-functional polymer blends. Macromolecules 2010;43:5121–7. doi:10.1021/ma1003776.
[10] Lin P, Ma S, Wang X, Zhou F. Molecularly Engineered Dual-Crosslinked Hydrogel with Ultrahigh Mechanical Strength, Toughness, and Good Self-Recovery. Adv Mater 2015;27:2054–9. doi:10.1002/adma.201405022.
[11] Burnworth M, Tang L, Kumpfer JR, Duncan AJ, Beyer FL, Fiore GL, et al. Optically healable supramolecular polymers. Nature 2011;472:334–7. doi:10.1038/nature09963.
[12] Sun J-Y, Zhao X, Illeperuma WRK, Chaudhuri O, Oh KH, Mooney DJ, et al. Highly stretchable and tough hydrogels. Nature 2012;489:133–6. doi:10.1038/nature11409.
[13] Parviz D, Das S, Ahmed HST, Irin F, Bhattacharia S, Green MJ. Dispersions of non-covalently functionalized graphene with minimal stabilizer. ACS Nano 2012;6:8857–67. doi:10.1021/nn302784m.
[14] Parviz D, Yu Z, Hedden RC, Green MJ. Designer stabilizer for preparation of pristine graphene/polysiloxane films and networks. Nanoscale 2014;6:11722–31. doi:10.1039/C4NR01431F.
[15] Kim SD, Torkelson JM. Nanoscale confinement and temperature effects on associative polymers in thin films: Fluorescence study of a telechelic, pyrene-labeled poly(dimethylsiloxane). Macromolecules 2002;35:5943–52. doi:10.1021/ma0200322.
[16] Jones BA, Torkelson JM. Crystallization and Enthalpy Relaxation of Physically Associating, End-Linked Polymer Networks: Telechelic Pyrene-Labeled Polydimethylsiloxane. Polym Bull 2004;51:411–8. doi:10.1007/s00289-004-0241-9.
[17] Jones B a., Torkelson JM. Large melting point depression of 2-3-nm length-scale nanocrystals formed by the self-assembly of an associative polymer: Telechelic, pyrene-labeled poly(dimethylsiloxane). J Polym Sci Part B Polym Phys 2004;42:3470–5. doi:10.1002/polb.20228.

[18] Martinez CR, Iverson BL. Rethinking the term “pi-stacking.” Chem Sci 2012;3:2191. doi:10.1039/c2sc20045g.
[19] Grimme S. Do special noncovalent pi-pi stacking interactions really exist? Angew Chemie - Int Ed 2008;47:3430–4. doi:10.1002/anie.200705157.
[20] Zhang Y, Liu C, Shi W, Wang Z, Dai L, Zhang X. Direct measurements of the interaction between pyrene and graphite in aqueous media by single molecule force spectroscopy: Understanding the π-π interactions. Langmuir 2007;23:7911–5. doi:10.1021/la700876d.
[21] Akbarzadeh K, Bressler DC, Wang J, Gawrys KL, Gray MR, Kilpatrick PK, et al. Association behavior of pyrene compounds as models for asphaltenes. Energy and Fuels 2005;19:1268–71. doi:10.1021/ef0496698.
[22] Zhang Y, Yuan S, Zhou W, Xu J, Li Y. Spectroscopic evidence and molecular simulation investigation of the pi-pi interaction between pyrene molecules and carbon nanotubes. J Nanosci Nanotechnol 2007;7:2366–75. doi:10.1166/jnn.2007.412.
[23] Burattini S, Greenland BW, Merino DH, Weng W, Seppala J, Colquhoun HM, et al. A healable supramolecular polymer blend based on aromatic π-π Stacking and hydrogen-bonding interactions. J Am Chem Soc 2010;132:12051–8. doi:10.1021/ja104446r.
[24] Li M-C, Ho R-M, Lee Y-D. Photo-induced excimer formation of pyrene-labeled polymers for optical recording. J Mater Chem 2011;21:2451. doi:10.1039/c0jm03543b.
[25] Ha H, Shanmuganathan K, Ellison CJ. Mechanically Stable Thermally Crosslinked Poly(acrylic acid)/Reduced Graphene Oxide Aerogels. ACS Appl Mater Interfaces 2015;7:6220–9. doi:10.1021/acsami.5b00407.
[26] Ha H, Shanmuganathan K, Fei Y, Ellison CJ. Thermal stimuli-responsive behavior of pyrene end-functionalized PDMS through tunable Π-Π interactions. J Polym Sci Part B Polym Phys 2016;54:159–68. doi:10.1002/polb.23805.
[27] Carvalho SP, Lucas EF, González G, Spinelli LS. Determining Hildebrand Solubility Parameter by Ultraviolet Spectroscopy and Microcalorimetry. J Braz Chem Soc 2013;24:1998–2007. doi:10.5935/0103-5053.20130250.
[28] Roth M. Solubility parameter of poly(dimethyl siloxane) as a function of temperature and chain length. J Polym Sci Part B Polym Phys 1990;28:2715–9. doi:10.1002/polb.1990.090281317.

Chapter 4: Synthesis and Gas Permeability of Highly Elastic Poly(dimethyl siloxane)/Graphene Oxide Composite Elastomers Using Telechelic Polymers[3]

4.1. Overview

While the polymer/GO composite systems studied in previous chapters all utilized secondary interactions for tailoring properties (the XPAA/GO aerogel system employed both secondary and covalent bonds), expanding the toolbox for introducing covalent bonds into the composite architecture could reveal an even greater range of properties. To this end, this chapter illustrates that amine functional groups on the ends of telechelic poly(dimethylsiloxane) (PDMS) can undergo post-processing reactions with surface epoxy groups on graphene oxide (GO) to form a robust elastomer during simple heating. In these materials, GO acts both as a nanofiller which reinforces the mechanical properties and participates as a multifunctional crosslinker, thereby promoting elastic properties. Experiments indicate that the telechelic PDMS/GO elastomer is highly crosslinked (e.g., more than 75 wt % is a non-dissolving crosslinked gel) but highly flexible such that it can be stretched up to 300 % of its original length. Finally, the PDMS/GO elastomer was tested as a single gas barrier membrane and gas permeability was decreased ~ 45 % by incorporating 1 wt % (0.43 vol %) GO, thereby highlighting its potential use in practical applications.

[3] Ha H (Designed and performed most of the experiments, wrote and edited the paper), Park J, Ha K, Freeman BD, Ellison CJ. Synthesis and gas permeability of highly elastic poly(dimethylsiloxane)/graphene oxide composite elastomers using telechelic polymers. Polymer 2016;93:53–60. doi:10.1016/j.polymer.2016.04.016.

4.2. INTRODUCTION

In recent years, flexible polymers have become increasingly important for many applications that impact daily life, including wearable devices [1–3], flexible displays [4–6], and devices for monitoring physiological signals [7–9], to name a few. These high-end applications typically require the use of an elastomer or rubber, such as crosslinked PDMS, to impart flexibility and mechanical robustness in addition to comfort; all are important features for interfacing with the human body. While there exist commercial choices for PDMS elastomer precursors, such PDMS precursors are generally high in viscosity, limited to several grades and the recipe for preparing the final elastomer can be complex [10–12]. Therefore, the development of new methods for forming elastomers with only a few simple components which exhibit unique combinations of properties (e.g., electrically conductive but flexible and mechanically robust, etc.) could be very useful.

Herein, we report a simple process for creating a strong and flexible elastomer from a reactive mixture of GO and functional telechelic (i.e., both ends functionalized) PDMS. The resulting composite has excellent mechanical properties but also serves as an effective and potentially economical gas barrier membrane for industrial use. For context, materials presenting a high barrier to oxygen permeation are typically very important for the applications listed above because flexible devices often contain organic components to promote flexibility that can be particularly susceptible to oxidative degradation.

For a number of reasons, the telechelic PDMS/GO composite elastomer described in this study can be considered to be unique when compared alongside other crosslinked PDMS materials. For instance, a distinguishing characteristic of the present elastomer is that it not only possesses the traditional properties of crosslinked PDMS materials, such as flexibility and good mechanical integrity, but it can also be made by simple and

scalable methods using two low-cost materials: graphite and telechelic polymer. In contrast, conventionally crosslinked PDMS elastomers are typically synthesized by one of three methods: platinum-catalyzed addition, vinyl-peroxide, or condensation curing [13]. All of these methods require a catalyst to perform the reaction, accompanied with a range of several different chemical additives, sometimes including fillers such as silica [11,12]. Many prior studies have investigated the tuning of physical properties, including mechanical, electrical, and dielectric properties, of PDMS materials by adjusting the crosslink density [14], adding fillers such as silica [15], clays [16], CNTs [17], graphene derivatives [18] or other polymers [19]. Generally, these additional additives are most commonly physically intermixed with PDMS with no chemical bonding between the PDMS and additives. In contrast, the preparation of telechelic PDMS/GO composite elastomers in this study incorporates a GO filler that also participates as a multi-functional crosslinker, which facilitates formation of the final covalently bonded macromolecular network.

While neat PDMS is highly gas permeable, the addition of impermeable platelet-like fillers such as GO can dramatically inhibit gas permeation. Recent studies of gas barrier membranes using different graphene derivatives have focused on coating the surface of flexible substrates (such as PDMS films or sheets) with a thin layer of graphene or GO that is typically weakly bound by noncovalent adhesion forces [6,20,21]. Graphene coated membranes could be susceptible to sections of the coating delaminating from the flexible substrate after repeated stress, bending or upstream/downstream pressure cycles [6,20,22]. Other potential sources of damage from environmental exposure of the active graphene or GO coating layer, such as irreversible adsorption of undesired contaminants during prolonged use, could be possible. In contrast to this coating approach, the elastomer described herein forms a covalent macromolecular

network between the flexible component (PDMS) and the gas impermeable component (GO) producing a dense and homogeneous barrier membrane. In summary, from a membrane engineering perspective, we believe this composite provides for the possibility of a cost-effective, high performance gas barrier membrane.

4.3. EXPERIMENTAL SECTION

4.3.1. Materials

In order to synthesize PDMS/GO elastomers, three components were combined: telechelic PDMS as the base material, GO as both a filler and multifunctional crosslinker, and tetrahydrofuran (THF; Fisher Chemical) as a solvent. Aminopropyl terminated telechelic PDMS with a viscosity of 1,000 cSt (M_n = 25,000 g/mol, DMS-A31, henceforth referred to as N1000) and 2,000 cSt (M_n = 30,000 g/mol, DMS-A32, henceforth referred to as N2000) were purchased from Gelest and used without any further purification. For comparison, silanol terminated PDMS with a viscosity of 1,000 cSt (M_n = 26,000 g/mol, DMS-S31) and epoxypropoxypropyl terminated PDMS with a viscosity of 15 cSt (M_n = 550 g/mol, DMS-E11) were also purchased from Gelest and used as received. GOs were synthesized by the modified Hummer's method as described in chapter 2 [23], where sulfuric acid, potassium permanganate, hydrogen peroxide, and hydrochloric acid were purchased from Sigma-Aldrich and used as-received. Pre-oxidized graphite from Bay Carbon Inc. (SP-1) was used as the starting material to synthesize GOs. The nominal number average particle size of the SP-1 graphite was approximately 19.3 μm [24], and it has been reported by others that the GO sheet size reduces to an average value of 8.3 μm when this grade of graphite is oxidized using the modified Hummer's method with an oxidation temperature of 35 °C [25].

4.3.2. Fabrication of PDMS/GO Elastomers

First, a known amount of telechelic PDMS (for 1 wt % GO composites, 990 mg) was dissolved in THF (6 ml) while stirring to ensure complete dissolution of the polymers. Then, dried GO (10 mg) was suspended in the solution with vigorous stirring, and a homogeneous dispersion of GO in this solution was promoted by sonication using a 400 W probe sonicator (Branson Digital Sonifier 450) with 10 % amplitude for 10 min (24 kJ) in an ice bath. It is noteworthy to point out that, although THF is not a good solvent for GO, amine terminated telechelic PDMS can effectively act as a surfactant to assist in dispersing GO homogeneously in THF through hydrogen bonding between amine ends and oxygen containing groups on GO surfaces. A good dispersion after sonication was confirmed by examining the residual liquid film in the vial while rolling the vial containing the solution and after pouring the majority of the solution into a PTFE dish for solution casting. In either case, the liquid film in the vial was essentially transparent (although brownish-black from the GO content) for all solution concentrations and no aggregates could be identified with the naked eye. This solution was immediately poured into a Teflon dish and covered in order to slowly evaporate the solvent thereby solution casting a film at room temperature. Solvent was evaporated for at least 2 days and then the sample was vacuum dried at room temperature for an additional day to make a homogenous PDMS/GO uncrosslinked liquid sol. In order to form a crosslinked elastomer, the sol precursor was heated to 160 °C in a vacuum oven for 24 hours and cooled slowly to room temperature before use.

For one of the gas permeation tests, a reference sample (neat PDMS elastomer) was synthesized by reacting aminopropyl terminated telechelic PDMS and epoxypropoxypropyl terminated telechelic PDMS. A detailed explanation of how this freestanding, neat PDMS elastomer was synthesized is summarized in Appendix C.

4.3.3. Characterization of PDMS/GO Elastomers

The chemical crosslinking reaction between PDMS and GO was investigated using Fourier transform infrared spectroscopy (FTIR; Thermo Nicolett, 6700) with a scan size (resolution) of 2 cm^{-1} collected over 256 scans per sample. Solvent uptake and gel content of each composite elastomer were calculated using Equation 1 and 2 below where 'w' indicates weight, according to ASTM D2765 test method C. THF was used as the solvent to dissolve away unreacted soluble polymers.

$$Solvent\ Uptake\ (\%) = \frac{w_{after\ swell} - w_{before\ swell}}{w_{before\ swell}} \times 100 \quad (1)$$

$$Gel\ Content\ (\%) = \frac{w_{after\ swell\ and\ dried\ in\ vacuum}}{w_{before\ swell}} \times 100 \quad (2)$$

All rheological experiments were conducted on a shear rheometer (TA Instruments, AR-2000EX) using an 8 mm parallel upper plate and a Peltier lower plate fixture for temperature control with a gap of 500 μm. First, a strain sweep was conducted to identify the linear viscoelastic regime at 25 °C in the range of 0.01-10 % strain at a frequency of 1 Hz. A frequency sweep was then conducted at 25 °C in the range of 0.01-10 Hz with 0.1 % strain. Temperature sweeps were conducted from 25 °C to 100 °C with 5 °C step changes using both 0.1 % strain and a frequency of 1 Hz. Stress relaxation tests were conducted by subjecting the sample to an initial strain of 10 % and 20 %. In order to measure the mechanical properties of the composite elastomers, microtensile specimens were prepared by solution casting on a mold (i.e., to produce a dog bone sample with a gauge length of 22 mm, width of 4.8 mm and thickness of about 0.7 mm) satisfying ASTM D1708-13 standards. An Instron (model 5966) equipped with a 1 kN load cell was used with a strain rate of 10 mm/min (i.e., at our gauge length this is a nominal strain rate

equivalent to 50 mm/min for ASTM D638 standard samples, which is the recommended speed for rubber samples) and samples were tested in triplicate.

Thermal properties of the elastomers were characterized by differential scanning calorimetry (DSC; Mettler Toledo DSC1). Heating and cooling rates of 10 °C/min were used for all experiments, and the second heating curve was used for the glass transition temperature (T_g) analysis to erase thermal history. GO was further characterized using X-ray photoelectron spectroscopy (XPS; Kratos) to compare the composition of the GO before and after annealing. CasaXPS software (v 2.3.16) was used to perform curve fitting in which a Shirley background was assumed. The dispersion of GO in the composite material was determined by optical microscopy (OM; Olympus BX60) using a microtomed sample on a 400 mesh Cu grid. Sectioning was performed by a benchtop microtome (RMC Products, PT-XL Power Tome) with a diamond knife where the temperature of the diamond knife and the sample holder were both set to -150 °C. According to the images (supporting information), all of the composite materials considered in this study showed good dispersion of GO without any noticeable large aggregates.

4.3.4. Single Gas Permeation Measurements

Single gas, including H_2, O_2, N_2, CH_4 and CO_2, transport properties were measured using the constant volume, variable pressure method at 35 °C with ultra-high purity grade gases from Airgas. A 1000 psig pressure transducer (Honeywell Sensotec, Model STJE) was used to measure the upstream pressure in the system. A 10 Torr capacitance manometer (MKS, Baratron 626 A) was used to measure the downstream pressure, and the downstream pressure was kept below 10 Torr using a vacuum pump. All data were recorded using National Instruments Lab-VIEW software. Permeability,

which is an intrinsic property of a specific material to a specific permeate, was expressed in barrer units, where 1 barrer equals to 10^{-10} cm^3(STP) cm/cm^2 s cm Hg. The average thickness of the sample was measured using a dial gauge (Mitutoyo, Absolute digimatic indicator) by sandwiching a sample in between two thin metal plates (each metal plate thickness = 0.05 mm). Metal plates were used to prevent samples from being compressed by the tip of the dial gauge during measurement. Thicknesses for the neat PDMS elastomer and telechelic PDMS N1000/1 wt % GO elastomer were 0.998 ± 0.021 mm and 0.354 ± 0.010 mm, respectively.

4.4. Results and Discussion

To fully understand the chemical nature of the thermally crosslinked telechelic PDMS/GO elastomers, a fundamental investigation regarding the reaction between amine terminated telechelic PDMS and GO was pursued first.

4.4.1. Proposed Reaction and Evidence of Crosslinking

As shown in Figure 4.1a, only two materials were used to form the highly elastic elastomer, the first being amine terminated telechelic PDMS, which contains a primary amine attached to each end of the polymer chain. As discussed in chapter 1, the second material, GO, contains numerous oxygen-containing functional groups, including hydroxyls, carboxylic acids, and epoxides, on the surface of the GO sheets [26]. XPS data supports the fact that hydroxyls and epoxides are present in larger proportion than other functionalities. Once the two materials are mixed together and sufficient energy is applied, in this case heat, an epoxide on GO can react with the nearest primary amine on PDMS by a ring-opening reaction. Such a reaction results in the formation of ethanolamine covalent bonds between the telechelic polymer ends and the epoxy groups

on the surface of GO, as shown in Figure 4.1b. This nucleophilic substitution reaction has been proposed and demonstrated previously by other groups when functionalizing GO surfaces with amines [27,28] as well as for synthesizing chemically crosslinked nylons [29,30], epoxy composites [31–33], and polymer/GO papers [34,35]. However, to the best of our knowledge, no research implementing telechelic polymers with GOs to form a controllable, highly elastic composite material has been reported [20]. It is worth noting that we have also confirmed this reaction proceeds similarly for PDMS materials containing secondary amide end groups [36].

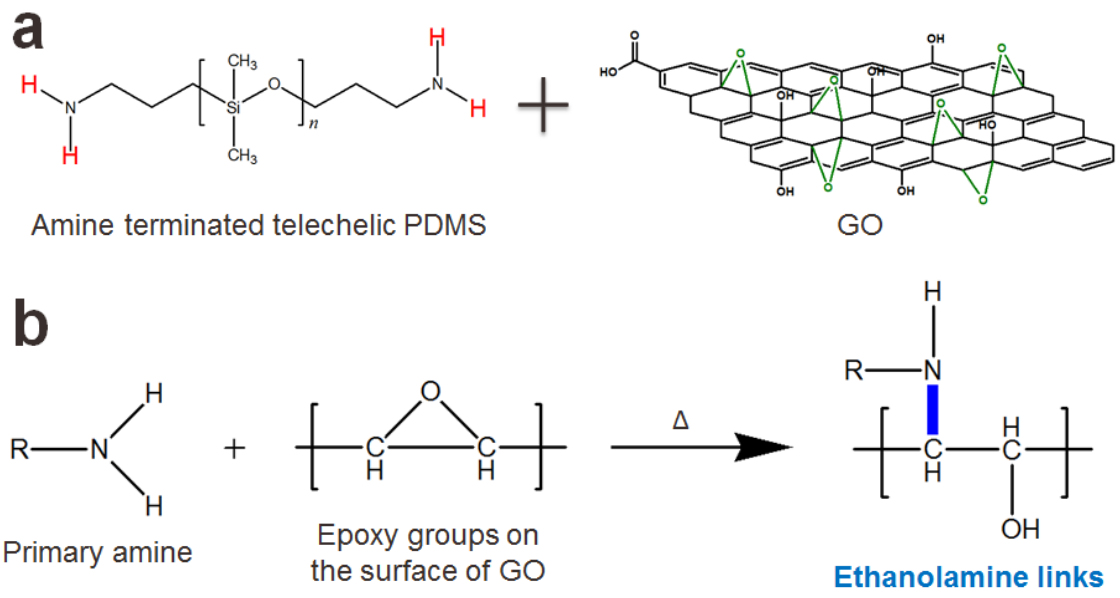

Figure 4.1. (a) Chemical structures of the two materials used in this study. Each material's active sites are capable of reacting with complementary functional groups (colored) on the other component. (b) The anticipated reaction mechanism that produces elastomers in this study. No other byproducts are formed during the crosslinking reaction. Adapted with permission from reference [37]. Copyright 2015 Elsevier.

There are three possible scenarios for amine terminated telechelic PDMS to react with GOs: two ends react with two different GO sheets, one end reacts with one GO sheet

while the other end forms a dangling strand and remains unreacted, or two ends react with the same GO sheet forming a loop. Considering the high gel content obtained for various samples (which will be discussed in more detail in a later section), it is postulated that the majority of the reaction takes place by forming a crosslink between two different GO sheets, since the latter two possibilities would not contribute to enhancing the gel content and mechanical properties of the composite. Given that reaction is only possible at chain ends, telechelic polymers offer the opportunity to produce elastomers with a predefined and tailorable molecular weight between crosslink points. Considering that this reaction only involves polymer end-groups, the versatility and universality of this crosslinking reaction could be easily demonstrated by applying it to other repeat unit chemistries extending this approach to polymers that are amorphous or semicrystalline, hydrophobic or hydrophilic, synthesized by either addition or step growth polymerizations, etc. Finally, due to the simplicity of the reaction and the fact that no byproducts are formed during crosslinking, it is expected that this facile method could be scalable to mass produce composite materials in a cost-effective way.

As shown in Figure 4.2, simply annealing the solution cast telechelic PDMS/GO composite film in vacuum for 24 hours resulted in a material that was freely standing, highly flexible and mass producible in different sizes and shapes (note the larger size in Figure 4.2f). The transformation of a viscous sol to a self-supporting solid elastomer provided indirect evidence of a reaction forming covalent bonds between the polymer and GO. For comparison, a silanol terminated telechelic PDMS/GO composite remained a soluble viscous liquid even after annealing at high temperature (Figure C.1). This clearly demonstrates the importance of complementary reactive functionalities for performing the reaction that leads to the final elastomers.

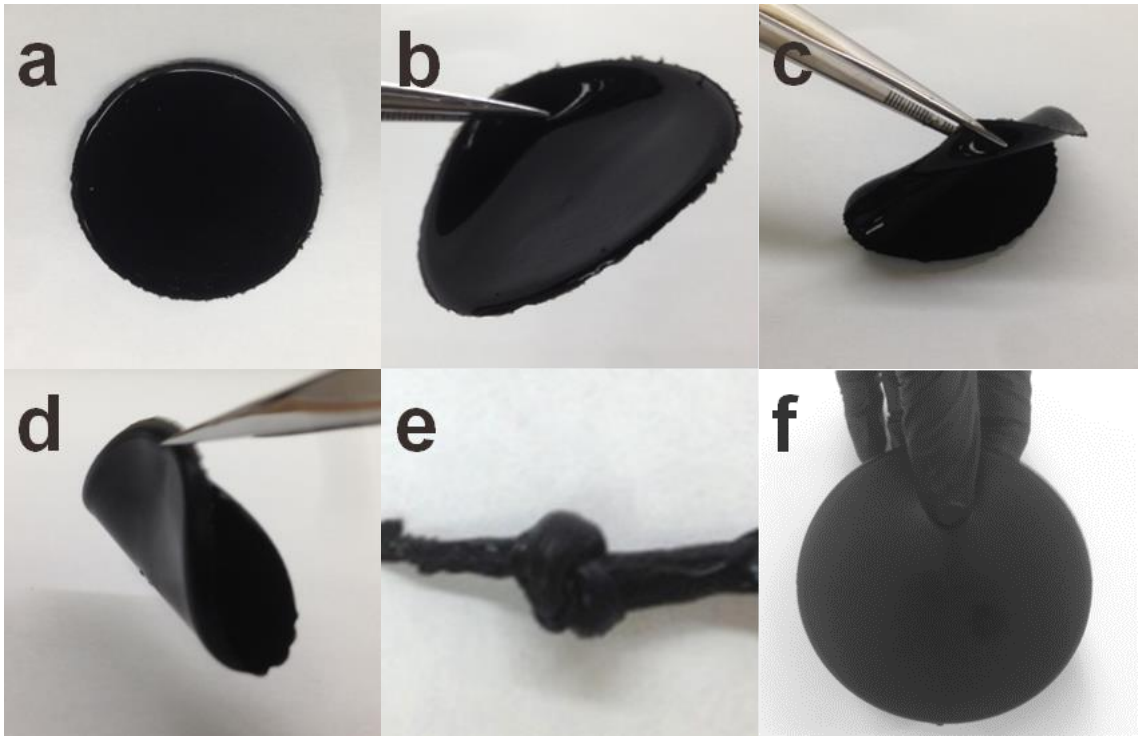

Figure 4.2. Images of N1000/1 wt % GO elastomers. (a) As prepared material is not only (b) freestanding, but also (c) bendable and (d) flexible. (e) The material is elastic enough to make a knot. (a-e) shows a N1000/1 wt % GO elastomer disc 38 mm in diameter, while (f) is 10 cm in diameter. Adapted with permission from reference [37]. Copyright 2015 Elsevier.

While the occurrence of the crosslinking reaction is evidenced by the images in Figure 4.2, absorbance spectra obtained using FTIR provide more direct evidence of the chemical changes associated with this reaction (Figure 4.3). To understand the crosslinking reaction and formation of the ethanolamine linkage, the telechelic PDMS/GO mixture was investigated before and after annealing. As expected, the majority of the intense peaks in the spectra were related to the PDMS main chain repeat units; detailed peak assignments for Figure 4.3a are tabulated in Appendix C in Table C.1. For the N1000 telechelic PDMS used in Figure 4.3, with amine ends present at approximately 0.6 mol % (i.e., 0.12 wt %), the 1500-1700 cm^{-1} region of the spectra was

examined in further detail in Figure 4.3b. Before annealing, the peak associated with N-H bending was assigned at 1600 cm^{-1} for both N1000 PDMS and N1000 PDMS/1 wt % GO sol samples. However, after annealing the sol to crosslink the sample producing an elastomer, a significant fraction of the N-H bending peak disappeared, indicating that the majority of the primary amine end groups were reacted during this step. In addition, due to a known thermal annealing induced reduction reaction of GO to reduced GO, a stronger C=C ring stretching peak at 1580 cm^{-1} was formed for the N1000 PDMS/1 wt % GO elastomer sample. A separate case study on the effect of heat on the transformation of GO to reduced GO is provided in Figure C.2. Because the FTIR spectra after extended annealing were nearly identical to those after 24 hours of annealing at 160 °C, it can be concluded that the reaction was essentially completed within 24 hours.

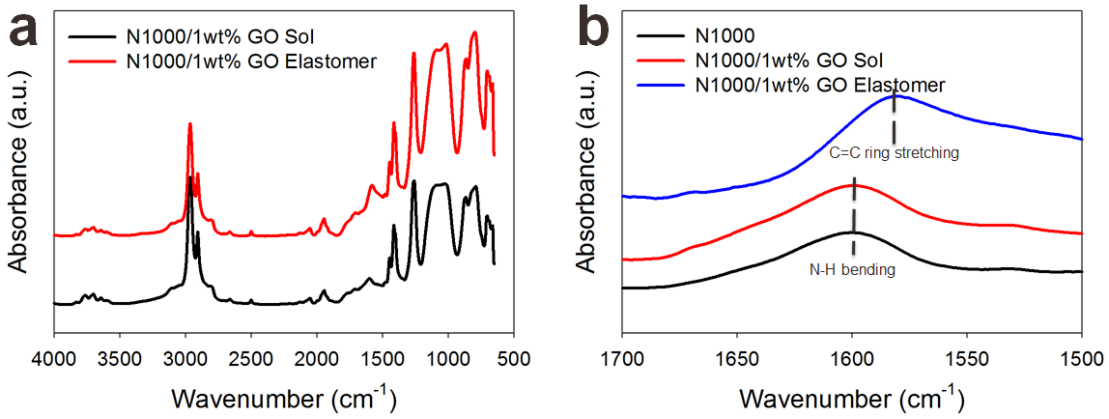

Figure 4.3. FTIR spectra before (sol) and after (elastomer) thermal annealing. (a) Full scan and (b) selected region from 1500-1700 cm^{-1}. FTIR spectra have been shifted vertically for clarity but are otherwise on the same scale. Adapted with permission from reference [37]. Copyright 2015 Elsevier.

Another method to confirm the formation of chemically crosslinked elastomers is to measure the swelling ratio and gel content of the composite material. By controlling the content of GO and the M_n of the PDMS polymer incorporated in this system, the gel

crosslink density can be altered effectively (Table 4.1). For example, increasing the GO content resulted in the introduction of more crosslinking sites and, as a result, dramatically increased the gel content and decreased the solvent uptake of the elastomers. On the other hand, as the M_n of the PDMS was increased from 25 to 30 kg/mol, the mol fraction of the amine end groups was reduced from 0.6 % to 0.5 %. Table 4.1 shows that the degree of swelling expectedly increased and gel fraction decreased; the likelihood of amines reacting with the surface epoxy groups of GO would be expected to decrease in this situation reducing crosslinking density. An associated factor is that the mobility of a higher M_n polymer could also be slightly lower due to increased entanglements and viscosity, which would also be expected to decrease the crosslink density.

Table 4.1. Solvent uptake and gel content for elastomer samples measured as a function of PDMS molecular weight and GO content. The indicated error is standard deviation of at least 5 separate samples. Adapted with permission from reference [37]. Copyright 2015 Elsevier.

Sample	$M_{n,PDMS}$ (g/mol)	Solvent uptake (%)	Gel content (%)	Soluble fraction (%)
N1000/1 wt % GO	25,000	711 ± 26	77.0 ± 1.7	~23
N1000/2 wt % GO	25,000	334 ± 17	89.2 ± 0.8	~11
N2000/1 wt % GO	30,000	836 ± 31	72.1 ± 1.8	~28
N2000/2 wt % GO	30,000	421 ± 4	84.4 ± 1.3	~16

It is noteworthy that the viscosity of the telechelic PDMS component, which is directly related to the M_n of the polymer, plays an important role in forming a homogeneous crosslinked material following solution casting and thermal annealing. Low viscosity telechelic PDMS, such as 50 cSt and 100 cSt, formed a material showing a

gradient in elasticity through the film thickness direction (data not shown). This occurs as GO (i.e., the highly functional crosslinkers) settled to the bottom of the PTFE dish, resulting in higher crosslink density at the bottom while essentially leaving the top as a viscous mostly amine terminated PDMS liquid. A similar phenomena was observed previously by Clarizia and coworkers for PDMS/zeolite composite materials [38]. This can be avoided by using telechelic PDMS with higher molecular weight and viscosity to slow or prevent settling of GO.

4.4.2. Physical Properties of Telechelic PDMS/GO Elastomers

Even though extensive information on the formation of the crosslinked network was obtained from FTIR and gel content measurements, rheological and mechanical properties provide additional understanding of both the elastomer and its precursor. Thus, the dynamic modulus for PDMS N1000/1 wt % GO sol and elastomer samples were investigated in more detail as a function of the % strain (Figure 4.4a), frequency (Figure 4.4b), temperature (Figure 4.4c), and during stress relaxation for 10 % and 20 % step strain (Figure 4.4d).

As shown in Figure 4.4a-c, the elastomer exhibited a storage modulus (G') that was approximately an order of magnitude higher than the loss modulus (G") over a wide range of strains, frequencies, and temperatures, indicative of stable, solid-like viscoelastic behavior. In contrast, the PDMS/GO uncrosslinked sol exhibited liquid-like behavior (G" being higher than G') over the range of interest and even showed considerable changes across both the frequency and temperature sweep, which is clearly distinguishable from that of the elastomer sample. A stress relaxation test also confirmed the elastomers as viscoelastic solids, which is in agreement with the aforementioned rheological observations shown in Figure 4.4a-c. After relatively short relaxation times, the stress

relaxation curve reached an asymptotic equilibrium stress of approximately 20 kPa. On the other hand, the uncrosslinked liquid sol composites exhibited complete stress relaxation within a few seconds.

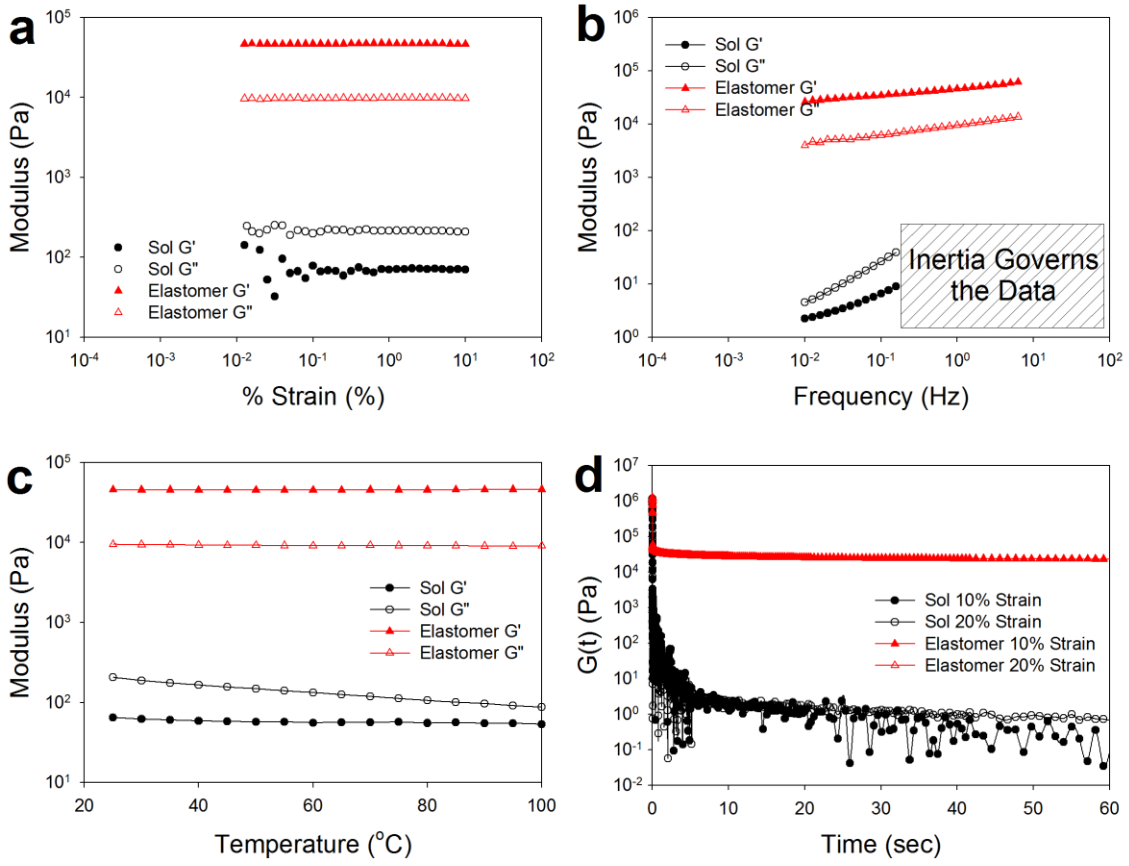

Figure 4.4. Comparison in rheological properties between N1000/1 wt % GO uncrosslinked sol and elastomer samples. (a) Oscillatory strain sweep, (b) oscillatory frequency sweep, (c) oscillatory temperature sweep, and (d) stress relaxation results. During the oscillatory frequency sweep in (b), the N1000/1 wt % sol sample's raw phase reached the instrument limit (> 150°). Therefore, data in the region of uncertainty is not shown. Adapted with permission from reference [37]. Copyright 2015 Elsevier.

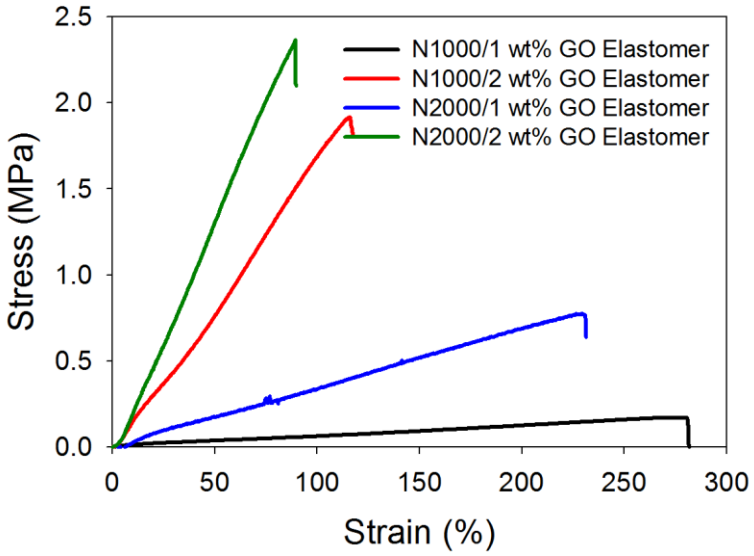

Figure 4.5. Representative stress-strain curves of telechelic PDMS/GO elastomers. Adapted with permission from reference [37]. Copyright 2015 Elsevier.

The mechanical integrity of the elastomer was also investigated using a universal tensile test. As expected, increasing the GO concentration resulted in a higher tensile strength while reducing the elongation at break (see stress-strain curve in Figure 4.5 and data tabulated in Table 4.2). It is noteworthy that the precursor PDMS and PDMS/GO sol are liquids, and it was therefore impossible to perform such experiments on these samples. This result highlights the effect of chemical crosslinks between the polymer and GO, where other studies on physically mixed thermoplastic polyurethane/octadecylamine functionalized GO composites showed no reinforcement at loading levels below 2.5 vol % [39]. Although the gel content for high M_n PDMS (N2000) composites was slightly lower than that of low M_n PDMS (N1000, related data in Table 4.1), the N2000 samples exhibited moderately higher tensile strength. We hypothesize that a major contributing factor could be related to trapped entanglements between the reacted PDMS

chain ends that could act as physical crosslinks within the network increasing the tensile strength.

Table 4.2. Tensile properties of telechelic PDMS/GO elastomers depending on the M_n of the telechelic PDMS and GO content. The indicated error is standard deviation of at least 3 separate samples. Adapted with permission from reference [37]. Copyright 2015 Elsevier.

Sample	Tensile strength at break (MPa)	Elongation at break (%)
N1000/1 wt % GO	0.15 ± 0.02	280 ± 12
N1000/2 wt % GO	2.20 ± 0.17	136 ± 17
N2000/1 wt % GO	0.77 ± 0.02	232 ± 8
N2000/2 wt % GO	2.33 ± 0.40	98 ± 16

In general, the physical and mechanical properties of the telechelic PDMS/GO elastomers are very important aspects when considering their use as gas barrier membranes. Depending on the specific application, dense polymer gas barrier membranes may be subjected to high pressures (over 10 atm) with high gas flux penetrating through the thin film membrane [40]. It is critical for the membrane to withstand both external pressure and gas flow without forming pinholes or rupturing completely.

4.4.3. Application as an Effective Gas Barrier Membrane

There is a strong demand for enhancing the gas barrier properties of polymer nanocomposite materials for prolonging lifetimes of organic electronics or packaged food, among other applications. One of the common approaches to improve the gas

barrier properties is to optimize the dispersion of the filler material using suitable processing procedures. Most of the polymer/GO membrane research has involved preparation of samples by solution mixing, in situ polymerization, and melt mixing [20]. While the high barrier performance of these materials has been demonstrated previously by physically mixing two or more components to obtain synergistic properties, a number of recent studies have focused on coating a thin layer of graphene or graphene derivative on top of a flexible substrate, or preparing a free-standing graphene derivative membrane [21]. Such approaches accordingly concentrate the graphene forming a denser layer of gas impermeable filler but they can introduce new challenges such as requiring careful handling to prevent the filler from fracturing or delaminating from the substrate. Exploiting the fact that the telechelic PDMS/GO elastomers exhibit excellent mechanical integrity with the PDMS component effectively encapsulating and protecting the gas impermeable GO from external stress and environmental damage, we envisioned that this material would perform well as a gas barrier or separation membrane.

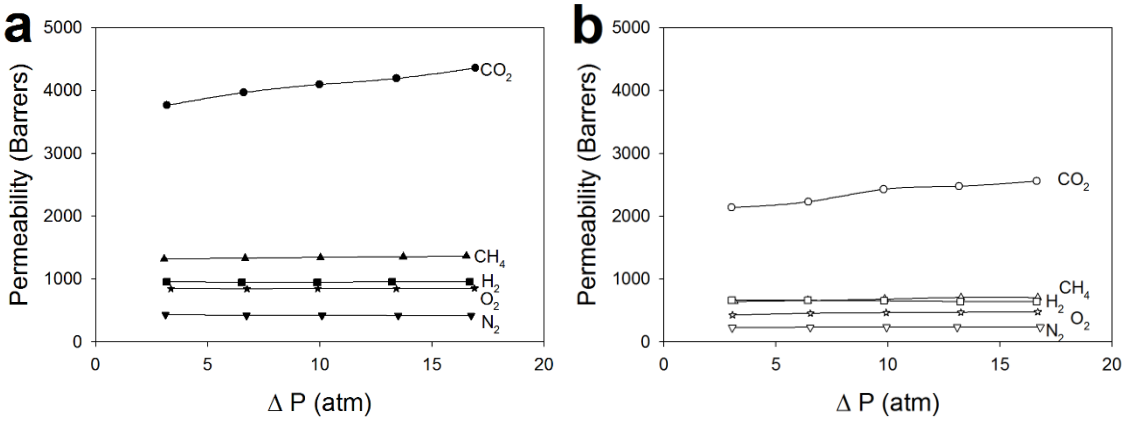

Figure 4.6. Single gas permeability of (a) neat PDMS and (b) telechelic PDMS N1000/1 wt % GO telechelic PDMS/GO elastomers. c

PDMS (and closely related derivatives) are common materials used in commercial gas/vapor separation membranes [40]. It is well accepted that by incorporating less permeable fillers (in this case GO) into the composite matrix, the gas barrier properties of the material should increase by introducing tortuous pathways through which the gas permeates [39,41–43]. To quantitatively measure the permeation of various gases, a single gas permeation test was performed, as shown in Figure 4.6 and tabulated in Table C.2. As a reference case, neat PDMS elastomer was synthesized and tested (Figure 4.6a), which exhibited identical gas permeability performance to that reported previously by others [40]. For the various gases tested, the gas permeability for both neat PDMS and telechelic PDMS/GO composite elastomer increased in the order of N_2, O_2, H_2, CH_4, and CO_2. Strongly sorbing penetrants, such as CO_2, had the tendency to plasticize the polymer matrix and thereby slightly increase the permeability with increasing pressure. Other low-sorbing gas molecules had less effect on permeability with increases in feed pressure [39]. Reacting 1 wt % GO (0.43 vol %) with telechelic PDMS to form the elastomeric matrix resulted in an average reduction of ~ 45 % in N_2, O_2, CH_4, and CO_2 single gas permeabilities. Osman and coworkers achieved a 30% reduction in O_2 transmission rate at 3 vol % for physically mixed polyurethane/alumino-silicate nanocomposites [44] while others have shown a 30-50 % reduction in single gas permeation for polymer mixed with 1.6-1.8 vol % thermally reduced graphene oxide composites (Table C.3, comparing the gas barrier performance of different composite systems) [45]. Finally, as shown in Table 4.3, the gas selectivity values for the telechelic PDMS/GO composite elastomers were more or less similar to that of the neat PDMS elastomer.

Table 4.3. Gas selectivities of neat PDMS and N1000/1 wt % GO elastomer. Selectivity values are calculated based on 10 atm permeability values. Adapted with permission from reference [37]. Copyright 2015 Elsevier.

Material	CO_2/N_2	CO_2/CH_4	O_2/N_2
Neat PDMS	10	3	2
N1000/1 wt % GO	10	4	2

One could speculate that the thermal properties of the neat PDMS and telechelic PDMS/GO elastomer could contribute to differences in their gas permeability data, especially given that the reaction between PDMS and GO might be anticipated to increase the glass transition temperature; Figure C.3 shows that the glass transition temperature (T_g) and melting temperature (T_m) of both materials were essentially identical. This clearly indicates that the significant decrease in gas permeability upon the addition of GO is mostly due to the impermeable dispersed GO component, which constrains gas molecules forcing them to migrate through irregular amorphous regions of the composite material, and not by the reduction in chain segment mobility in the interstitial amorphous phase. It is evident that incorporation of higher loadings of GO (under the constraint that higher levels of this reactive GO component still allows for formation of mechanically robust elastomers) and enhanced alignment of the dispersed GO platelets would provide better gas barrier performance. Research related to these aspects, accompanied with efforts to model the relevant processes, is investigated in the following chapter.

4.5. CONCLUSIONS

A facile method to prepare elastic polymer/GO composite materials using telechelic polymers was developed. By taking advantage of simple chemistry between

amine terminated telechelic polymers and GO, it was possible to transform liquid-like precursor materials into solid, robust elastomers by incorporating less than 1 vol % GO into the system. The GO acted both as a filler material that significantly reinforced the mechanical properties and as a multifunctional crosslinker forming chemical bonds with the polymer establishing the final macromolecular network. The elastomers prepared in this work were highly crosslinked (> 75 wt % gel) and could be extended up to 300 % when mechanically stretched. The rheological studies revealed that the elastomer is stable to external stress over a wide range of strain, frequency, and temperature. The elastomer showed ~45% reduction in various gas permeabilities by incorporating 0.43 vol% of GO, which highlights the use of this material as an effective gas barrier membrane. Furthermore, this simple, potentially cost-effective materials design approach should enable more versatile usage of polymer/GO composite elastomers in many commercial applications, including as gas barrier or separation membranes.

4.6. REFERENCES

[1] Zang J, Ryu S, Pugno N, Wang Q, Tu Q, Buehler MJ, et al. Multifunctionality and control of the crumpling and unfolding of large-area graphene. Nat Mater 2013;12:321–5. doi:10.1038/nmat3542.

[2] Bae S, Lee Y, Sharma BK, Lee H, Kim J, Ahn J. Graphene-based transparent strain sensor. Carbon N Y 2013;51:236–42. doi:10.1016/j.carbon.2012.08.048.

[3] Zeng W, Shu L, Li Q, Chen S, Wang F, Tao X-M. Fiber-Based Wearable Electronics: A Review of Materials, Fabrication, Devices, and Applications. Adv Mater 2014;26:5310–36. doi:10.1002/adma.201400633.

[4] Choi M-C, Kim Y, Ha C-S. Polymers for flexible displays: From material selection to device applications. Prog Polym Sci 2008;33:581–630. doi:10.1016/j.progpolymsci.2007.11.004.

[5] Kim KS, Zhao Y, Jang H, Lee SY, Kim JM, Kim KS, et al. Large-scale pattern growth of graphene films for stretchable transparent electrodes. Nature 2009;457:706–10. doi:10.1038/nature07719.

[6] Choi K, Nam S, Lee Y, Lee M, Jang J, Kim SJ, et al. Reduced Water Vapor Transmission Rate of Graphene Gas Barrier Films for Flexible Organic Field-Effect Transistors. ACS Nano 2015;9:5818–24. doi:10.1021/acsnano.5b01161.
[7] Yang C-C, Hsu Y-L. A Review of Accelerometry-Based Wearable Motion Detectors for Physical Activity Monitoring. Sensors 2010;10:7772–88. doi:10.3390/s100807772.
[8] Yang J, Wei D, Tang L, Song X, Luo W, Chu J, et al. Wearable temperature sensor based on graphene nanowalls. RSC Adv 2015;5:25609–15. doi:10.1039/C5RA00871A.
[9] Wang Y, Wang L, Yang T, Li X, Zang X, Zhu M, et al. Wearable and Highly Sensitive Graphene Strain Sensors for Human Motion Monitoring. Adv Funct Mater 2014;24:4666–70. doi:10.1002/adfm.201400379.
[10] Paul DR, Mark JE. Fillers for polysiloxane ("silicone") elastomers. Prog Polym Sci 2010;35:893–901. doi:10.1016/j.progpolymsci.2010.03.004.
[11] LeVier RR, Lane TH, Harrison MC, Cook RR. What is silicone? J Clin Epidemiol 1995;48:513–7. doi:10.1016/0895-4356(94)00207-7.
[12] Efimenko K, Wallace WE, Genzer J. Surface Modification of Sylgard-184 Poly(dimethyl siloxane) Networks by Ultraviolet and Ultraviolet/Ozone Treatment. J Colloid Interface Sci 2002;254:306–15. doi:10.1006/jcis.2002.8594.
[13] Silicone Rubber Chemical Crosslinking Principle n.d. http://www.wacker.com/cms/en/products/product_groups/silicone_rubbers_1/vernetzung_1.jsp.
[14] Lamberti A, Di Donato M, Chiappone A, Giorgis F, Canavese G. Tunable electromechanical actuation in silicone dielectric film. Smart Mater Struct 2014;23:105001. doi:10.1088/0964-1726/23/10/105001.
[15] Camenzind A, Schweizer T, Sztucki M, Pratsinis SE. Structure & strength of silica-PDMS nanocomposites. Polymer (Guildf) 2010;51:1796–804. doi:10.1016/j.polymer.2010.02.030.
[16] Burnside SD, Giannelis EP. Synthesis and properties of new poly(dimethylsiloxane) nanocomposites. Chem Mater 1995;7:1597–600. doi:10.1021/cm00057a001.
[17] Ma P-C, Siddiqui NA, Marom G, Kim J-K. Dispersion and functionalization of carbon nanotubes for polymer-based nanocomposites: A review. Compos Part A Appl Sci Manuf 2010;41:1345–67. doi:10.1016/j.compositesa.2010.07.003.
[18] Wang Z, Nelson JK, Hillborg H, Zhao S, Schadler LS. Graphene oxide filled nanocomposite with novel electrical and dielectric properties. Adv Mater 2012;24:3134–7. doi:10.1002/adma.201200827.
[19] Du P, Lin X, Zhang X. Tunable electrical and mechanical responses of PDMS and polypyrrole nanowire composites. J Phys D Appl Phys 2013;46:195303. doi:10.1088/0022-3727/46/19/195303.
[20] Yoo BM, Shin HJ, Yoon HW, Park HB. Graphene and graphene oxide and their uses in barrier polymers. J Appl Polym Sci 2014;131:39628. doi:10.1002/app.39628.

[21] Huang H, Ying Y, Peng X. Graphene oxide nanosheet: an emerging star material for novel separation membranes. J Mater Chem A 2014;2:13772. doi:10.1039/C4TA02359E.
[22] Gomez De Arco L, Zhang Y, Schlenker CW, Ryu K, Thompson ME, Zhou C. Continuous, highly flexible, and transparent graphene films by chemical vapor deposition for organic photovoltaics. ACS Nano 2010;4:2865–73. doi:10.1021/nn901587x.
[23] Ha H, Shanmuganathan K, Ellison CJ. Mechanically Stable Thermally Crosslinked Poly(acrylic acid)/Reduced Graphene Oxide Aerogels. ACS Appl Mater Interfaces 2015;7:6220–9. doi:10.1021/acsami.5b00407.
[24] Bay Carbon Inc., SP-1 Graphite Powder n.d. http://www.baycarbon.com/SP1Summary.htm.
[25] Kang D-W, Shin H-S. Control of size and physical properties of graphene oxide by changing the oxidation temperature. Carbon Lett 2012;13:39–43. doi:10.5714/CL.2012.13.1.039.
[26] Dreyer DR, Park S, Bielawski CW, Ruoff RS. The chemistry of graphene oxide. Chem Soc Rev 2010;39:228–40. doi:10.1039/b920539j.
[27] Bourlinos AB, Gournis D, Petridis D, Szabó T, Szeri A, Dékány I. Graphite Oxide: Chemical Reduction to Graphite and Surface Modification with Primary Aliphatic Amines and Amino Acids. Langmuir 2003;19:6050–5. doi:10.1021/la026525h.
[28] Kovtyukhova NI, Ollivier PJ, Martin BR, Mallouk TE, Chizhik SA, Buzaneva E V, et al. Layer-by-Layer Assembly of Ultrathin Composite Films from Micron-Sized Graphite Oxide Sheets and Polycations. Chem Mater 1999;11:771–8. doi:10.1021/cm981085u.
[29] Prime RB, Sacher E. Kinetics of epoxy cure: 2. The system bisphenol-A diglycidyl ether/polyamide. Polymer (Guildf) 1972;13:455–8. doi:10.1016/0032-3861(72)90113-9.
[30] Chiou K-C, Chang F-C. Reactive compatibilization of polyamide-6 (PA 6)/polybutylene terephthalate (PBT) blends by a multifunctional epoxy resin. J Polym Sci Part B Polym Phys 2000;38:23–33. doi:10.1002/(SICI)1099-0488(20000101)38:1<23::AID-POLB3>3.0.CO;2-Y.
[31] Ryu SH, Sin JH, Shanmugharaj AM. Study on the effect of hexamethylene diamine functionalized graphene oxide on the curing kinetics of epoxy nanocomposites. Eur Polym J 2014;52:88–97. doi:10.1016/j.eurpolymj.2013.12.014.
[32] Hung W, Tsou C, De Guzman M, An Q, Liu Y, Zhang Y, et al. Cross-Linking with Diamine Monomers To Prepare Composite Graphene Oxide-Framework Membranes with Varying d -Spacing. Chem Mater 2014;26:2983–90. doi:10.1021/cm5007873.
[33] Cholake S, Mada M, Raman R, Bai Y, Zhao X, Rizkalla S, et al. Quantitative Analysis of Curing Mechanisms of Epoxy Resin by Mid- and Near- Fourier Transform Infra Red Spectroscopy. Def Sci J 2014;64:314–21. doi:10.14429/dsj.64.7326.

[34] Park S, Dikin D a., Nguyen ST, Ruoff RS. Graphene oxide sheets chemically cross-linked by polyallylamine. J Phys Chem C 2009;113:15801–4. doi:10.1021/jp907613s.
[35] Liu H, Kuila T, Kim NH, Ku B-C, Lee JH. In situ synthesis of the reduced graphene oxide–polyethyleneimine composite and its gas barrier properties. J Mater Chem A 2013;1:3739. doi:10.1039/c3ta01228j.
[36] Ha H, Shanmuganathan K, Fei Y, Ellison CJ. Thermal stimuli-responsive behavior of pyrene end-functionalized PDMS through tunable Π-Π interactions. J Polym Sci Part B Polym Phys 2016;54:159–68. doi:10.1002/polb.23805.
[37] Ha H, Park J, Ha K, Freeman BD, Ellison CJ. Synthesis and gas permeability of highly elastic poly(dimethylsiloxane)/graphene oxide composite elastomers using telechelic polymers. Polymer (Guildf) 2016;93:53–60. doi:10.1016/j.polymer.2016.04.016.
[38] Clarizia G, Algieri C, Drioli E. Filler-polymer combination: a route to modify gas transport properties of a polymeric membrane. Polymer (Guildf) 2004;45:5671–81. doi:10.1016/j.polymer.2004.06.001.
[39] Nawaz K, Khan U, Ul-Haq N, May P, O'Neill A, Coleman JN. Observation of mechanical percolation in functionalized graphene oxide/elastomer composites. Carbon N Y 2012;50:4489–94. doi:10.1016/j.carbon.2012.05.029.
[40] Merkel TC, Bondar VI, Nagai K, Freeman BD, Pinnau I. Gas sorption, diffusion, and permeation in poly(dimethylsiloxane). J Polym Sci Part B Polym Phys 2000;38:415–34. doi:10.1002/(SICI)1099-0488(20000201)38:3<415::AID-POLB8>3.0.CO;2-Z.
[41] Cussler EL, Hughes SE, Ward WJ, Aris R. Barrier membranes. J Memb Sci 1988;38:161–74. doi:10.1016/S0376-7388(00)80877-7.
[42] Lape NK, Nuxoll EE, Cussler EL. Polydisperse flakes in barrier films. J Memb Sci 2004;236:29–37. doi:10.1016/j.memsci.2003.12.026.
[43] Choudalakis G, Gotsis AD. Permeability of polymer/clay nanocomposites: A review. Eur Polym J 2009;45:967–84. doi:10.1016/j.eurpolymj.2009.01.027.
[44] Osman M a., Mittal V, Morbidelli M, Suter UW. Polyurethane adhesive nanocomposites as gas permeation barrier. Macromolecules 2003;36:9851–8. doi:10.1021/ma035077x.
[45] Kim H, Abdala A a., Macosko CW. Graphene/polymer nanocomposites. Macromolecules 2010;43:6515–30. doi:10.1021/ma100572e.

Chapter 5: Gas Permeation and Selectivity of Poly(dimethyl siloxane)/ Graphene Oxide Composite Elastomer Membranes[4]

5.1. Overview

While chemically crosslinked PDMS/GO composites were successfully synthesized in chapter 4, in order to develop broad fundamental understanding of the connection between composite architecture and gas transport properties, further studies on both gas barrier and separation characteristics were initiated.

In this study, the permeability for several common gases was examined as a function of GO concentration. Incorporating only 3.55 vol % (8 wt %) GO into the PDMS matrix resulted in a more than 99.9% reduction in gas permeation for various gases, such as H_2, O_2, N_2, CH_4 and CO_2. Moreover, factor of two enhancements in gas selectivities were observed for CO_2/N_2 and CO_2/CH_4 compared to neat PDMS membranes. As a supplement to experimental data from scanning-electron and atomic-force microscopy and x-ray diffraction, theoretical models such as the Nielsen and Cussler models were applied to comprehend the dispersion and alignment of GO in the polymer.

5.2. Introduction

Polymer-based membranes have been studied for more than two centuries, starting in 1748, when Abbé Jean Antoine Nollet reported the permeability of spirits of wine through a pig bladder [1]. More recently, polymer membranes have been considered

[4] Ha H (Designed and performed most of the experiments, wrote and edited the paper), Park J, Ando S, Kim CB, Nagai K, Freeman BD, Ellison CJ. Gas permeation and selectivity of poly (dimethylsiloxane)/graphene oxide composite elastomer membranes. J Memb Sci 2016;518:131-140. doi:10.1016/j.memsci.2016.06.028.

ideal materials for large-scale industrial processes [2,3] and they are currently being used for air separation to produce N_2-enriched air, natural gas treatment to remove acid gas, H_2 separation from hydrocarbons, and many other applications. Some advantages of polymer-based membranes over conventional alternatives include their low cost, ability to be mass produced, low energy consumption, and small footprint required for separation membrane modulus.

However, polymer-based membranes still require additional improvements in gas separation performance, which is typically linked to the so-called permeability-selectivity trade-off. For any given material or class of materials, if permeability increases by some mechanism (e.g., by varying composition, cross-link density, crystallinity, etc.), selectivity typically decreases, and vice versa. In addition, polymers are generally vulnerable to high temperature and harsh chemical environments. Therefore, understanding and enhancing mechanical and chemical stability of polymer-based membranes in industrial environments is crucial. One way to address some of these issues is to incorporate filler materials that can enhance the thermo-physical properties of the membrane as well as tune the gas transport properties. Among the many fillers of interest to scientists in recent years, graphene and related graphene derivatives have been emerging for use in polymer membrane applications [4–6]. Graphene has been a common target due to its intrinsic strength and impermeability to gases, such that transport can only occur through major defects or in-between GO sheets.

As shown in Chapter 4, our group developed a simple method to synthesize highly elastic telechelic PDMS/GO elastomers using affordable amine-terminated telechelic PDMS and graphite [7]. The formation of ethanolamine covalent bonds was proposed based on the heating-induced reaction of primary amine end groups on the polymer with the highly reactive epoxy groups on the surface of GO. This simple

reaction enhanced the mechanical properties of the composite material, forming an elastomeric network with homogeneous GO dispersion from a liquid polymer-GO precursor. Incorporation of 1 wt % GO (0.43 vol %) resulted in a reduction in gas permeability by ~45%, thereby highlighting the material's potential use as a gas barrier membrane. Intuitively, one might expect that higher concentrations of GO could elicit additional reductions in gas permeability and potentially increase gas selectivities for specific gas mixtures.

To the best of our knowledge, systematic studies of the permeation of various gases and the gas barrier and separation performance of polymer/GO composites are still lacking. Therefore, the goal of this study was to investigate the permeability and selectivity of a variety of common gases and gas mixtures composed of H_2, O_2, N_2, CH_4 and CO_2 as a function of GO concentration. Through analysis of experimental gas transport data with different theoretical models, we rationalize the intrinsic behavior of the composite membranes and use this knowledge, in conjunction with microscopy images and x-ray diffraction, to develop understanding regarding the dispersion and alignment of GO platelets. Particularly for gas separation membranes, a number of issues may limit the use of a polymer composite membrane. Typically, the concentration of a gas of interest in flue gas is low, which means large quantities and/or high pressures of the flue gas need to be processed. The high temperature and potential presence of corrosive chemicals of the flue gas may also be a challenge in that it can degrade the polymer membrane over time. Considering the expected thermal and chemical tolerance of the PDMS/GO composite membrane detailed in this work suggests these membranes could be useful in applications such as post-combustion CO_2 capture, CO_2 removal from natural gas and in other industries that use or process CO_2.

5.3. EXPERIMENTAL SECTION

5.3.1. Materials

Three components were used to synthesize PDMS/GO elastomers: telechelic PDMS as the base material, GO as both a filler and multifunctional crosslinker, and tetrahydrofuran (THF; Fisher Chemical) as a solvent. All three components were purchased from the same company and prepared as described in chapter 4. The density of PDMS was assumed to be 0.965 g/cm^3, and the density of graphite was assumed to be 2.28 g/cm^3 as calculated from unit cell dimension data of perfectly crystalline graphite (hexagonal structure, a = 2.46 Å and c = 6.69 Å) [8]. Volume % (henceforth, vol %) was calculated based on the ratio of GO volume to the total volume of the composite material multiplied by 100 using the aforementioned density values.

5.3.2. Fabrication of PDMS/GO Elastomers

Highly elastic telechelic PDMS/GO elastomers were synthesized as described in chapter 4 [7]. Neat PDMS elastomer was also synthesized as a reference material and the detailed synthesis procedure is described in Appendix C [7]. Except for 8 wt % (3.55 vol %) GO elastomers, all other PDMS/GO samples used 1 g of material (PDMS and GO) which was dissolved in 6 ml of THF before sonication. However, due to the high viscosity of the 8 wt % GO composite solution after sonication, 10 ml of THF was used for this sample, while the net weight of solid material was kept the same as the other samples.

5.3.3. Single Gas Permeation Measurements

Single gas, including H_2, O_2, N_2, CH_4 and CO_2, transport properties were measured using the method described in chapter 4. The average thickness of the sample was measured using a dial gauge (Mitutoyo, Absolute digimatic indicator) by

sandwiching a sample between two thin metal plates (each metal plate thickness = 0.05 mm). Metal plates were used to prevent samples from being compressed by the tip of the dial gauge during measurement. Average and standard deviation were calculated based on 30 or more measurements of each sample, and values are tabulated in Appendix D (Table D.1). These values were compared with SEM images for selected samples (Figure D.1), and it was confirmed that the dial gauge measured values were all in good agreement. In summary, the thickness of the neat PDMS elastomer was 0.998 ± 0.021 mm, PDMS/1-5 wt % GO composites were in the range of 0.250-0.381 mm and the PDMS/8 wt % GO composite was 0.081 ± 0.007 mm, respectively. The ideal selectivity, $\alpha_{A/B}$, for gas A (more permeable) and B (less permeable) was calculated as the ratio of pure gas permeabilities of two different gases using $\alpha_{A/B} \equiv P_A/P_B$. The experimental uncertainty for permeability measurements was typically 10 % or better which was confirmed by testing multiple samples for several GO concentrations.

5.3.4. Characterization of PDMS/GO Elastomers

The chemical cross-linking reaction of primary amine ends and epoxies on the surface of GO was investigated using attenuated total reflection Fourier transform infrared spectroscopy (ATR-FTIR; Thermo Nicolett 6700). Scanning electron microscopy (SEM; Zeiss Supra 40 V) was used to study the morphology of the composite material and 12 nm of Pt/Pd were sputter coated on the sample before taking measurements. Due to the low Tg of the PDMS/GO composites, it was a non-trivial task to microtome or cryo-fracture the sample to observe the cross-section of the material. Instead, the cross-section of each sample was exposed by hand tearing to obtain a relatively undamaged cross-sectional surface for SEM imaging. Atomic force microscopy (AFM) images were taken using MFP-3D Origin AFM (Asylum Research; Oxford

Instruments) in order to determine the individual GO size and thickness. Imaging was done in tapping mode using a non-coated Si probe (frequency 300 kHz, spring constant of 26 N/m, and nominal tip radius of 9 ± 2 nm; Olympus). GO samples were prepared for AFM by depositing dispersions of GO in THF on a Si wafer and allowing them to dry in air. Transmission electron microscopy (TEM; FEI Tecnai Spirit Bio Twin TEM) images were acquired by preparing a sample of dilute aqueous dispersion of GO deposited onto a 300 mesh copper Lacey carbon grid. Thermal properties of the PDMS/GO composites were characterized by differential scanning calorimetry (DSC; Mettler Toledo DSC1). Heating and cooling rates of 10 °C/min in N_2 atmosphere were used for all experiments. GO and PDMS/GO elastomers used in this study were further characterized using X-ray diffraction (XRD; Rigaku R-axis Spider) with a CuKα radiation source (λ = 1.5418 Å, the average of Kα1 and Kα2 lines) to determine the presence of large GO agglomerates inside the composite material.

5.4. Results and Discussion

5.4.1. Single Gas Permeability and Gas Barrier Properties

PDMS elastomers are flexible, rubbery materials that are commonly used in commercial vapor separation membranes [9]. Such materials are categorized as weakly size-sieving due to the presence of high free volume and high mobility of the flexible PDMS chains [10]. However, it is well accepted that incorporating less permeable fillers (such as the GO in the present study) into the polymer matrix can significantly increase the gas barrier performance by introducing tortuous pathways through which the gas permeates [11–15]. To quantitatively measure the permeation of various gases, single gas permeation tests were performed, and the results are shown in Figure 5.1. Neat PDMS

elastomer was tested as a reference material and was found to exhibit identical gas permeability performance to that reported previously by others [9]. In general, the gas permeability declined by more than three orders of magnitude upon increasing the concentration of impermeable GO incorporated into the polymer matrix. Strongly sorbing penetrants, such as CO_2 (Figure 5.1e), had a tendency to plasticize the polymer matrix, so the permeability increased slightly with increasing pressure. The permeability of other low-sorbing gas molecules (Figure 5.1a-d) were less affected by increasing feed pressure. Minimal changes in the CO_2 hysteresis loop shown in Figure 5.1f illustrates that all of the materials tested in this study behaved as rubbery materials [2], which is in good agreement with DSC results (DSC thermograms of every sample are shown in Figure D.2).

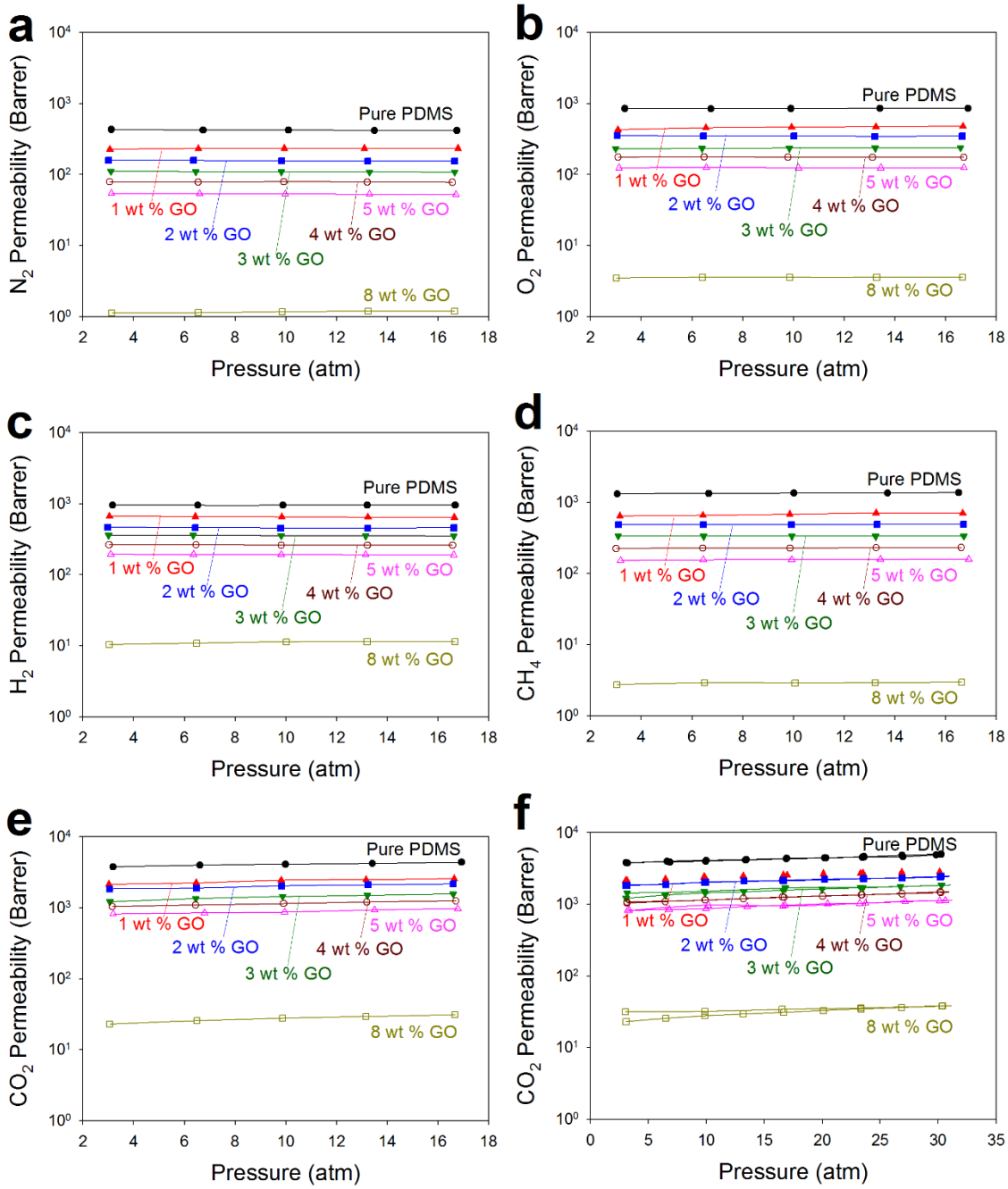

Figure 5.1. Single gas permeability of neat PDMS and PDMS/GO composite elastomers. (a) N_2, (b) O_2, (c) H_2, (d) CH_4, (e) CO_2 permeability, and (f) CO_2 hysteresis permeability results where feed pressure was increased and then decreased. 1, 2, 3, 4, 5, and 8 wt % correspond to 0.43, 0.86, 1.29, 1.73, 2.18, and 3.55 vol %, respectively.

Generally, in rubbery polymers such as PDMS, the permeability strongly depends on the relative solubility of a specific gas molecule, i.e., the solubility selectivity is often higher than diffusivity selectivity. Therefore, PDMS is more permeable to large, soluble and condensable gases than to smaller, less condensable gases. However, as the GO content increased, it is assumed that the diffusivity is more strongly affected than the solubility due to the introduction of more tortuous pathways. The gas permeabilities for neat PDMS and 1-2 wt % PDMS/GO composite elastomers increased in the order of N_2, O_2, H_2, CH_4, and CO_2, which is in agreement with previously reported results [7,9]. However, as the concentration of GO in the composite material was further increased, the order changed to N_2, O_2, CH_4, H_2, and CO_2 for 3-5 wt % PDMS/GO composite elastomers and for 8 wt % PDMS/GO composite elastomers the order changed to N_2, CH_4, O_2, H_2, and CO_2. The more significant decrease in the CH_4 gas permeability is attributed to the smaller channels for gas transport as the concentration of GO increased. The kinetic diameter of CH4 is approximately 3.8 Å, the largest of the gases tested in this study, which suggests the possibility that the gas transport pathways are small enough to size-sieve large penetrants (table of critical temperatures, kinetic diameters, and critical volumes of single gases are shown in Table D.2 and corresponding permeabilities for selected samples in Figure D.3). This is directly reflected in the dramatic decline of the relative permeability coefficient (R), defined as the ratio of the composite permeability to the neat polymer permeability (see Table 5.1). Of course, such an interpretation must be treated with caution given that this study is restricted to small gas molecules, such as H_2, N_2, O_2, CO_2, and CH_4, where the gas kinetic diameter provides a good measure of the penetrant size as it relates to transport properties.

Table 5.1. Relative single gas permeability data for polymer/GO composites from selected literature. *R* is a ratio of the composite permeability to the neat polymer permeability.

Polymer	Filler Type	Loading (vol %)	Operation conditions	Methods	RH_2	RO_2	RN_2	RCH_4	RCO_2	RH_2O	Ref.
PEN	TRG	2.4	35 °C 1 atm	Melt mix	0.45	-	-	-	-	-	[8]
PC	G	6.7	35 °C	Melt mix	-	-	0.64	-	-	-	[16]
PC	TRG	1.6	1 atm	Melt mix	-	-	0.56	-	-	-	[16]
PP	GNP	3.0	25 °C 1 atm	Melt mix	-	0.80	-	-	-	-	[17]
PS	fGO	0.93* (2 wt %)	N/A	In situ	-	0.75	0.41	-	-	-	[18]
TPU	fGO	1.6	35 °C 1 atm	In situ	-	-	0.40	-	-	-	[19]
TPU	iGO	1.6	35 °C 1 atm	Solution	-	-	0.10	-	-	-	[19]
PS	iGO	2.27	23 °C 1 atm	Solution	-	0.39	-	-	-	-	[20]
PVA	GO	0.72	25 °C 1 atm	Solution	-	0.01	-	-	-	0.32	[21]
PLA	GO	1.37	25 °C 1 atm	Solution	-	0.55	-	-	0.32	-	[22]
PI	rGO	21.1* (30 wt %)	25 °C 1 atm	Solution	-	0.07	-	-	-	-	[23]
Matrimid	GO	5.52* (10 wt %)	30 °C 1.97 atm	Solution	-	-	0.37	0.35	0.73	-	[24]
Telechelic PDMS	GO	1.29 3.55	35 °C 10 atm	Solution	0.37 0.01	0.28 0.01	0.26 0.01	0.25 0.01	0.35 0.01	-	This Work

PEN: poly(ethylene-2,6-naphthalate), PC: polycarbonate, PP: polypropylene, PS: polystyrene, TPU: thermoplastic polyurethane, PVA: poly(vinyl alcohol), PLA: poly(lactic acid), PI: polyimide, Matrimid: thermoplastic polyimide copolymer, PDMS: poly(dimethylsiloxane), TRG: thermally reduced graphene oxide, G: graphite, GNP: graphite nanoplatelets, fGO: functionalized graphene oxides for in situ polymerization, iGO: isocyanate treated graphite oxide, GO: graphene oxide prepared by modified Hummer's method. * volume percent was calculated arbitrarily using the following densities: PS = 1.05 g/cm^3, PI = 1.42 g/cm^3, Matrimid = 1.2 g/cm^3, fGO = rGO = 2.28 g/cm^3.

PDMS/GO elastomers reported herein typically showed a greater reduction in permeability, even with a smaller amount of filler content, when compared to other polymer/graphene derivative systems reported in the literature (Table 5.1). For instance, all of the gases studied in this work showed more than 99.9% reduction in gas permeability by incorporating 3.55 vol % GO. It is postulated that the general processing approach and chemical network formed during the cross-linking reaction between the primary amine ends and epoxy groups on the surface of the GO platelets (corresponding ATR-FTIR data in Figure D.4) promoted the efficient dispersion of impermeable fillers throughout the matrix; homogeneous filler dispersion is one of the most important factors in reducing gas permeabilities [7]. Another possibility for the exceptional barrier properties in the present study could be related to the use of a higher aspect ratio filler, which would be expected to increase the diffusion length and the tortuosity for gas transport. This aspect will be addressed in more detail in the following sections.

Interestingly, it has been shown by others that in-situ polymerization is not as effective as solution mixing for dispersing GO derivatives. Kim and coworkers compared thermoplastic polyurethane (TPU)/GO composite elastomers made by different methods

and confirmed that the samples prepared by solution mixing showed better barrier performance than the in-situ polymerized samples [19]. The specific reason for this observation is yet unclear, but this aspect may be another reason for the remarkable improvement in barrier properties for the present system, which used solution mixing instead of melt mixing or in-situ polymerization. Although PVA/GO composites have exhibited unprecedented results in O_2 barrier properties due to the enhanced interaction between the hydroxyl-containing polymer and GO, the PVA composite gas permeability is greatly influenced by the presence of water vapor [21]. It is postulated that a PDMS/GO composite will show outstanding performance even in high humidity, due to the hydrophobic nature of PDMS. A quantitative analysis of the water vapor permeability is beyond the scope of this study, but it will be reported on in the near future.

5.4.2. Modeling Gas Barrier Properties

Owing to the significant reduction in permeability achieved by incorporating a small amount of GO into the system, an associated goal was to develop further fundamental understanding by systematically analyzing the changes in gas permeability using well-accepted theoretical models. The modified Nielsen and Cussler models are the most widely used and accepted to explain the gas barrier performance for a polymer/filler composite material.

Briefly, the modified Nielsen model has been shown to be most accurate in predicting relative permeability coefficients (R or P_c/P_m) in composites possessing high aspect ratio randomly dispersed fillers at very dilute concentrations. This model strongly depends on the state of the filler alignment, and the general form of this equation can be written as [25]

$$\frac{P_c}{P_m} = \frac{1-\phi_d}{1+\frac{\alpha}{3}\left(S+\frac{1}{2}\right)\phi_d} \quad \text{(Eq. 1)}$$

where α represents the aspect ratio of the filler (e.g., length/thickness for GO) and Φ_d is its volume fraction. P_c and P_m represent the permeability of the composite and neat polymer, respectively. S illustrates the state of filler alignment in the composite material, where $S = 0$ for randomly dispersed fillers (Eq. 2) and $S = 1$ for fillers perfectly aligned perpendicular to the gas flux direction (Eq. 3).

$$\frac{P_c}{P_m} = \frac{1-\phi_d}{1+\frac{\alpha}{6}\phi_d} \quad \text{(Eq. 2)}$$

$$\frac{P_c}{P_m} = \frac{1-\phi_d}{1+\frac{\alpha}{2}\phi_d} \quad \text{(Eq. 3)}$$

In contrast, the original Cussler model assumes that flake-like fillers inside a film are randomly spaced but are perfectly aligned perpendicular to the gas flux [12]. In such an idealization, diffusion will only occur through the slits between the fillers arranged as "bricks", which is why this model has a strong resemblance to a "bricks and mortar" situation. Fillers collapse into discrete layers, which in turn are organized to form slits for the gas to diffuse through. However, in an actual composite membrane, it is reasonable to assume that the flake-like fillers will possess a number of different sizes and arrangements (AFM images of GO in Figure D.5). More recently, the same group modified the original Cussler model by assuming a more general case in which the flake-like fillers are interspersed randomly within the polymer [13]. Their work further showed that a distribution of different flake-like particle sizes actually make better barriers in contrast to the traditional notion that size polydispersity would introduce shorter diffusion

pathways and reduce tortuosity. Lape and coworkers examined a composite having two very different sizes of graphite flakes and also mixtures of several discrete sizes as well. Their experimental results supported by proposed theoretical models demonstrated that polydisperse fillers showed negligible differences with a composite having large monodisperse flakes because the larger sized flakes in the distribution are more important for inhibiting penetrant transport. For the present study, the following modified Cussler expression from Lape and coworkers, applicable for a semi-dilute composite having monodisperse platelets that are well aligned but interspersed randomly within a matrix, was used for modeling:

$$\frac{P_c}{P_m} = \frac{1-\phi_d}{\left(1+\frac{1}{3}\alpha\phi_d\right)^2} \qquad \text{(Eq. 4)}$$

Table 5.2 tabulates key differences between the three models used to analyze data in the present study: the modified Nielsen model for randomly dispersed (Eq. 2) and perfectly aligned fillers (Eq. 3) and the modified Cussler model (Lape et al., Eq. 4). The major difference between the Nielsen and Cussler models is the filler concentration. In a dilute situation, the fillers are spaced at a distance much larger than the filler radius or length. The contribution of impermeable fillers to the reduction in the total composite permeability is small in this case, and therefore it is best described by the "tortuosity model" proposed by Nielsen. However, once the concentration becomes semi-dilute, the interstitial distance between two filler particles is small enough that they overlap, and this effect dominates the diffusion of penetrants. This case is best described by the modified Cussler model [13,26]. It is generally accepted that the composite is in a semi-dilute state when the product of the aspect ratio α and the volume fraction Φ_d of the filler is

significantly larger than 1 ($\alpha\Phi_d >> 1$). More detailed information on the theoretical models investigated in this work is provided in the Appendix D.

Table 5.2. Comparison of the three different models used to analyze data in this study.

Models	Array	Filler Alignment	Concentration	Ref.
Modified Nielsen (Random)	Random	Random	Dilute	[25]
Modified Nielsen (Aligned)	Random	Aligned	Dilute	[25]
Lape et al. (modified Cussler)	Random	Aligned	Semi-dilute	[13]

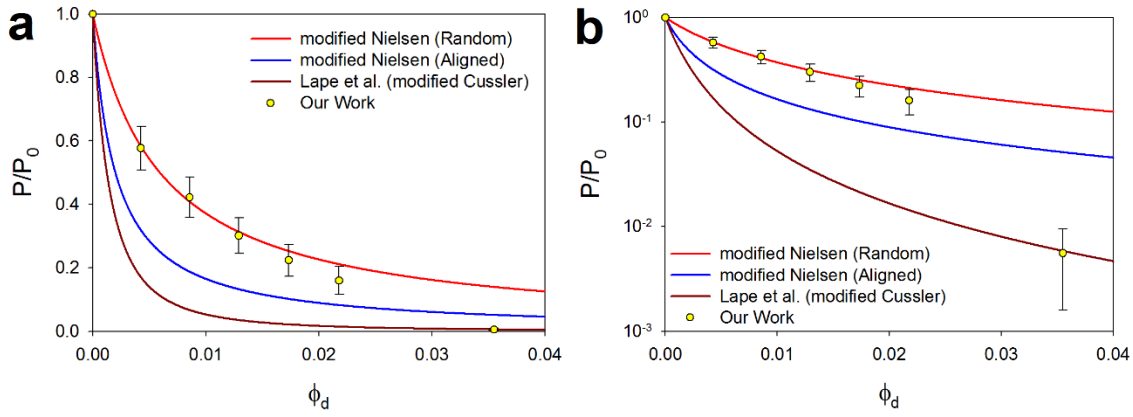

Figure 5.2. Relative permeability as a function of GO volume fraction compared with various theoretical models. (a) is on a linear scale while (b) is the same information expressed in semi-log form. Data points are the average relative permeability coefficient (R) values of all gases (N_2, O_2, H_2, CH_4, and CO_2) while the error bars are standard deviations of these data.

Figure 5.2 depicts the experimental data plotted with various models assuming that the single adjustable parameter (aspect ratio α) is 1,000. Overall, the relative gas permeability decreased exponentially, which is in good agreement with the shape of the models proposed by Nielsen and Cussler. The randomly aligned modified Nielsen model is in excellent agreement for composites possessing a low concentration of GO (1-3 wt %

or Φ_d = 0.0043-0.0129). This illustrates that at low concentrations, the fillers tend to align randomly regardless of gravitational effects during the sample preparation step. However, as the concentration of GO increased (4-5 wt % or Φ_d =0.0173-0.0218), the relative permeability values tend to approach the more aligned situation predicted by the modified Nielsen model for the aligned filler case (blue curve). Platelets such as GO prefer to orient parallel in a nematic fashion as the particle concentration increases [19]. Furthermore, when the concentration is high enough such that $\alpha\Phi_d >> 1$ (for 8 wt % or Φ_d = 0.0355, $\alpha\Phi_d$ = 35), the data fits perfectly with the modified Cussler model. Finally, considering that larger-sized fillers are known to dominate the gas permeability [13], assuming an aspect ratio of 1,000 seems to be a fair assumption based on AFM and TEM image analysis (Figure D.5 and D.6), and this value clearly leads to model predictions that are in good agreement with experimental data.

SEM images of cross-sections shown in Figure 5.3 were taken for selected samples to experimentally characterize rather than infer the alignment of the fillers. All of the samples were cross-sectioned by tearing instead of using cryo-fractured or microtomed samples due to the low T_g (~ -130 ^oC) of the composite material (DSC data in Figure D.2). While it was difficult to locate GO for the low-concentration sample (2 wt % GO, Figure 5.3a), samples with higher loadings of GO revealed that the individual GO sheets are mostly aligned perpendicular to the gas flow direction, and the 8 wt % sample (Figure 5.3c) was nearly completely aligned. Another interesting observation was that the GO sheets are not perfectly flat, but rather have a wrinkled structure (Figure 5.3b-c). This wrinkled structure is crucial for the dispersion of GO, as it could minimize restacking/aggregation. Flat sheets with a high aspect ratio will have a tendency to restack/aggregate because of their high surface area and attractive van der Waals forces between sheets. Wide-angle X-ray diffraction (WAXD) was performed to confirm the

absence of agglomerates due to restacking (Figure D.7), and as expected, only an amorphous halo peak was observed for all of the samples. This result suggests that the stacking of GO is rare, or the sheets are more than 10 Å apart and thus scatter at a lower angle than can be detected with XRD. In summary, at low concentrations, the GO are isotropically dispersed in the polymer matrix and follow the modified Nielsen randomly oriented model. As the concentration further increases, GO sheets tend to align, which is demonstrated as relative permeability converges towards the modified Nielsen model for the aligned filler situation. Finally, when the GO concentration is semi-dilute, the data fits nearly perfectly with the modified Cussler model proposed by Lape and coworkers.

The idea of using three different models depending on the state of alignment and the concentration of GO is illustrated in Figure 5.3d for clarity. Because each model is derived under different assumptions regarding filler alignment and concentration (see Table 5.2), it is logical to use models that are appropriate to specific conditions. Previous studies summarized in Table 5.3 also illustrate that the modified Nielsen model generally shows good agreement in dilute systems, while the modified Cussler model performs better for semi-dilute composites.

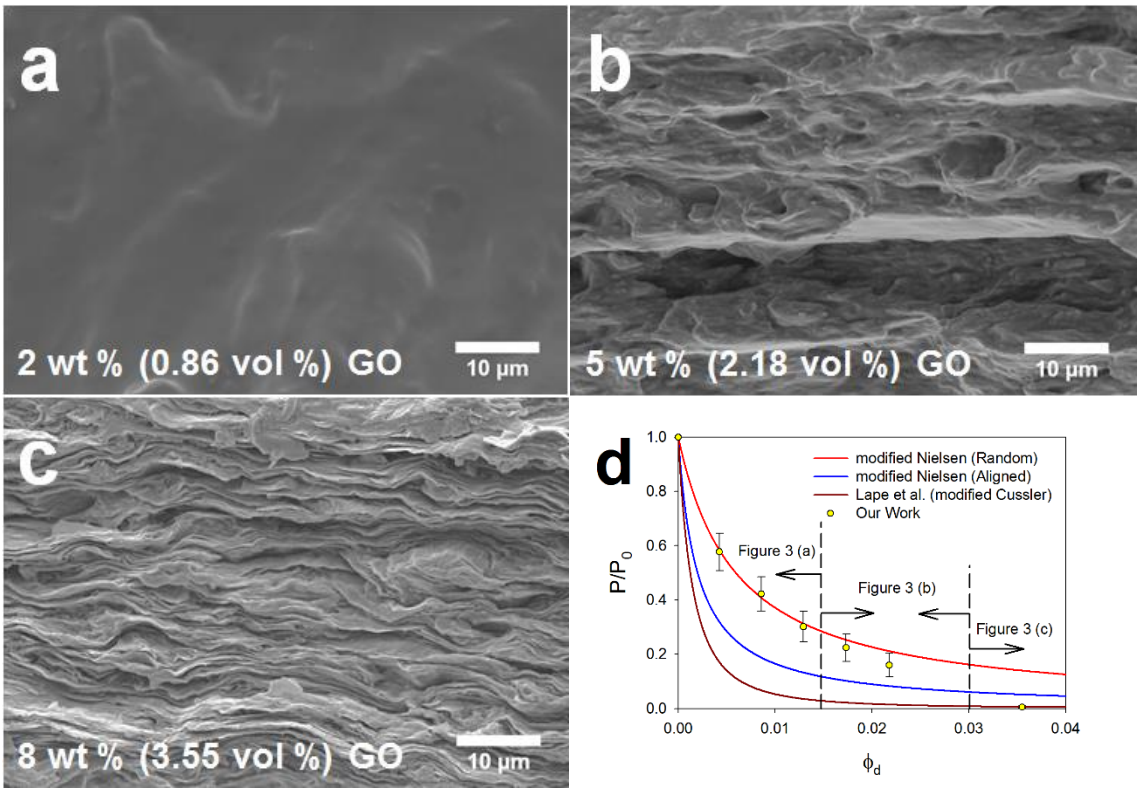

Figure 5.3. Cross-sectional SEM images of selected PDMS/GO composites. (a) 2 wt % (0.86 vol %) GO, (b) 5 wt % (2.18 vol %) GO, and (c) 8 wt % (3.55 vol %) GO composites. (d) Graph representing relative permeability coefficient as a function of GO volume fraction divided into three different regions depending on the state of GO alignment and concentration of GO.

Table 5.3. Attempts of modeling a range of relative permeability data using various models.

Polymer	Filler Type	Loading (vol %)	Model	Gas	Remark	Ref.
PEN	TRG	0.60 – 2.40	Lape et al.	H_2	Good agreement	[8]
PC	TRG	0.13 – 1.60	Lape et al.	He, N_2	Good agreement	[16]
TPU	iGO	0.26 – 1.60	Lape et al.	N_2	Good agreement	[19]
PS	iGO	0.02 – 0.94	m-Nielsen Cussler	O_2	Relatively better agreement with m-Nielsen model	[20]
PVA	GO	0.18 – 0.72	Cussler	O_2	Underestimation at 0.18 vol %	[21]
PLA	GO	0.17 – 1.37	m-Nielsen	O_2, CO_2	Good agreement	[22]
PDMS	TRG	Less than 5 wt%	m-Nielsen	Air	Good agreement	[27]
Telechelic PDMS	GO	0.43 – 3.55	m-Nielsen Lape et al.	Various gases	m-Nielsen at low concentrations Lape et al. at high concentrations	This Work

While Table 5.3 shows that the values predicted by the models are close to the experimental data, errors are expected for several reasons. First, as shown in SEM images, the irregular shape and orientation, dispersion and size distribution of GO platelets are likely different from those described in idealized models. Second, all of the models require a single value of the aspect ratio of the fillers, which is difficult to accurately estimate from a wrinkled structure. Third, all of the models neglect the effect of the polymer matrix and treat all gas molecules as the same. Depending on the nature of

the polymer (e.g., gas permeability, chain mobility, free volume, etc.), the gas transport properties may differ substantially, but these factors are not considered in these idealized models. Furthermore, as shown in the permeability data in Figure 5.1 and Table 5.1, and the modeling results for various individual gases in Figure D.8, different relative permeability coefficients were observed for different gas molecules. Larger gas molecules, such as CH_4 (Table 5.1, for 1.29 vol % (3 wt %) GO R_{CH4} = 0.25), showed larger decreases in gas permeability compared to smaller molecules, such as H_2 (Table 5.1, for 1.29 vol % (3 wt %) GO R_{H2} = 0.37). However, according to the idealized models all gas molecules should exhibit an identical permeability reduction if the volume fraction and the aspect ratio are the same; in aggregate, these results suggest PDMS/GO membranes may exhibit gas separation characteristics and this is the topic of the next section.

5.4.3. Gas Selectivity

While the gas barrier properties of PDMS/GO elastomers showed interesting behavior, gas selectivity studies provide additional understanding of the material performance as a gas separation membrane. The inherently different behavior of composite membranes with different GO concentrations becomes more obvious when comparing the gas selectivities. Figure 5.4 shows a combination of gas permeabilities and ideal selectivities for selected PDMS/GO composite elastomers compared to those of the neat PDMS elastomer. Interestingly, significant increases in the ideal selectivities were observed for CO_2/N_2, CO_2/CH_4, and O_2/N_2. Because N_2 and CH_4 were the largest penetrants considered, it is postulated that the increase in the ideal selectivity is due to the size and shape differences between two penetrants (refer to the kinetic diameter of gases in Table D.2), and such large penetrants are often most sensitive to changes in a polymer

system that alters the availability of transport pathways through the material. Impenetrable fillers having a high aspect ratio increase the length of the tortuous path for gas to diffuse through the polymer matrix; as the constrictions in the tortuous path become smaller, the diffusion of larger molecules is reduced more than that of smaller molecules. The kinetic diameters of N_2 and CH_4 are considerably larger than that of CO_2, and N_2 is larger than O_2. Greater reductions in gas permeation occurred for larger gas molecules (N_2 and CH_4) than for smaller gas molecules (CO_2 and O_2), and as a result, the ideal selectivities were increased substantially. In contrast, the CO_2/H_2 selectivity decreased as GO content was increased, since the kinetic diameter of CO_2 is much greater than that of H_2 (opposite situation from Figure 5.4a-c).

More insight regarding the effect of the kinetic diameter differences and size-sieving effects can be obtained by comparing the relative selectivities (ratio of composite selectivity to neat polymer selectivity). Figure 5.5 compares the relative selectivity increases of various gas mixtures for selected concentrations of GO. CO_2/O_2, CO_2/N_2 and CO_2/CH_4 have kinetic diameter differences of 0.16, 0.34, and 0.50 Å, respectively. It is evident that the relative selectivity increases dramatically as the difference in kinetic diameter increases, suggesting that a size-sieving effect plays an important role in gas separation for PDMS/GO elastomers. The CO_2/N_2 selectivity increases by a factor of approximately 2 for 8 wt % GO (3.55 vol %), while the CO_2/CH_4 selectivity increases by a factor of approximately 3. This strongly suggests that this material could be used in post-combustion carbon capture or industries that require CO_2 separations. It would be of great interest to conduct mixed gas permeability studies of some of these gas pairs involving CO_2, but such studies are beyond the scope this initial, exploratory investigation.

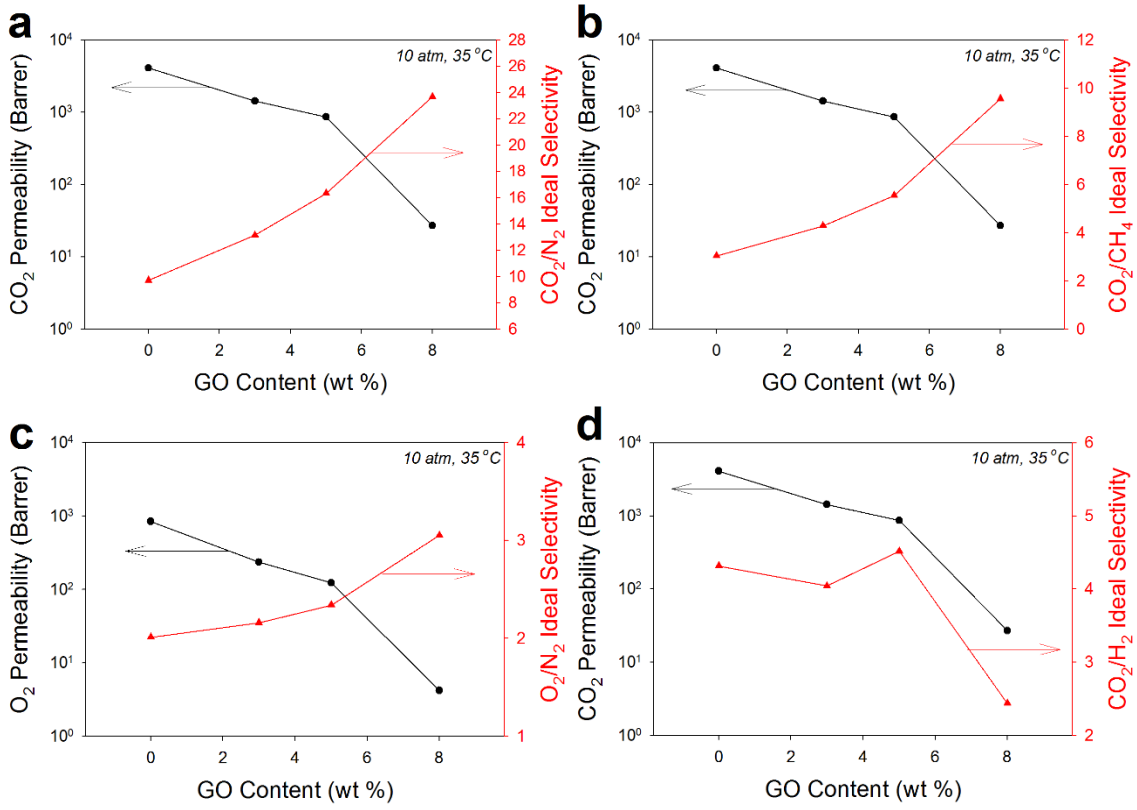

Figure 5.4. Various gas permselectivities as a function of GO content in the PDMS/GO composite membrane. All of the measurements are based on 10 atm, 35 °C. Refer to Figure D.9 for corresponding ideal gas selectivities as a function of pressure. Error bars are not shown in this image since the experimental uncertainty for permeability measurements was typically 10 % or better which was confirmed by testing multiple samples for several GO concentrations.

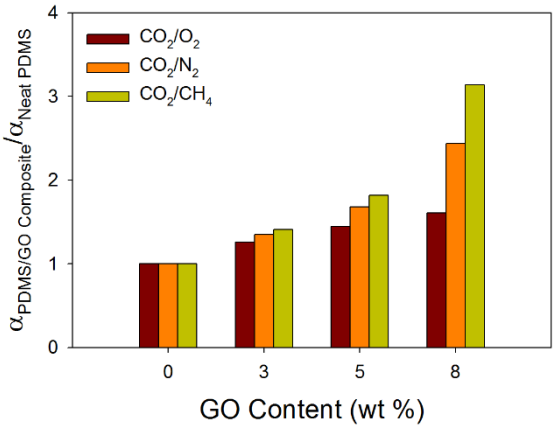

Figure 5.5. Relative ideal selectivity of CO_2 for selected PDMS/GO elastomers. Error bars are not shown in this image since the experimental uncertainty for permeability measurements was typically 10 % or better which was confirmed by testing multiple samples for several GO concentrations.

The CO_2/N_2 case showed one of the most pronounced increases in selectivity as the GO content increased. Figure 5.6 depicts the CO_2/N_2 gas selectivities of various polymers in a Robeson plot [28]. Our data displayed on this plot suggests the behavior is consistent with "tightening" of the diffusion pathways of the polymer by adding more impermeable filler. Such movements nearly parallel to the upper bound are often what are expected if the permeability in a polymer were being systematically decreased by copolymerization or cross-linking. As shown in the barrier properties of PDMS/GO elastomers, increasing the GO content seems to similarly constrict the bottlenecks that govern selectivity.

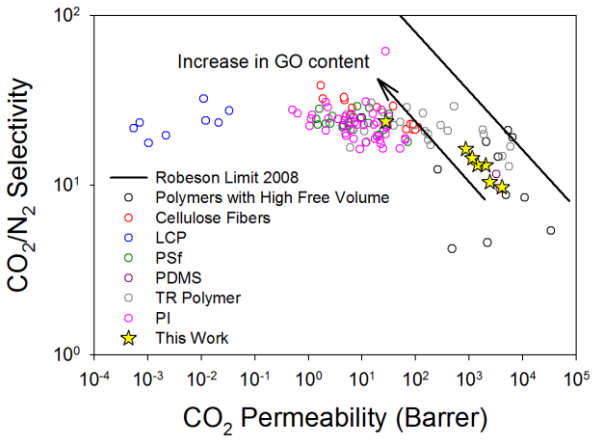

Figure 5.6. CO_2/N_2 gas selectivity comparison based on a Robeson plot from 2008. Various acronyms stand for: liquid crystalline polymer (LCP), polysulfone (PSf), thermally rearranged polymer (TR polymer) and polyimide (PI).

From a practical point of view, a CO_2/N_2 selectivity of 20 is required for commercially relevant post-combustion carbon capture processes based on the assumption of CO_2 gas permeance of 1000 GPU [29]. While the CO_2 gas permeance of the current material is considerably lower than 1000 GPU, higher permeance can be effectively engineered by reducing the thickness of the membrane. The current thickness for the PDMS/8 wt % GO composite membrane reported herein is ~100 μm. Future studies revealing how the permeance changes with respect to the membrane thickness will be beneficial for practical implementation of these materials and it could introduce other avenues for tuning their gas transport properties.

Although the permeability decreases as the concentration of GO content increases, because the base PDMS material is highly permeable, the CO_2 permeability is still considerably higher than that found in other studies using engineering polymers. The gas selectivity of the PDMS/GO elastomer is comparable to that of polysulfone (PSf) and polyimide (PI), as shown in the Robeson plot in Figure 5.6 and Table 5.4. While these

polymers show similar selectivities, the cost of synthesizing the material and the capability of tuning its properties make PDMS/GO elastomers unique and highly attractive. Moreover, the PDMS/GO elastomer in this study is distinguished from other composite systems by the covalent bonding between the polymer and the GO basal plane formed through simple solution casting and annealing, which enables the effective loading of a high amount of dispersed GO into the system. Several groups have reported exceptionally high CO_2 permeabilities and CO_2/N_2 selectivities owing to the intrinsically high gas transport performance of the host/neat polymers, such as polymers containing poly(ethylene oxide) segments [30,31]. These studies generally incorporated only a small amount of GO and, in some cases, even observed a decrease in selectivity when the concentration of GO was increased further [29]. One possible explanation for this behavior could be the formation of large agglomerates when GO is physically mixed inside a viscous polymer matrix. Comparing the selectivity increment of composite materials with respect to the neat polymer, others reported 43% and 82% increases in CO_2/N_2 ideal selectivities with a maximum loading of GO, while we obtained a 143% increase. These aspects highlight the use of the PDMS/GO elastomers as an effective gas separation membrane.

Table 5.4. CO_2 permeability and CO_2/N_2 selectivity data from selected literature. Permeabilities are in Barrer units.

Polymer	Filler Type	Loading (wt %)	Operation Conditions	P_{CO_2}	α_{CO_2/N_2}	Ref.
Neat PEO-PBT	-	-	25 °C, 0.5 bar	150	52	[30]
PEO-PBT	GO	0.0625	25 °C, 0.5 bar	143	73	[30]
Neat Pebax	-	-	25 °C, 3 bar	70	64	[31]
Pebax	GO	0.1	25 °C, 3 bar	100	91	[31]
PSf	Silica	30	25 °C, 2 bar	20.5	27.2	[32]
SPEEK	Silica	30	25 °C, 10 bar	18.5	38*	[33]
Matrimid	CMS	36 vol %	35 °C, 3.5 bar	12.6	33.15	[34]
Matrimid	CSM	30	35 °C, 9 bar	52.6	37.6	[35]
Neat PDMS	-	-	35 °C, $\Delta p = 0$	3800	9.5	[9]
Telechelic PDMS	GO	8	35 °C, 10 bar	27.7	24	This Work

PEO: poly(ethylene oxide), PBT: poly(butylene terephthalate), Pebax: polyether block amide, PSf: polysulfone, SPEEK: poly(ether ether ketone), CMS: carbon molecular sieve, CSM: carbon-silica nanocomposites, * Gas mixture (50:50 vol %); values without '*' are based on single gas measurements.

5.5. CONCLUSIONS

In summary, an investigation of the effect of GO content on gas barrier and separation performance for a highly elastic PDMS/GO elastomer was performed. The material was synthesized in solution using a simple thermally-activated reaction between

the amine terminated telechelic polymer and GO precursors, resulting in good GO dispersion throughout the matrix. In order to broadly and fundamentally understand how this composite architecture impacts gas transport, both gas barrier and separation characteristics were evaluated. As a result, incorporating 3.55 vol % (8 wt %) GO resulted in a 99.9% reduction in gas permeability for several gases, which suggests their potential utility as an effective gas barrier membrane. Furthermore, gas barrier performance was correlated with well-known theoretical models, such as the modified Nielsen and Cussler model, accompanied with cross-sectional SEM images confirming the applicability of such models. Our data suggests that the gas permeability reduction can be divided into three different regimes depending on the filler concentration and degree of alignment relative to the direction of gas transport. Finally, compared to the intrinsically high permeability and low gas selectivity of the PDMS base material, the composite elastomer showed significant increases in certain gas selectivities due to the incorporation of the GO filler. For example, the observed CO_2 gas separation performance of the PDMS/GO elastomer membranes was comparable to membranes based on engineering plastics. We believe this strategy for making composite membranes can be generalized to other polymer precursors which may lead to further tunability of their transport properties and this will be the subject of future research.

5.6. REFERENCES

[1] Nollet JA. Investigations on the causes for the ebullition of liquids. J Memb Sci 1995;100:1–3. doi:10.1016/0376-7388(94)00224-M.

[2] Ghosal K, Freeman BD. Gas separation using polymer membranes: An overview. Polym Adv Technol 1994;5:673–97. doi:10.1002/pat.1994.220051102.

[3] Sanders DF, Smith ZP, Guo R, Robeson LM, McGrath JE, Paul DR, et al. Energy-efficient polymeric gas separation membranes for a sustainable future: A review. Polym (United Kingdom) 2013;54:4729–61. doi:10.1016/j.polymer.2013.05.075.

[4] Potts JR, Dreyer DR, Bielawski CW, Ruoff RS. Graphene-based polymer nanocomposites. Polymer (Guildf) 2011;52:5–25. doi:10.1016/j.polymer.2010.11.042.
[5] Smith ZP, Freeman BD. Graphene oxide: A new platform for high-performance gas- and liquid-separation membranes. Angew Chemie - Int Ed 2014;53:10286–8. doi:10.1002/anie.201404407.
[6] Yoo BM, Shin HJ, Yoon HW, Park HB. Graphene and graphene oxide and their uses in barrier polymers. J Appl Polym Sci 2014;131:39628. doi:10.1002/app.39628.
[7] Ha H, Park J, Ha K, Freeman BD, Ellison CJ. Synthesis and gas permeability of highly elastic poly(dimethylsiloxane)/graphene oxide composite elastomers using telechelic polymers. Polymer (Guildf) 2016;93:53–60. doi:10.1016/j.polymer.2016.04.016.
[8] Kim H, Macosko CW. Morphology and Properties of Polyester/Exfoliated Graphite Nanocomposites. Macromolecules 2008;41:3317–27. doi:10.1021/ma702385h.
[9] Merkel TC, Bondar VI, Nagai K, Freeman BD, Pinnau I. Gas sorption, diffusion, and permeation in poly(dimethylsiloxane). J Polym Sci Part B Polym Phys 2000;38:415–34. doi:10.1002/(SICI)1099-0488(20000201)38:3<415::AID-POLB8>3.0.CO;2-Z.
[10] Freeman BD, Pinnau I. Separation of gases using solubility-selective polymers. Trends Polym Sci 1997;5:167–73.
[11] Paul DR, Robeson LM. Polymer nanotechnology: Nanocomposites. Polymer (Guildf) 2008;49:3187–204. doi:10.1016/j.polymer.2008.04.017.
[12] Cussler EL, Hughes SE, Ward WJ, Aris R. Barrier membranes. J Memb Sci 1988;38:161–74. doi:10.1016/S0376-7388(00)80877-7.
[13] Lape NK, Nuxoll EE, Cussler EL. Polydisperse flakes in barrier films. J Memb Sci 2004;236:29–37. doi:10.1016/j.memsci.2003.12.026.
[14] Choudalakis G, Gotsis AD. Permeability of polymer/clay nanocomposites: A review. Eur Polym J 2009;45:967–84. doi:10.1016/j.eurpolymj.2009.01.027.
[15] Cui Y, Kundalwal SI, Kumar S. Gas barrier performance of graphene/polymer nanocomposites. Carbon N Y 2016;98:313–33. doi:10.1016/j.carbon.2015.11.018.
[16] Kim H, Macosko CW. Processing-property relationships of polycarbonate/graphene composites. Polymer (Guildf) 2009;50:3797–809. doi:10.1016/j.polymer.2009.05.038.
[17] Kalaitzidou K, Fukushima H, Drzal LT. Multifunctional polypropylene composites produced by incorporation of exfoliated graphite nanoplatelets. Carbon N Y 2007;45:1446–52. doi:10.1016/j.carbon.2007.03.029.
[18] Yu Y-H, Lin Y-Y, Lin C-H, Chan C-C, Huang Y-C. High-performance polystyrene/graphene-based nanocomposites with excellent anti-corrosion properties. Polym Chem 2014;5:535–50. doi:10.1039/C3PY00825H.

[19] Kim H, Miura Y, MacOsko CW. Graphene/polyurethane nanocomposites for improved gas barrier and electrical conductivity. Chem Mater 2010;22:3441–50. doi:10.1021/cm100477v.
[20] Compton OC, Kim S, Pierre C, Torkelson JM, Nguyen ST. Crumpled graphene nanosheets as highly effective barrier property enhancers. Adv Mater 2010;22:4759–63. doi:10.1002/adma.201000960.
[21] Huang HD, Ren PG, Chen J, Zhang WQ, Ji X, Li ZM. High barrier graphene oxide nanosheet/poly(vinyl alcohol) nanocomposite films. J Memb Sci 2012;409-410:156–63. doi:10.1016/j.memsci.2012.03.051.
[22] Huang HD, Ren PG, Xu JZ, Xu L, Zhong GJ, Hsiao BS, et al. Improved barrier properties of poly(lactic acid) with randomly dispersed graphene oxide nanosheets. J Memb Sci 2014;464:110–8. doi:10.1016/j.memsci.2014.04.009.
[23] Zhu J, Lim J, Lee CH, Joh HI, Kim HC, Park B, et al. Multifunctional polyimide/graphene oxide composites via in situ polymerization. J Appl Polym Sci 2014;131:1–7. doi:10.1002/app.40177.
[24] Li X, Ma L, Zhang H, Wang S, Jiang Z, Guo R, et al. Synergistic effect of combining carbon nanotubes and graphene oxide in mixed matrix membranes for efficient CO2 separation. J Memb Sci 2015;479:1–10. doi:10.1016/j.memsci.2015.01.014.
[25] Bharadwaj RK. Modeling the barrier properties of polymer-layered silicate nanocomposites. Macromolecules 2001;34:9189–92. doi:10.1021/ma010780b.
[26] Decker JJ, Meyers KP, Paul DR, Schiraldi DA, Hiltner A, Nazarenko S. Polyethylene-based nanocomposites containing organoclay: A new approach to enhance gas barrier via multilayer coextrusion and interdiffusion. Polymer (Guildf) 2015;61:42–54. doi:10.1016/j.polymer.2015.01.061.
[27] Ozbas B, O'Neill CD, Register R a., Aksay I a., Prud'Homme RK, Adamson DH. Multifunctional elastomer nanocomposites with functionalized graphene single sheets. J Polym Sci Part B Polym Phys 2012;50:910–6. doi:10.1002/polb.23080.
[28] Robeson LM. The upper bound revisited. J Memb Sci 2008;320:390–400. doi:10.1016/j.memsci.2008.04.030.
[29] Merkel TC, Lin H, Wei X, Baker R. Power plant post-combustion carbon dioxide capture: An opportunity for membranes. J Memb Sci 2010;359:126–39. doi:10.1016/j.memsci.2009.10.041.
[30] Karunakaran M, Shevate R, Kumar M, Peinemann K-V. CO2 -selective PEO–PBT (PolyActive^{TM})/graphene oxide composite membranes. Chem Commun 2015;51:14187–90. doi:10.1039/C5CC04999G.
[31] Shen J, Liu G, Huang K, Jin W, Lee KR, Xu N. Membranes with fast and selective gas-transport channels of laminar graphene oxide for efficient CO2 capture. Angew Chemie - Int Ed 2015;54:578–82. doi:10.1002/anie.201409563.
[32] Reid BD, Ruiz-Trevino FA, Musselman IH, Balkus KJ, Ferraris JP. Gas Permeability Properties of Polysulfone Membranes Containing the Mesoporous Molecular Sieve MCM-41. Chem Mater 2001;13:2366–73. doi:10.1021/cm000931+.

[33] Khan AL, Klaysom C, Gahlaut A, Khan AU, Vankelecom IFJ. Mixed matrix membranes comprising of Matrimid and -SO3H functionalized mesoporous MCM-41 for gas separation. J Memb Sci 2013;447:73–9. doi:10.1016/j.memsci.2013.07.011.
[34] Vu DQ, Koros WJ, Miller SJ. Mixed matrix membranes using carbon molecular sieves. J Memb Sci 2003;211:311–34. doi:10.1016/S0376-7388(02)00429-5.
[35] Waqas Anjum M, de Clippel F, Didden J, Laeeq Khan A, Couck S, Baron G V., et al. Polyimide mixed matrix membranes for CO2 separations using carbon–silica nanocomposite fillers. J Memb Sci 2015;495:121–9. doi:10.1016/j.memsci.2015.08.006.

Chapter 6: Conclusions and Recommendations

6.1. Conclusions

This dissertation focused on a systematic study of the synthesis, properties, and applications of polymer/GO composites that exploit specific interactions between functional polymers and GO. GO was chosen because of the residual functional groups on the surface of the graphene basal plane, which can participate in both secondary interactions and reactions that form covalent bonds.

By taking advantage of secondary interactions, such as hydrogen bonding and π-π interactions, highly porous thermally crosslinked PAA/rGO aerogels and thermal stimuli-responsive pyrene end-labeled PDMS gels were successfully synthesized. Crosslinked PAA/rGO aerogels had mass densities of about 4-6 mg/cm^3 and > 99.6% porosity that can reversibly support up to 10,000 times their weight with full recovery of their original volume. This material showed capabilities as a pressure sensor and oil absorber due to their high electrical conductivity, reversibility of mechanical deformation, and hydrophobicity. Pyrene end-labeled PDMS exhibited a 7 orders of magnitude change in storage modulus in response to thermal stimuli by modifying only 0.6 wt % of all polymer segments. The properties of these materials were tunable by adding free pyrene, neat PDMS or GO nanoparticles, and also showed potential as a surfactant to disperse GO in common organic solvents.

While utilizing secondary interactions between PDMS and GO could be suitable for some applications, an even greater variety of applications can be realized by forming covalent bonds between polymer and GO. Amine-terminated PDMS was chemically crosslinked by reacting with surface epoxy groups on GO to form a robust elastomer

during simple heating. In these materials, GO acts both as a nanofiller which reinforces the mechanical properties and participates as a multifunctional crosslinker, thereby promoting elastic properties. The final product was highly crosslinked but highly flexible such that it can be stretched up to 300 % of its original length. Incorporating only 3.55 vol % GO into the PDMS matrix resulted in a more than 99.9% reduction in gas permeation for various gases, thereby highlighting its potential use as a gas barrier membrane. Moreover, factor of two enhancements in gas selectivities were observed for CO_2/N_2 and CO_2/CH_4 compared to neat PDMS membranes. This suggests these membranes could be useful in applications such as post-combustion CO_2 capture, CO_2 removal from natural gas and in other industries that use or process CO_2.

6.2. Recommendations For Future Work

6.2.1. Polymer/rGO Aerogel for Li-ion Battery

In this work, XPAA/rGO aerogels showed promising results as a pressure sensor and oil absorber. However, considering the high electrical conductivity, porosity and flexibility, this material could also be used as a current collector for Li-ion batteries. The typical thickness of a commercial Li-ion battery electrode film is limited in order to avoid film delamination and increases in resistance. These factors which limit film thickness for conventional slurry casted metal foils restrict achievable energy density per unit area when using commercially available active materials. It is postulated that this problem can be solved by organizing active materials into a thick film supported not by a metal foil, but instead by a highly porous, conductive, compressible, flexible and inexpensively made three-dimensional current collector such as the polymer/rGO aerogel. Further research to validate this concept, including examining the battery performance using

polymer/rGO aerogels as a 3-dimensional cathode electrode will be a promising area of research in the future.

6.2.2. UV Light Stimuli-responsive Telechelic Polymers

At the moment, the understanding of tunability in elastic properties of pyrene end-labeled PDMS gels upon heating is due to the association//disassociation of π-π interactions between pyrene ends. One can speculate that not only heat, but UV light may also modulate the elastic properties of the pyrene end-labeled polymer. The energy associated with the π-π interaction between pyrene molecules has been reported to be ~ 40 kJ/mol. As long as the UV light source can provide enough energy, the material properties could be modulated locally. This kind of approach may be useful for repositioning adhesives or in electronics, where spatially control over the properties of a material is important. Further studies on the UV light stimuli-responsiveness accompanied by precise in-situ rheological measurements should be able to validate this concept.

6.2.3. Chemically Crosslinked Semi-crystalline Polymer/GO Composites

In this thesis, amine terminated telechelic PDMS was used as a starting material because it has been well-studied during the past few decades and the gas permeability is high enough to clearly distinguish the reduction in gas permeability due to the presence of GO. However, for polymer-based barrier films, semi-crystalline polymers are considered to be more suitable for commercialization. Although incorporating GO in a different polymer seems simple and straight-forward, there are many issues to consider. First, GO is generally insoluble to organic solvents, which makes it complicated to incorporate fillers into semi-crystalline polymers through solution mixing. Melt mixing has been generally studied to address this issue, however, due to the poor dispersion and

thermal degradation of GO during harsh processing, the effect of gas reduction with respect to the concentration of GO is typically reported to be lower than our PDMS/GO composite results. Therefore, investigations into different mixing methods, or pre-functionalizing GO in a manner that would still allow for post-crosslinking reactions would help in obtaining practical materials for use in industrial gas barrier membranes.

Appendices

APPENDIX A: SUPPORTING INFORMATION FOR CHAPTER 2

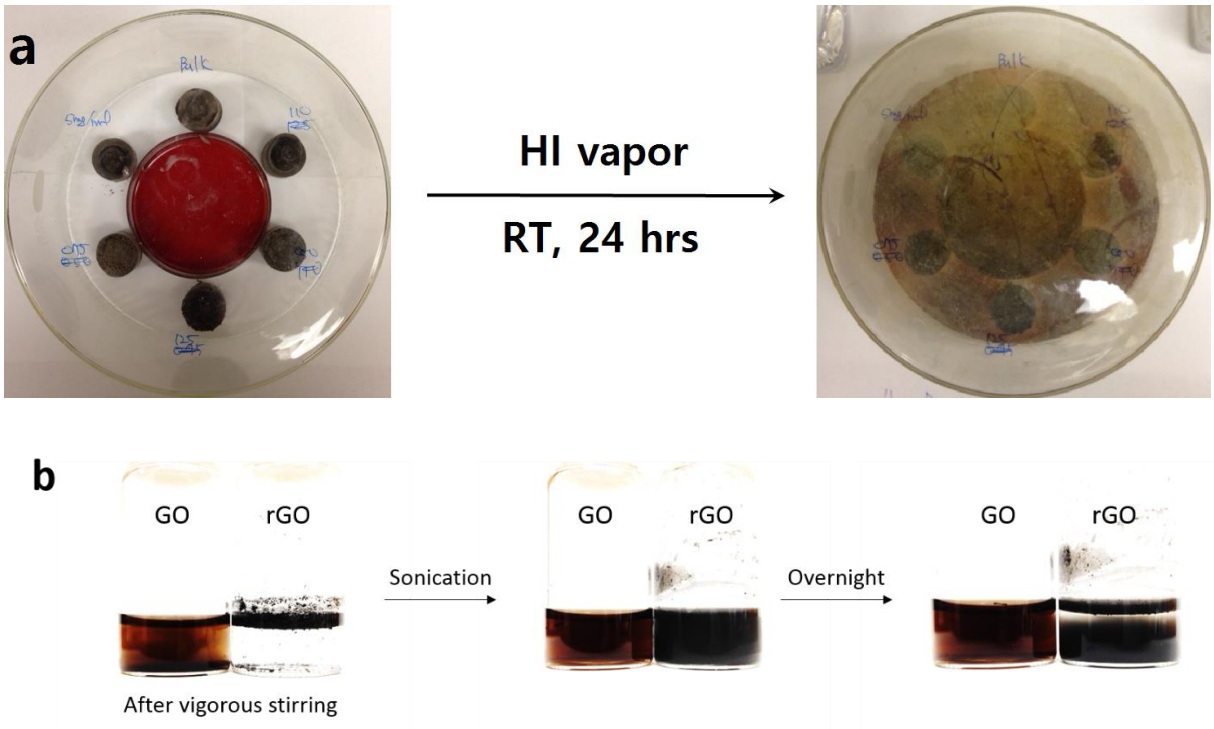

Figure A.1. Images related to the reduction process using HI vapor at room temperature. (a) Before and after 24 hrs. (b) Solubility comparison of GO and rGO in DI water, which is an indirect indication of how effectively GOs are reduced by HI vapor.

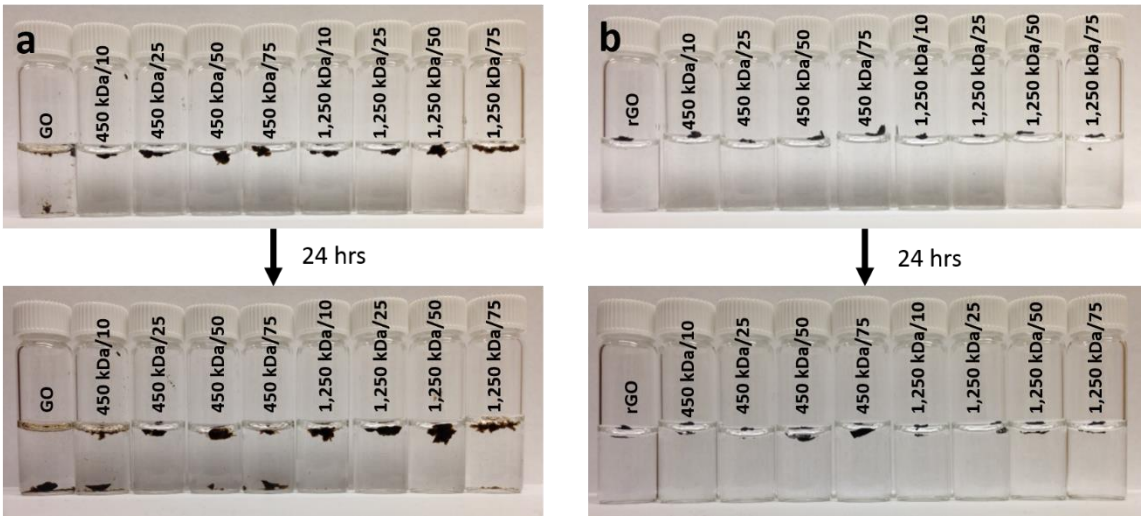

Figure A.2. Solubility comparison of (a) PAA/GO and (b) XPAA/rGO aerogels in DI water at room temperature initially (top) and after soaking in water for 24 hrs (bottom).

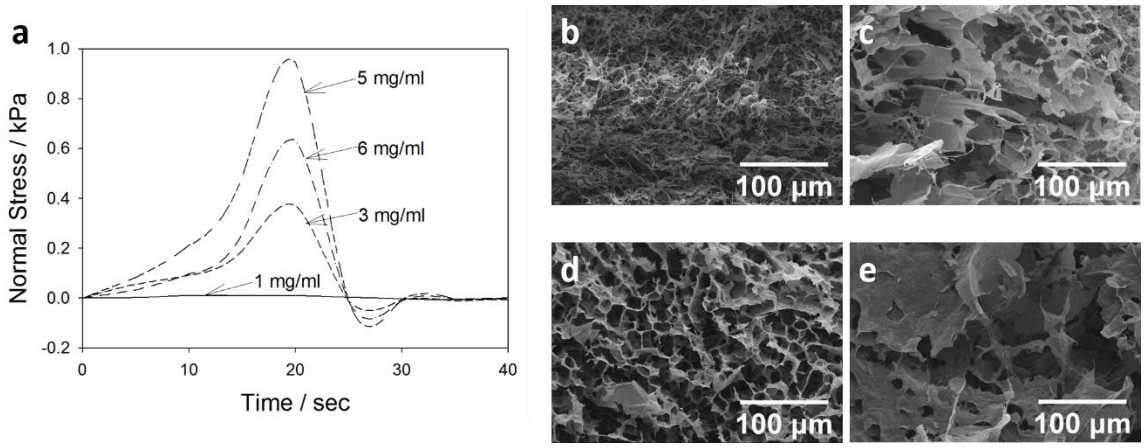

Figure A.3. Compression test results and morphology comparisons for various concentrations of GO aerogels. (a) 1st cycle compression test result conducted using a rheometer. SEM images of GO aerogels depending on the concentration of GO in DI water; (b) 1 mg/ml, (c) 3 mg/ml, (d) 5 mg/ml, and (e) 6 mg/ml.

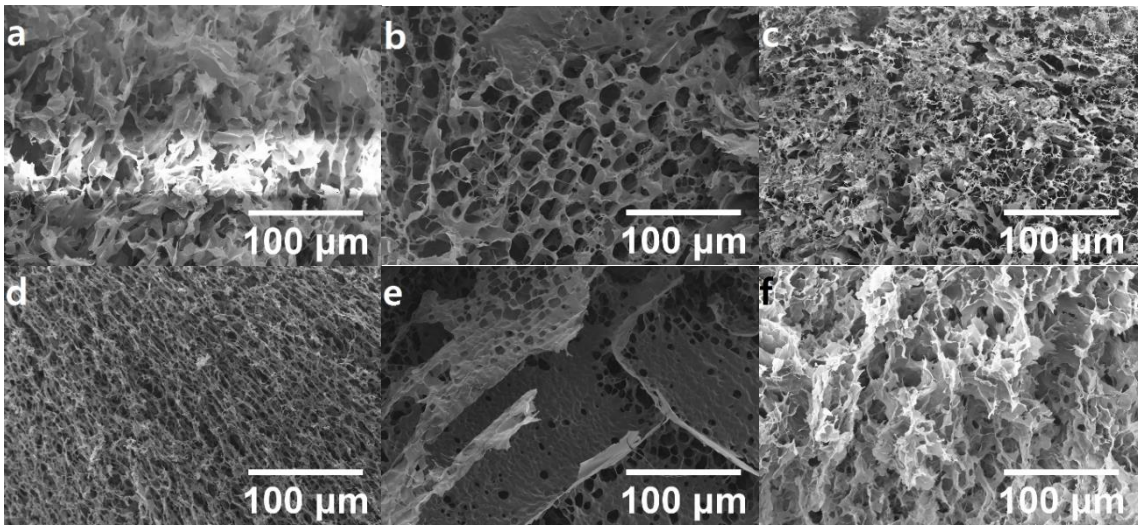

Figure A.4. Cross-sectioned SEM images of freeze-dried PAA/GO aerogels before reducing or thermal annealing: (a) 450 kDa/25, (b) 450 kDa/50, (c) 450 kDa/75, (d) 1,250 kDa/25, (e) 1,250 kDa/50, and (f) 1,250 kDa/75.

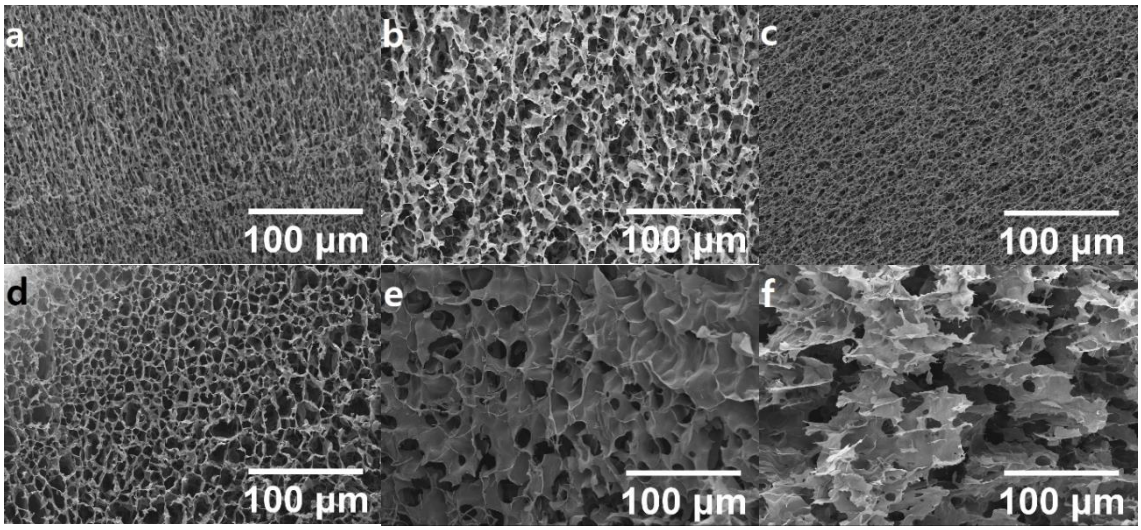

Figure A.5. Cross-sectioned SEM images of freeze-dried XPAA/rGO aerogels after HI vapor reduction and thermal annealing at 160 °C for 24 hrs: (a) 450 kDa/25, (b) 450 kDa/50, (c) 450 kDa/75, (d) 1,250 kDa/25, (e) 1,250 kDa/50, and (f) 1,250 kDa/75.

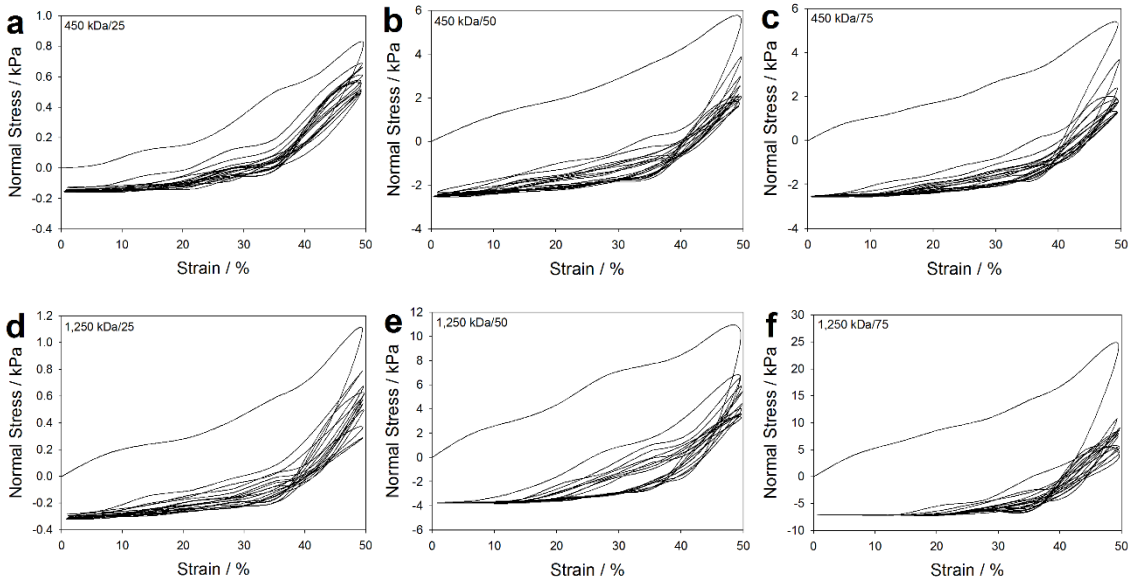

Figure A.6. Compression-release cycle test results for all of the XPAA/rGO aerogel samples during 10 consecutive cycles.

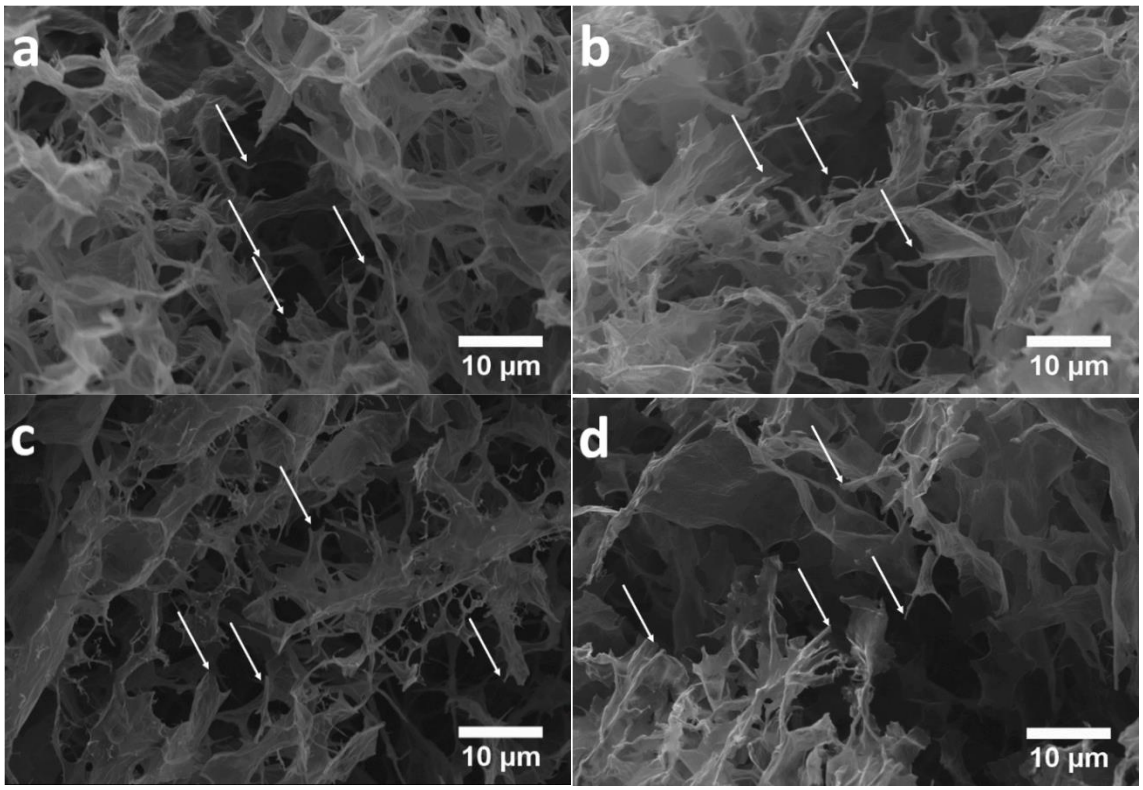

Figure A.7. Cross-sectional SEM images of XPAA/rGO aerogels taken parallel and perpendicular to the direction of compression/release after 10 cycles. 450 kDa/50 (a) parallel and (b) perpendicular and 450 kDa/75 (c) parallel and (d) perpendicular. White arrows indicate the location of fracturing of rGO and/or XPAA structural elements which are shown as a fractured dangling threads.

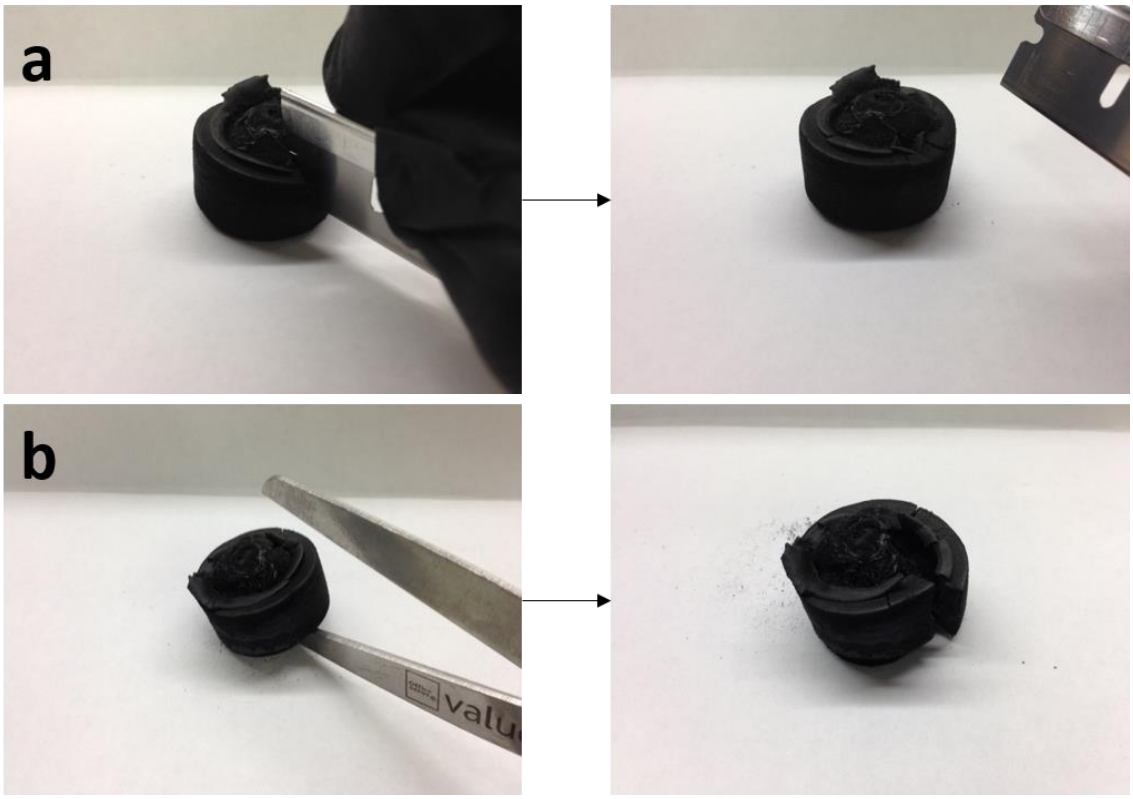

Figure A.8. Mechanical integrity of pure rGO aerogels. (a) Attempt to cut the aerogel with a razor blade. Due to their relatively weak mechanical properties, the rGO aerogel is significantly squeezed during cutting, leaving a large rupture with additional cracks formed near the contact point. (b) Attempt to cut the rGO aerogel with a pair of scissors. Aerogels are torn rather then cut clean, as well as leaving large amount of rGO particles that have been disengaged from the aerogel itself.

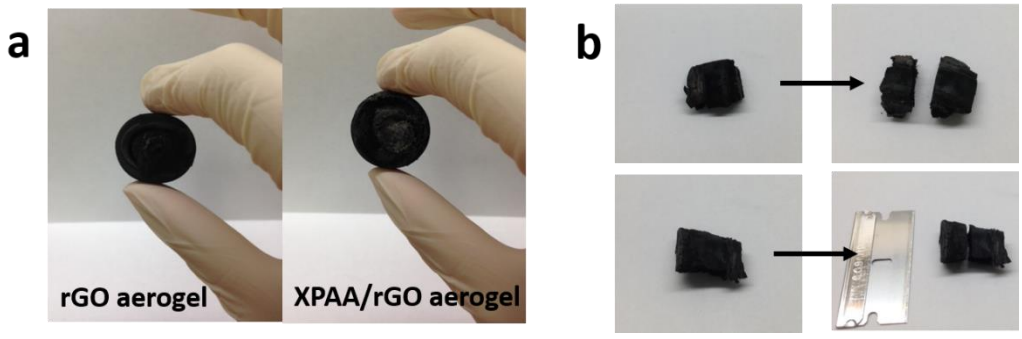

Figure A.9. Images of the mechanical integrity and robustness of XPAA/rGO aerogels. (a) Hand-held rGO (left) and XPAA/rGO aerogel (right). (b) Small portion of 450 kDa/75 XPAA/rGO aerogel cut clean without damaging the structure using (top) a pair of scissors, and (bottom) a razor blade.

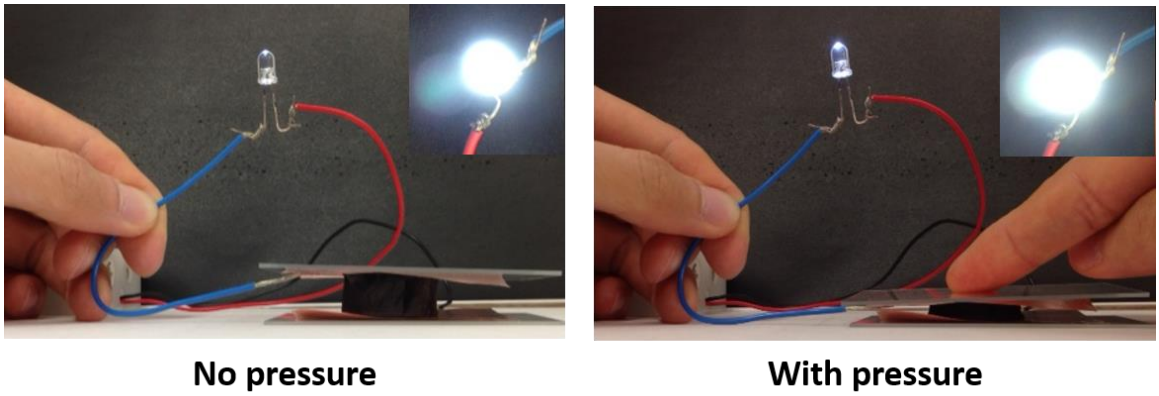

Figure A.10. Full image of a simple circuit constructed with a LED lamp. The inset images compare the brightness of the LED lamp from above.

Table A.1. T_g changes of PAA with different molecular weights depending on the annealing time at 160 ºC. All of the T_g data were collected from the DSC 2nd heating curves as midpoint values. For 1,250 kDa M_v PAA, glass transition behavior becomes broad enough that it was hard to determine the exact T_g. Ramp rate: 20 ºC/min.

M_v of PAA	**Annealing Time (hr)**	**T_g (°C)**
450 kDa	0	133.5
	1	140.0
	2	156.1
	4	169.9
	8	173.1
	24	174.8
1,250 kDa	0	132.1
	1	133.9
	2	134.0
	4	Broad (> 150.0)
	8	Broad (> 150.0)
	24	Broad (> 150.0)

APPENDIX B: SUPPORTING INFORMATION FOR CHAPTER 3

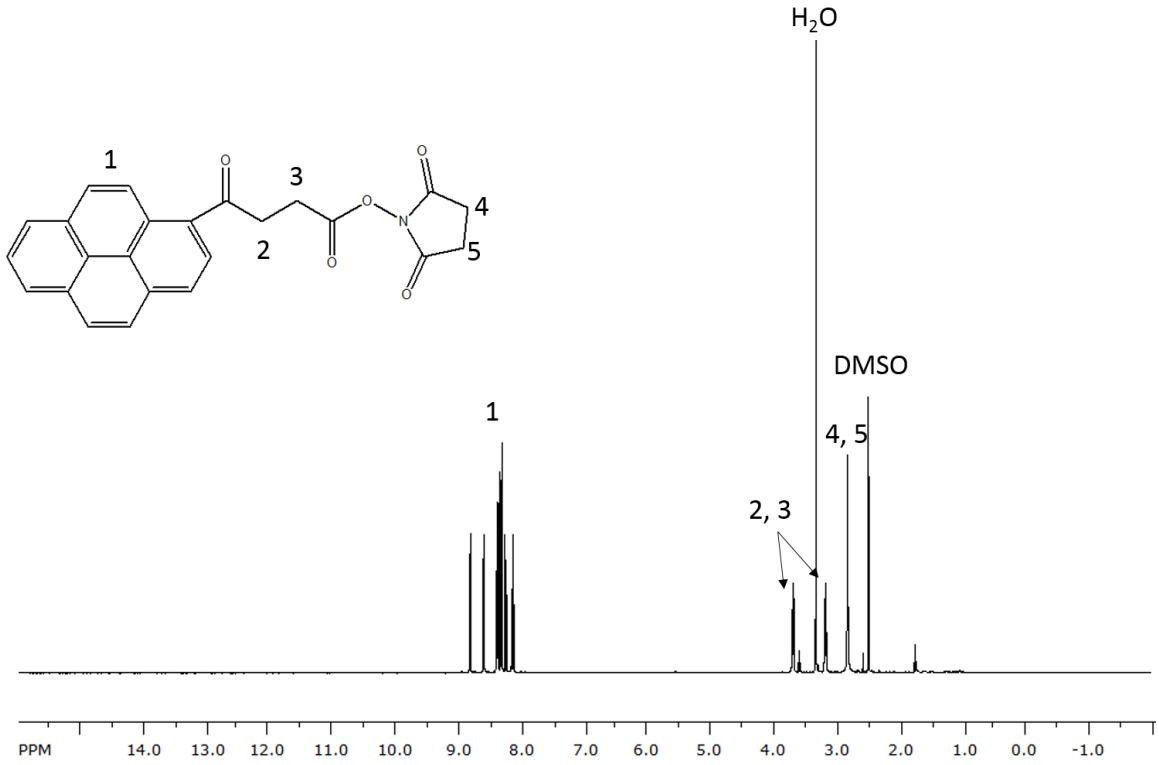

Figure B.1. Proton NMR spectrum for OPBA NHS Ester.

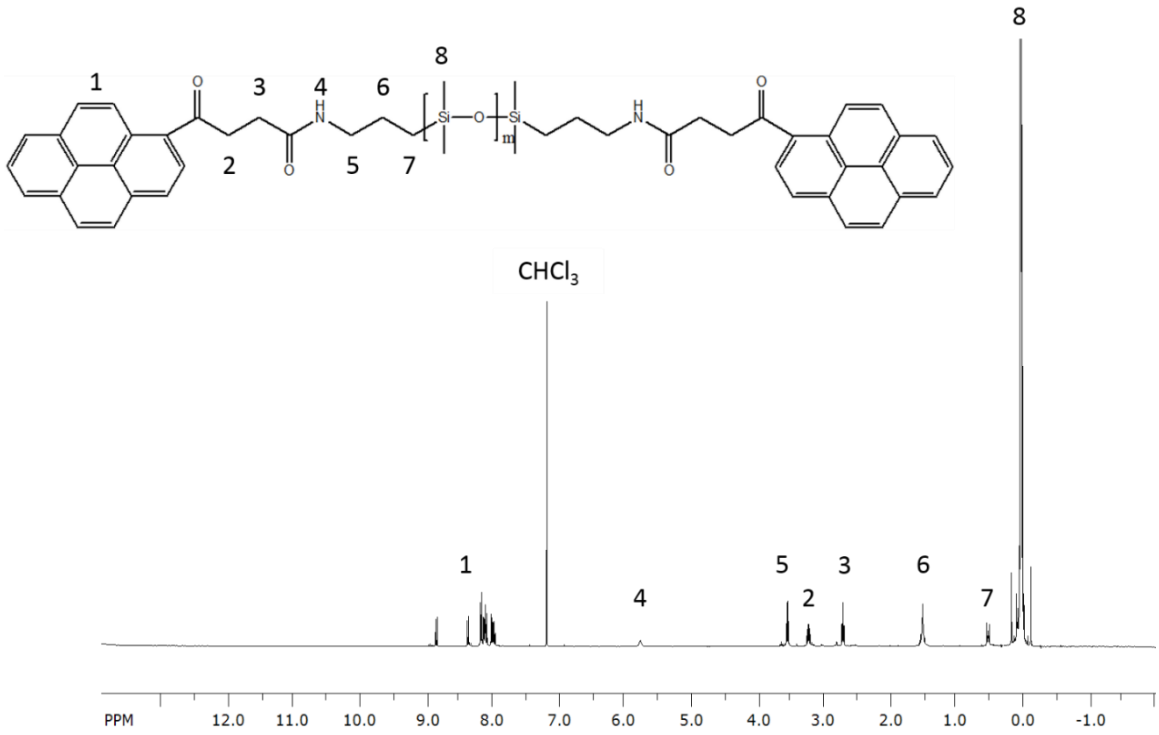

Figure B.2. Proton NMR spectrum for pyrene end-functionalized PDMS.

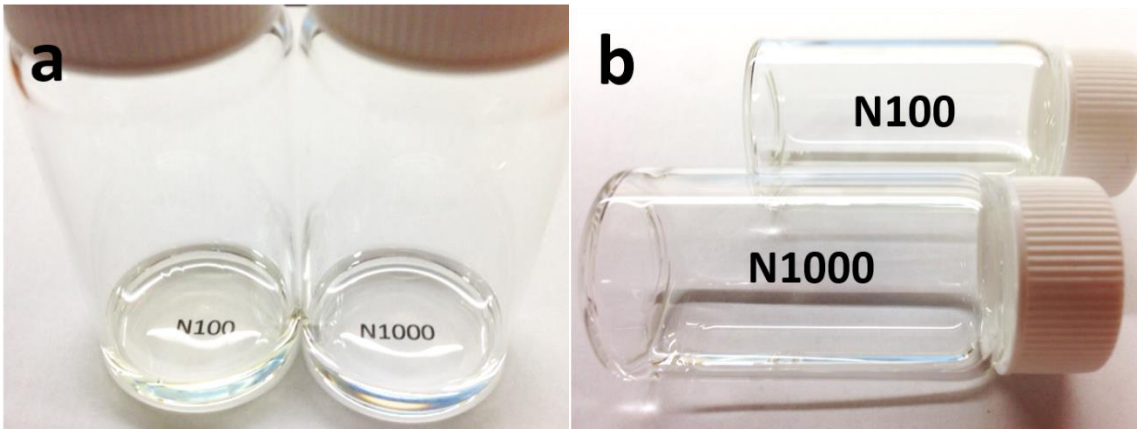

Figure B.3. Images of N series PDMS for comparison. a) N100 (left) and N1000 (right) both show good transparency at room temperature. b) N100 (top) and N1000 (bottom) both flow easily as liquids.

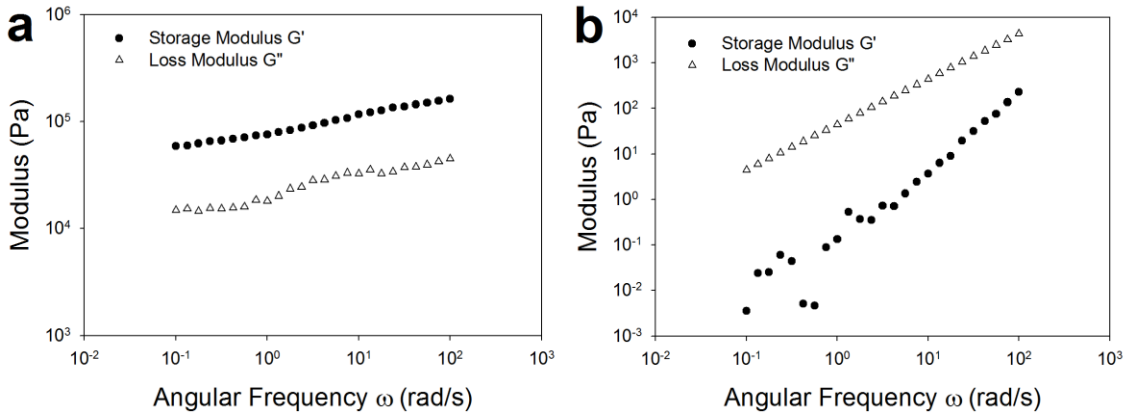

Figure B.4. Dynamic moduli as a function of angular frequency by varying temperatures for (a) P100 and (b) P1000. A portion of G' data were not collected for P1000 due to the instrument limits.

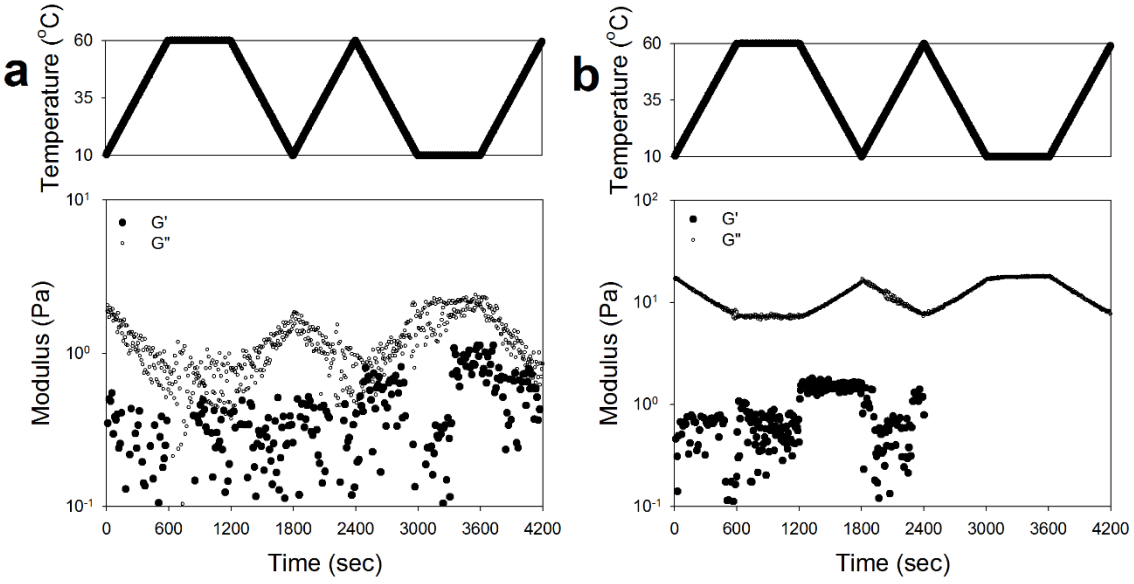

Figure B.5. Dynamic moduli (bottom) during a designated heat cycle (top) for a) N100 and b) N1000. Some portion of the data was not collected due to instrument limitations.

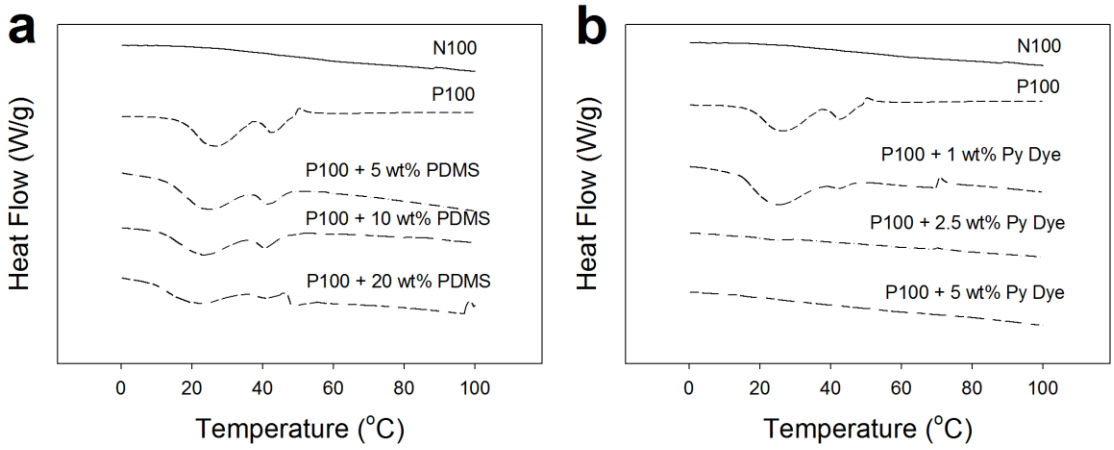

Figure B.6. DSC thermograms of P100 by adding different amounts of (a) pure PDMS, and (b) free pyrene (OPBA NHS ester; Py dye).

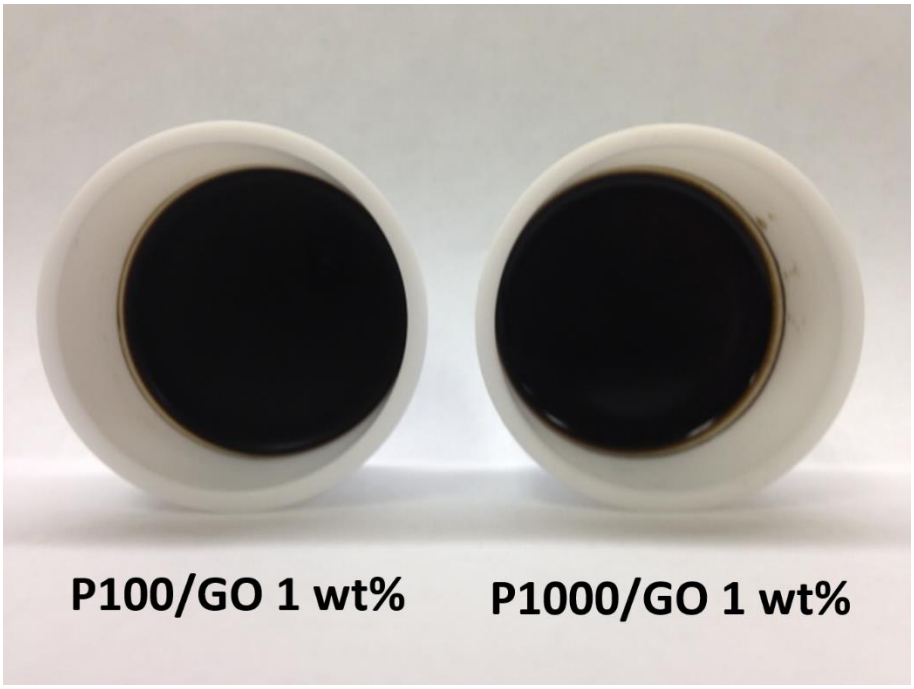

Figure B.7. Images of P100/1 wt% GO (left) and P1000/1 wt% GO (right) nanocomposite gel in a PTFE dish. Both of the samples do not flow, which indicates that they are in the solid state.

APPENDIX C: SUPPORTING INFORMATION FOR CHAPTER 4

1. Neat PDMS elastomer (reference/control material) synthesis procedure for single gas permeation experiments

Neat PDMS sample was synthesized by reacting aminopropyl terminated telechelic PDMS and epoxypropoxypropyl terminated PDMS. The chemical structures of the two components are illustrated below.

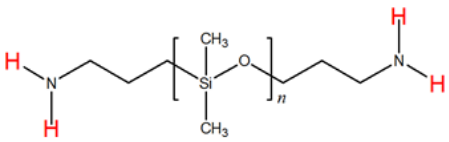

M_n = 25,000 g/mol
(N1000)

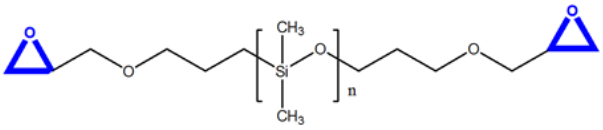

M_n = 550 g/mol
(diepoxy)

Typically, aminopropyl terminated telechelic PDMS (e.g. N1000) was reacted in THF with a 5-fold molar excess of epoxypropoxypropyl terminated PDMS (henceforth referred to as diepoxy). Depending on the molecular weight of the PDMS material, the weight ratio between the two components were adjusted accordingly. Assuming that the amine terminated PDMS has 4 active sites (4 H atoms at the ends, each are capable of reacting with an epoxy) and diepoxy has 2 active sites, calculating the extent of reaction at the gel point by Flory's method gives a value very near to 1. After solution casting a film in a PTFE dish, the mixture was annealed at 160 °C similarly to other PDMS/GO composite elastomer materials. It is noteworthy that using less diepoxy will still form an elastomer, but the material after heating was weak and sticky which complicated additional post-processing.

2. Confirming the dispersion of GOs in the composite material

The dispersion of GOs in the composite material was confirmed by optical microscope (OM; Olympus BX60) using a microtomed sample on a 400 mesh Cu grid. It was difficult to prepare a defect free microtomed sample having a thickness less than 100 nm due to several reasons. First, due to the low T_g of the composite materials (approximately -120 °C), the microtome was conducted at -150 °C. To the best of our knowledge, no solvent or mixture of solvents were available which do not freeze at this temperature. Second, without having any solvent to float the sectioned sample, we placed the sample manually on a Cu grid using an eyelash tool. When the sample was heated back to room temperature, sectioned samples relaxed considerably, giving rise to wrinkled or uneven surfaces. Generally, samples prepared this way were not suitable for TEM imaging (i.e., the images were black with little contrast). However, OM showed a clear evidence of the presence of GOs, and the corresponding images of all of the samples studied in this research are presented below.

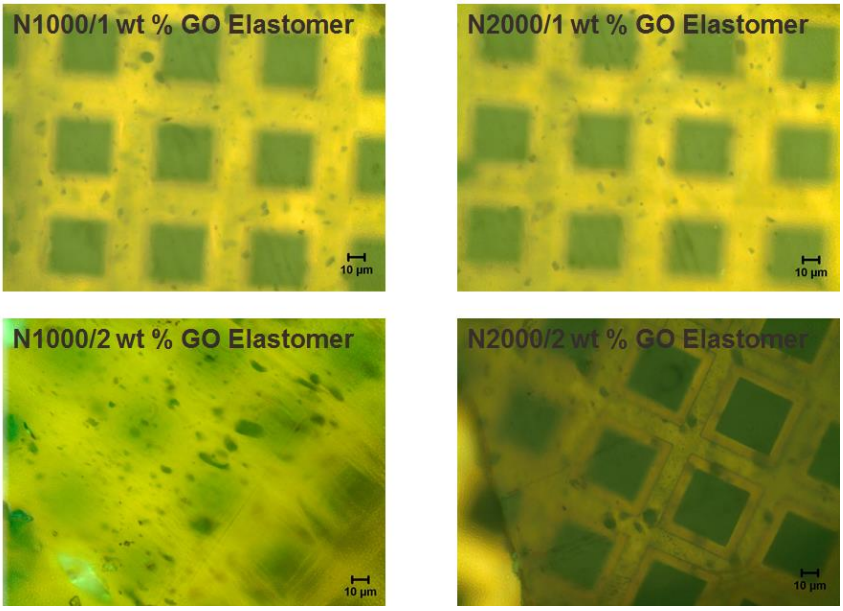

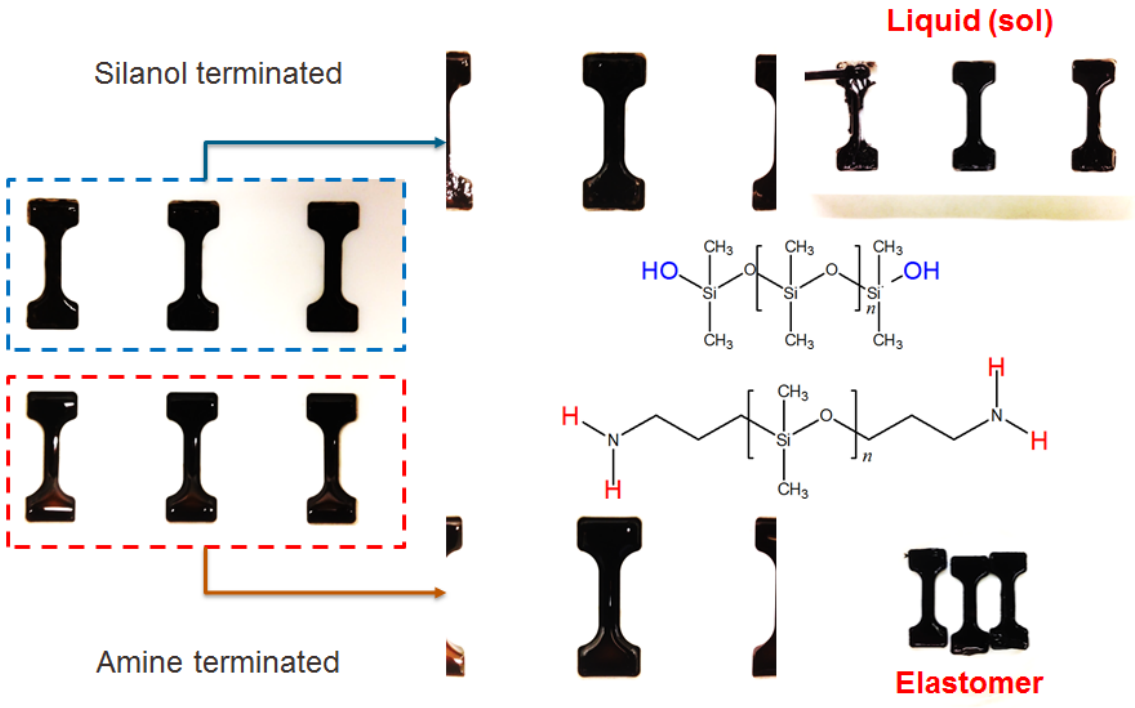

Figure C.1. Microtensile testing samples prepared by reacting (top) silanol terminated PDMS with 1 wt % GO and (bottom) amine terminated N1000 with 1 wt % GO. While the viscosity of both materials were identical, only amine terminated PDMS was capable of forming a freestanding elastomer. Silanol terminated PDMS samples were liquid sol after annealing.

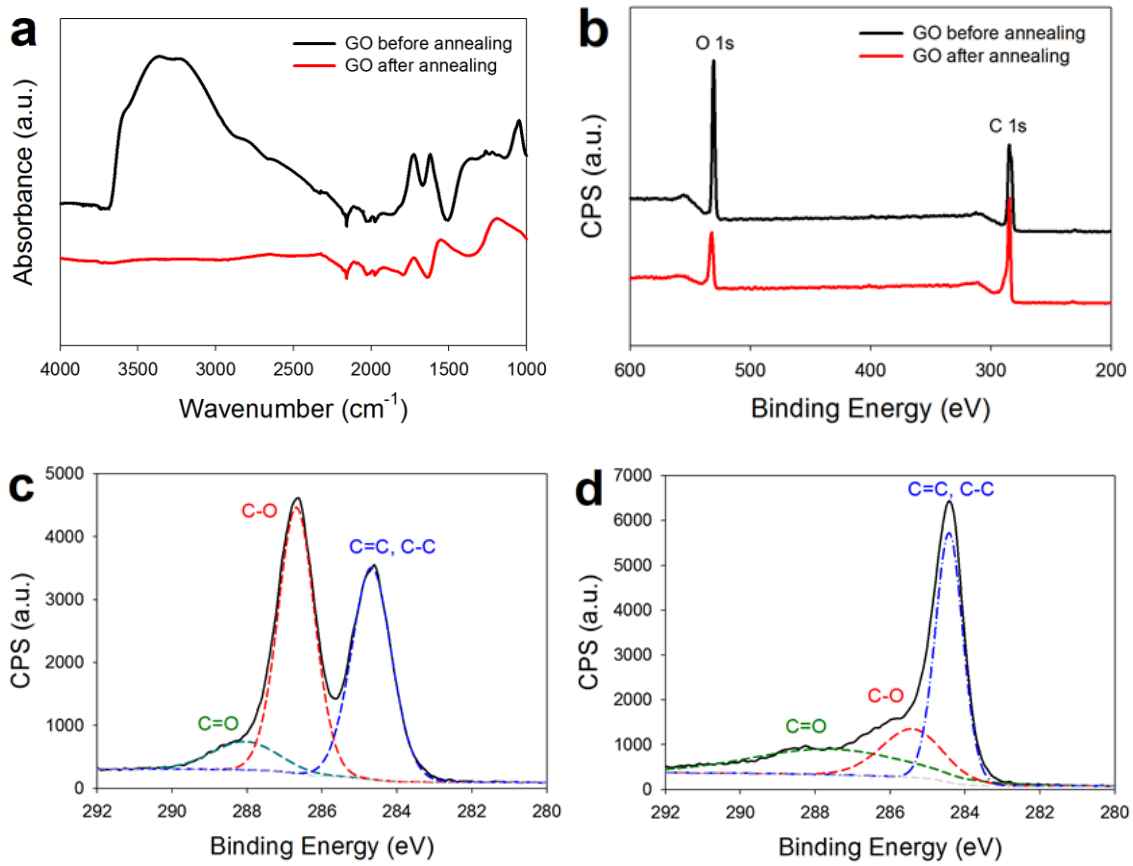

Figure C.2. (a) FTIR spectra before and after annealing GO. FTIR spectra have been shifted vertically for clarity but are otherwise on the same scale. For GO before annealing, a broad band –OH stretching was observed around 3380 cm^{-1}, C=O stretching at 1730 cm^{-1}, and epoxide group C-O stretching at 1260 and 1050 cm^{-1}. A strong peak assumed to be vibration of water molecules adsorbed on GO was observed at 1620 cm^{-1}. After annealing the same GO in vacuum at 160 °C, -OH stretching and epoxy C-O stretching peaks decreased significantly, while C=C stretching peak at 1560 cm^{-1} increased substantially. (b) XPS survey and C 1s spectra for (c) GO before annealing, and (d) GO after annealing. The main oxygen containing components of GO arising from C=O (288.1 eV) and C-O (286.7 eV) groups are significantly reduced after annealing. On the other hand, C=C, C-C (284.6 eV) becomes dominant after annealing, as shown by one single peak with a shoulder at higher binding energy. Thus, while the crosslinking reaction takes place between telechelic PDMS materials and GOs, GOs will be slightly reduced as well.

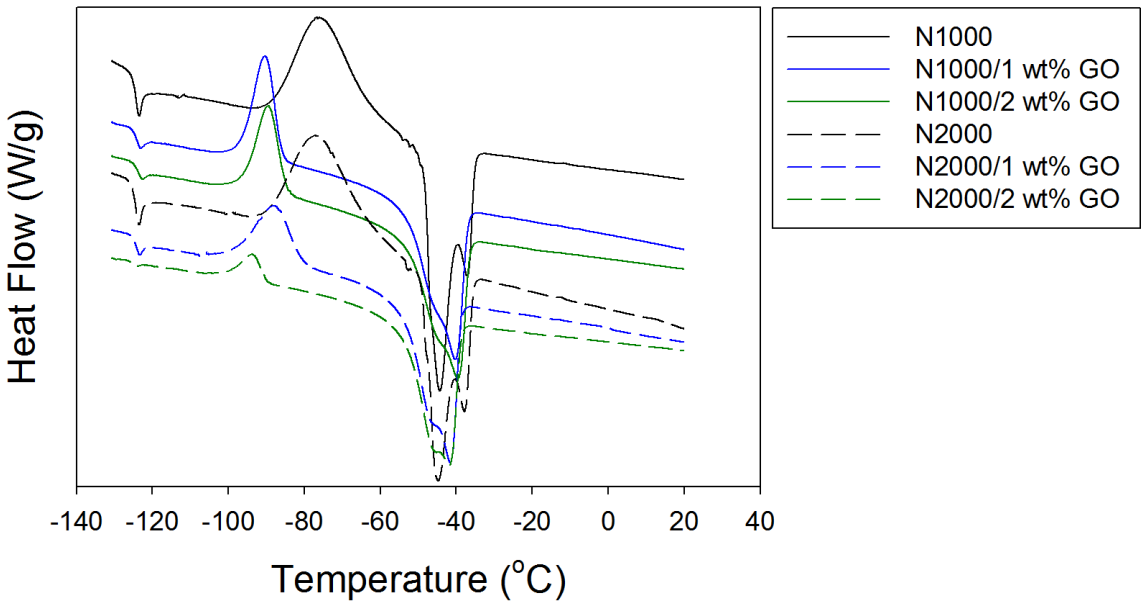

Figure C.3. DSC thermogram comparison between neat telechelic PDMS materials and PDMS/GO composite elastomers. The glass transition temperature (T_g) and melting temperature (T_m) of all of the materials are essentially identical. The decrease in cold crystallization temperature (T_{cc}) is due to GOs and chemical crosslinks acting as an effective nucleating agent in the system.

Table C.1. Detailed peak assignments for the FTIR spectra in Figure 2 (a). Although N-H asymmetric/symmetric stretching and C-N stretching peaks are listed below, it was difficult to identify these peaks due to overlapping with other dominant peaks.

Wavenumber (cm^{-1})	**Mode**
3380	*N-H asymmetric stretching*
3326	*N-H symmetric stretching*
2962	CH_3 asymmetric stretching
2905	CH_3 symmetric stretching
1600	N-H bending (broad)
1445	CH_3 asymmetric bending shoulder
1412	CH_3 asymmetric bending
1258	CH_3 symmetric bending
1020-1250	*C-N stretching (weak)*
1080	Si-O-Si asymmetric stretching
1009	Si-O-Si symmetric stretching
786	CH_3 asymmetric rocking Si-C asymmetric stretching
702	Si-C symmetric stretching

Table C.2. Raw data obtained for single gas permeability of neat PDMS and N1000/1 wt % GO elastomer.

Neat PDMS									
P (atm)	**CO_2 (Barrer)**	**P (atm)**	**CH_4 (Barrer)**	**P (atm)**	**H_2 (Barrer)**	**P (atm)**	**O_2 (Barrer)**	**P (atm)**	**N_2 (Barrer)**
3.19	3767.66	3.05	1320.96	3.17	955.64	3.36	848.97	3.12	430.36
6.61	3969.28	6.66	1332.61	6.52	948.96	6.75	845.12	6.74	422.56
9.90	4096.77	10.03	1344.57	9.89	949.55	9.91	848.10	10.10	421.36
13.42	4194.19	13.72	1353.88	13.23	953.00	13.42	849.90	13.50	418.14
16.94	4359.79	16.53	1364.34	16.69	952.73	16.90	851.36	16.75	417.90

N1000/1 wt % GO Elastomer									
P (atm)	**CO_2 (Barrer)**	**P (atm)**	**CH_4 (Barrer)**	**P (atm)**	**H_2 (Barrer)**	**P (atm)**	**O_2 (Barrer)**	**P (atm)**	**N_2 (Barrer)**
3.02	2138.21	3.16	642.65	3.04	664.71	3.08	427.22	3.06	226.40
6.46	2232.71	6.43	656.54	6.43	659.49	6.55	454.28	6.55	232.28
9.82	2429.76	9.85	677.93	9.84	652.23	9.93	464.96	9.94	233.41
13.17	2476.78	13.26	706.16	13.24	642.51	13.26	471.04	13.10	233.80
16.65	2559.57	16.69	703.64	16.65	640.16	16.69	477.94	16.80	233.42

Table C.3. % reduction in gas permeability for various polymer/filler composites from selected literature. R_x represents % reduction of gas permeability for gas x with respect to neat polymer.

Polymer	Filler Type	Loading (vol %)	Operation conditions	R_{H_2}	R_{O_2}	R_{N_2}	R_{CH_4}	R_{CO_2}	Ref.
PU	Clay	3.0	23 °C, 1 atm	-	30	-	-	-	[1]
PC	G	6.7	35 °C, 1 atm	-	-	36	-	-	[2]
PC	TRG	1.6		-	-	44	-	-	[2]
PP	GNP	3.0	25 °C, 1 atm	-	20	-	-	-	[3]
PS	fGO	0.93* (2 wt %)	N/A	-	25	59	-	-	[4]
Telechelic PDMS	GO	0.43	35 °C, 10 atm	31	45	44	50	40	This Work

PU: polyurethane, PC: polycarbonate, PP: polypropylene, PS: polystyrene, PDMS: poly(dimethylsiloxane), Clay: alumino-silicate, G: graphite, TRG: thermally reduced graphene oxide, GNP: graphite nanoplatelets, fGO: functionalized graphene oxides for in situ polymerization, GO: graphene oxide prepared by modified Hummer's method. * volume percent was calculated arbitrarily using the following densities: PS = 1.05 g/cm^3, fGO = 2.28 g/cm^3.

REFERENCES

[1] Osman M a., Mittal V, Morbidelli M, Suter UW. Polyurethane adhesive nanocomposites as gas permeation barrier. Macromolecules 2003;36:9851–8. doi:10.1021/ma035077x.

[2] Kim H, Macosko CW. Processing-property relationships of polycarbonate/graphene composites. Polymer 2009;50:3797–809. doi:10.1016/j.polymer.2009.05.038.

[3] Kalaitzidou K, Fukushima H, Drzal LT. Multifunctional polypropylene composites produced by incorporation of exfoliated graphite nanoplatelets. Carbon 2007;45:1446–52. doi:10.1016/j.carbon.2007.03.029.

[4] Yu Y-H, Lin Y-Y, Lin C-H, Chan C-C, Huang Y-C. High-performance polystyrene/graphene-based nanocomposites with excellent anti-corrosion properties. Polym Chem 2014;5:535–50. doi:10.1039/C3PY00825H.

APPENDIX D: SUPPORTING INFORMATION FOR CHAPTER 5

In order to fit theoretical models to the gas permeability data from thermally crosslinked amine terminated telechelic PDMS/graphene oxide (GO) elastomers, initially three well-known models were considered.

1) Maxwell model: The Maxwell model was originally applied to electric current transport in systems in which the dispersed phase consisted of a low volume fraction of conductive spherical particles [1]. For this study, we assumed the permeability of the dispersed phase (P_d) is nearly 0, since it is well acknowledged that graphene or graphene derivatives such as GO act as an impermeable barrier [2].

$$\frac{P_c}{P_m} = 1 + \frac{3\phi_d}{\left[\frac{\frac{P_d}{P_m}+2}{\frac{P_d}{P_m}-1}\right]-\phi_d} = 1 - \frac{3\phi_d}{\phi_d+2} \qquad \text{(Eq. 1)}$$

P_c is the permeability of the composite, Pm is the permeability of the neat matrix, and Φ_d is the volume fraction of the dispersant.

A more generalized form of Maxwell model is given by the following equation.

$$\frac{P_c}{P_m} = 1 + \frac{(1+G)\phi_d}{\left[\frac{\frac{P_d}{P_m}+G}{\frac{P_d}{P_m}-1}\right]-\phi_d} \qquad \text{(Eq. 2)}$$

where G is a geometric factor accounting for the filler shape. For spheres G = 2 (same with Eq. 1) and for cylinders G = 1. In the case of platelet fillers, G is infinity if the platelets are aligned parallel to the gas flux and 0 if they are oriented normal to the gas flux direction (i.e., perfectly aligned). However, when we assume G = 0 (platelets) and

$P_d/P_m = 0$, the resulting $P_c/P_m = 0$ which makes it impossible to model the experimental results. Therefore, the Maxwell model was not considered further this study.

2) Modified Nielsen model: This model has shown to be most accurate in predicting relative permeability coefficients (P_c/P_m) in nanocomposites having randomly distributed nanofillers with high aspect ratio at very dilute concentrations. It is anticipated that this model will underestimate the efficiency of the filler to alter permeability at high filler loadings, since GO tends to align themselves due to gravity during the solution casting process.

$$\frac{P_c}{P_m} = \frac{1-\phi_d}{1+\frac{\alpha}{6}\phi_d} \quad \text{(Eq. 3)}$$

α represents aspect ratio of the dispersant and henceforth, it is defined as length divided by the thickness of the fillers. For fillers aligned parallel to the bottom surface can be expressed as:

$$\frac{P_c}{P_m} = \frac{1-\phi_d}{1+\frac{\alpha}{2}\phi_d} \quad \text{(Eq. 4)}$$

The general form of this equation can be written as below, where S represents the state of alignment of fillers in the composite material. For randomly dispersed fillers S = 0 (same with Eq. 3), and for perfectly aligned fillers S = 1 (same with Eq. 4) [3, 4].

$$\frac{P_c}{P_m} = \frac{1-\phi_d}{1+\frac{\alpha}{3}\left(S+\frac{1}{2}\right)\phi_d} \quad \text{(Eq. 5)}$$

3) Model proposed by Lape and coworkers (modified Cussler model): The original Cussler model assumes a well-ordered stacked array of nanoplatelets that extend through the entire polymer film. It is anticipated that this model will overestimate the result at low GO concentrations, since GO sheets are not perfectly aligned perpendicular to the gas flux direction.

$$\frac{P_c}{P_m} = \left(1 + \frac{1}{4}\frac{\alpha^2 \phi_d^2}{1-\phi_d}\right)^{-1} \quad \text{(Eq. 6)}$$

Later, the same group proposed a modified version of this model suggesting that platelets are well aligned but interspersed randomly within the matrix having a monodisperse filler size.

$$\frac{P_c}{P_m} = \frac{1-\phi_d}{\left(1+\frac{1}{3}\alpha\phi_d\right)^2} \quad \text{(Eq. 7)}$$

The authors successfully demonstrated theories and experimental data for polydisperse fillers having discrete (e.g., a mixture of 50:50 5 μm flakes and 50 μm flakes) or continuous distributions (e.g., flakes having a Gaussian distribution) in sizes as well [5]. However, advanced models were not used in our study for simplicity. It is noteworthy to point out that modified Nielsen and Cussler models used the term "ribbons" instead of fillers or platelets. This "ribbon" has an infinite length, but a finite width and thickness [6]. Aspect ratio was defined originally in the paper as width/thickness for ribbons. For GO in this work, the aspect ratio was calculated as length/thickness as it is typically defined for platelets or disk like fillers (such as GO).

Table D.1. Sample thicknesses as a function of GO content in the composite materials.

Material	Neat PDMS	PDMS/ 1 wt % GO	PDMS/ 2 wt % GO	PDMS/ 3 wt % GO	PDMS/ 4 wt % GO	PDMS/ 5 wt % GO	PDMS/ 8 wt % GO
Average (mm)	0.998	0.354	0.267	0.381	0.285	0.250	0.081
StDev. (mm)	0.021	0.010	0.005	0.012	0.009	0.010	0.007

Table D.2. Table of critical temperatures, kinetic diameters and critical volumes for various single gases [7].

Penetrant	Critical Temperature (K)	Kinetic Diameter (Å)	Critical Volume (cm^3/mol)
H_2	33.24	2.89	65.1
O_2	154.58	3.46	73.4
N_2	126.20	3.64	89.8
CO_2	304.21	3.3	93.9
CH_4	191.05	3.8	99.2

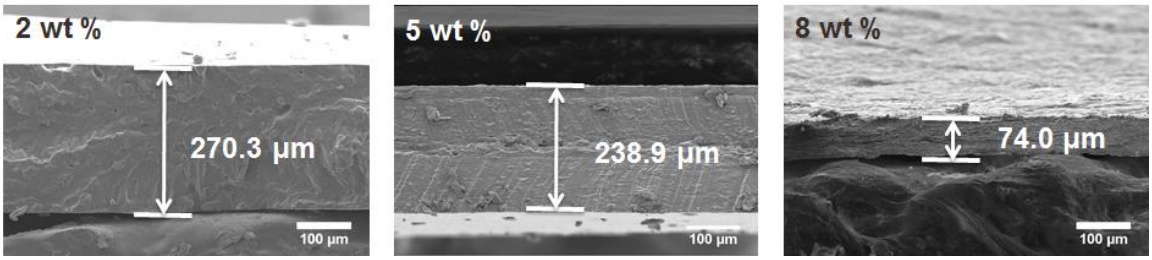

Figure D.1. SEM images for selected samples and their thicknesses. All of the sample thicknesses were in good agreement with Table D.1 data.

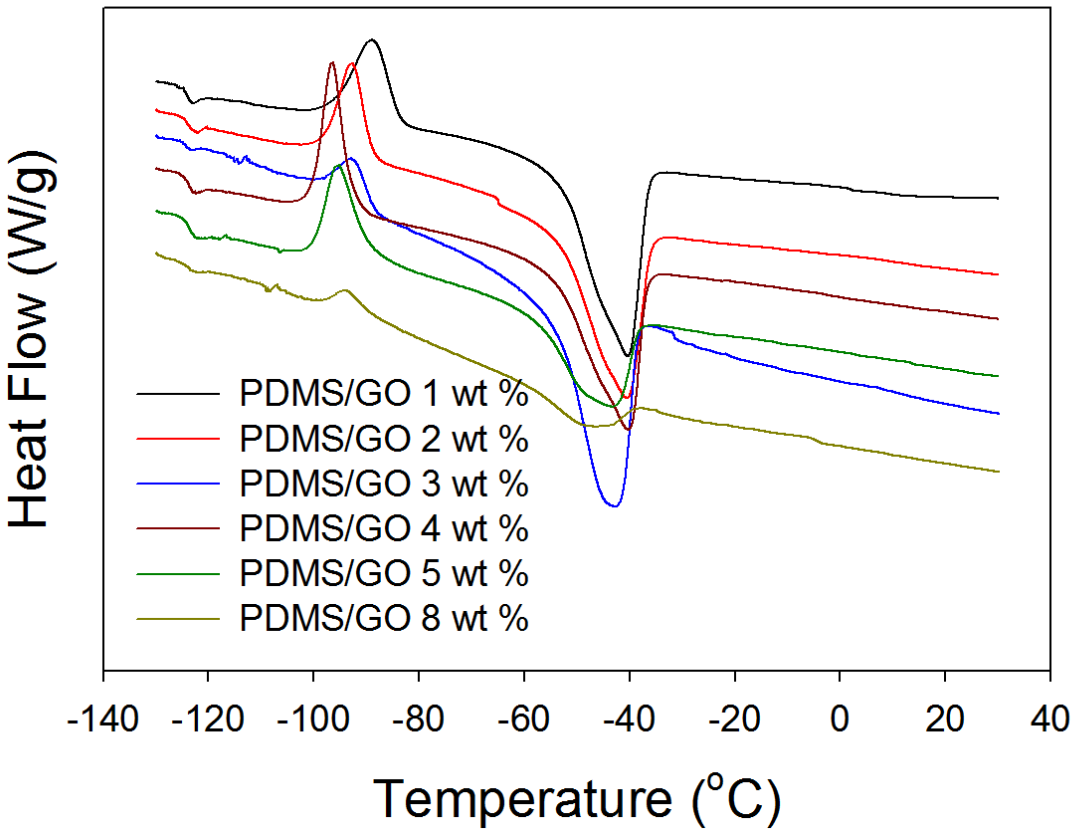

Figure D.2. DSC thermograms comparison between PDMS/GO composite elastomers. The glass transition temperature (T_g) and melting temperature (T_m) were essentially independent of GO content. This indicates that the significant decrease in gas permeability upon addition of GO is mostly due to the impermeable GO dispersed phase and not by the reduction in chain segment mobility in the interstitial amorphous phase. Heat flow was normalized by the total weight of the composite material.

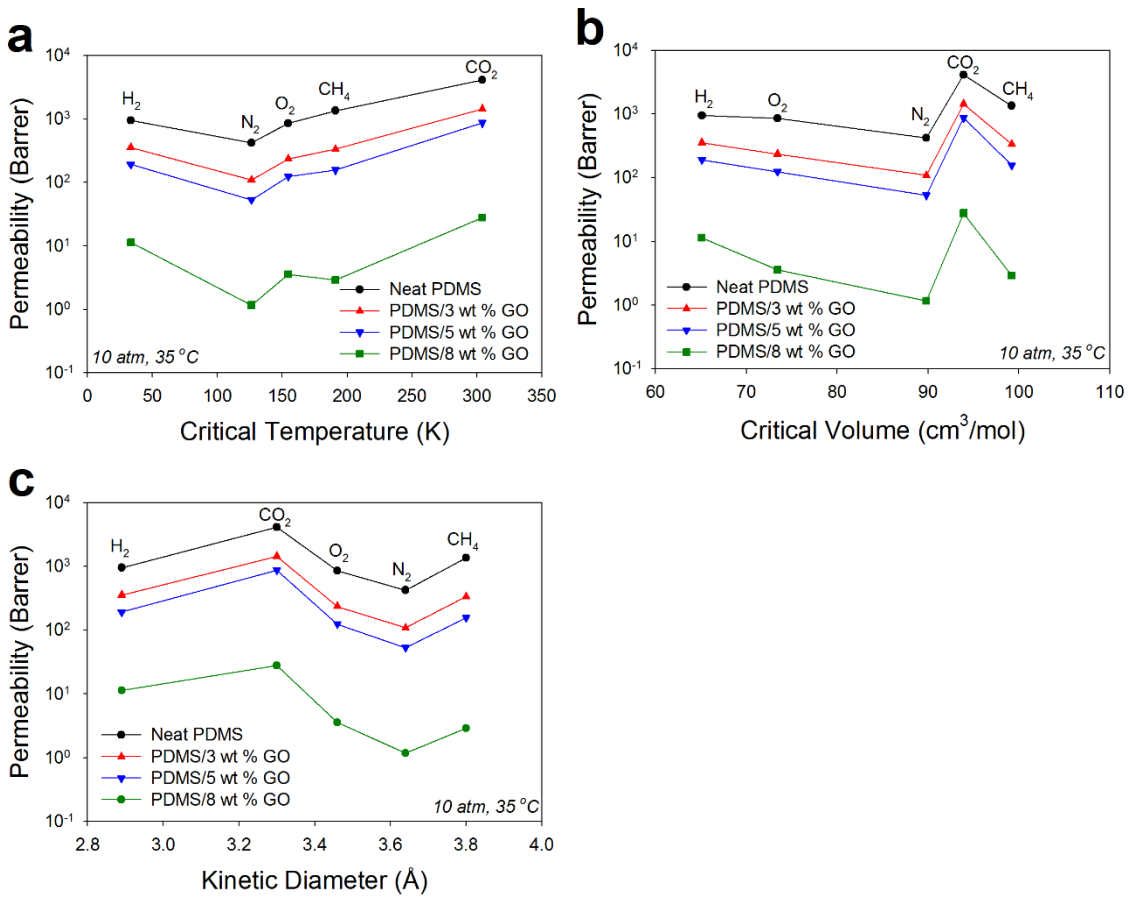

Figure D.3. Permeability of various gases depending on their critical temperatures, critical volumes, and kinetic diameters measured at 10 atm and 35 °C. As mentioned in the main manuscript, the permeability order is strongly dependent on the amount of GO in the composite material.

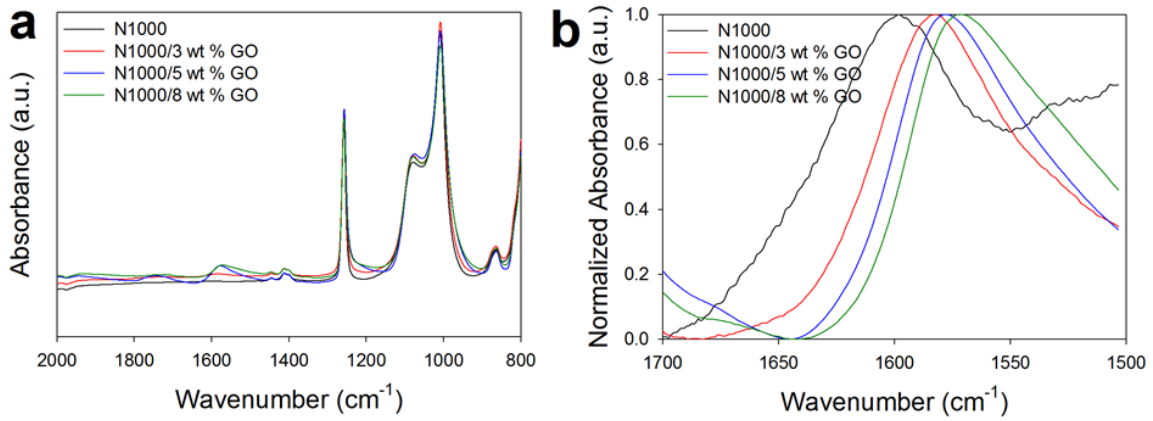

Figure D.4. ATR-FTIR spectra for selected samples. (a) Full scan and (b) normalized absorbance for selected region from 1500-1700 cm^{-1}. The peak associated with N-H bending was assigned at 1600 cm^{-1} for N1000 PDMS sample. After cross-linking the sample in the presence of GO, a significant fraction of the N-H bending peak disappeared, indicating that the majority of the primary amine end groups were reacted during annealing step. In addition, thermal annealing induced reduction reaction of GO to reduced GO and therefore, a strong C=C ring stretching peak at 1570-1580 cm^{-1} was formed for the telechelic PDMS/GO composite elastomer sample [8]. As the concentration of GO increased, the C=C ring stretching shifted from 1582 (3 wt %), 1578 (5 wt %), and 1572 (8 wt %) cm^{-1} due to stronger π-π interactions.

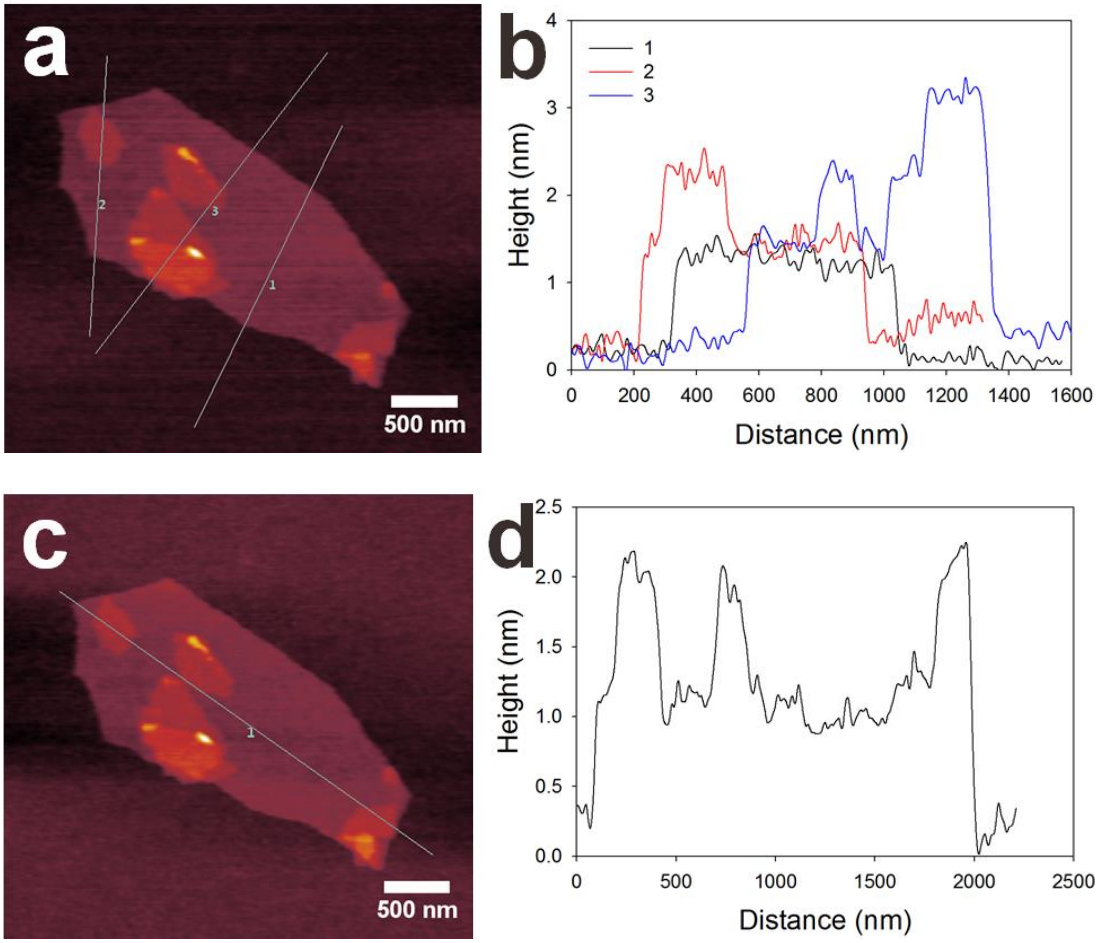

Figure D.5. (a) and (c) are AFM images of pure GO sheets on a Si wafer and (b) profile showing the 1 nm thickness per sheet. With each additional sheet, approximately 1 nm increased in height. The length of the large sheet in (c) was ~ 2 μm. Since the barrier performance of the composite material will be governed by the presence of large impermeable sheets, it is a good approximation to assume the aspect ratio (α) as 1000 (length is 2000 nm and average thickness is about 2 nm).

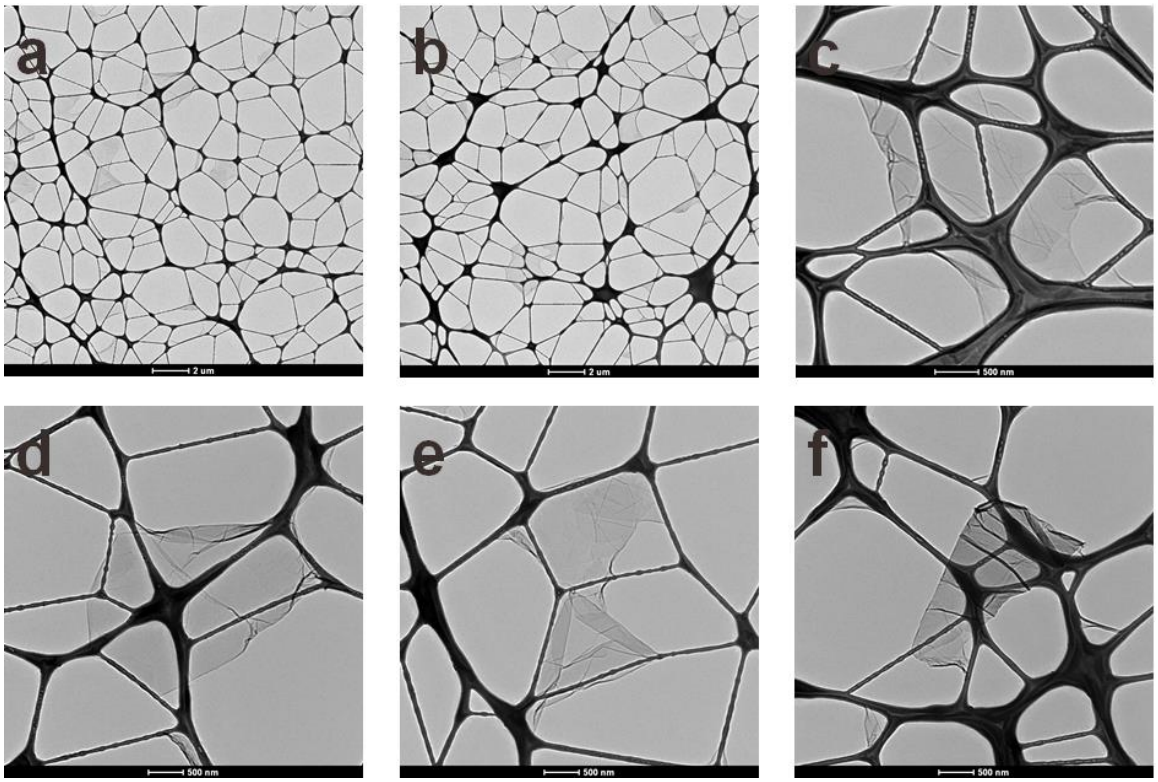

Figure D.6. TEM images of pure GO sheets on a 300 mesh copper Lacey carbon grid. According to low (a-b) and high magnification (c-f) TEM images, GO platelets were present as single or a few stacked layers with lateral dimensions ranging from roughly 1 – 3 μm.

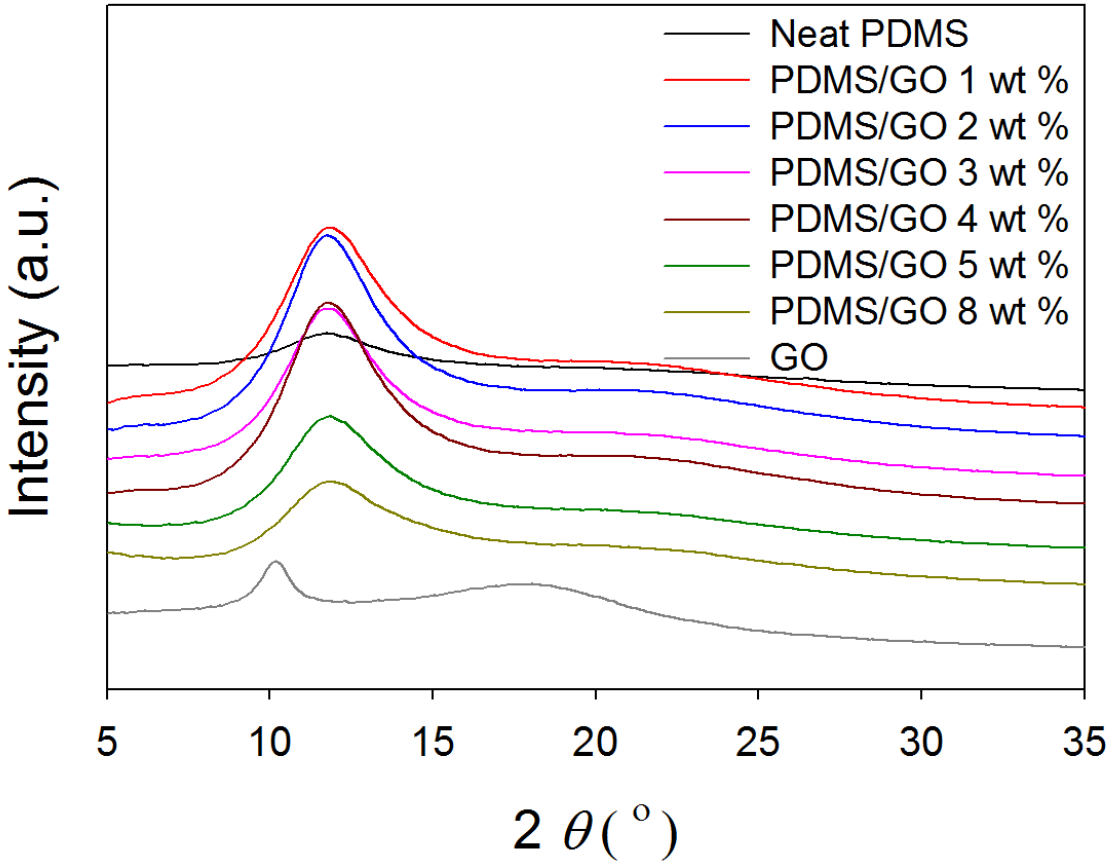

Figure D.7. X-ray diffraction data collected for all of the samples used in this study. For PDMS/GO elastomers, only a broad amorphous halo was detected, while GO showed a definitive (002) crystal peak at around 2θ = 11 ° (d-spacing of 8.03 Å).

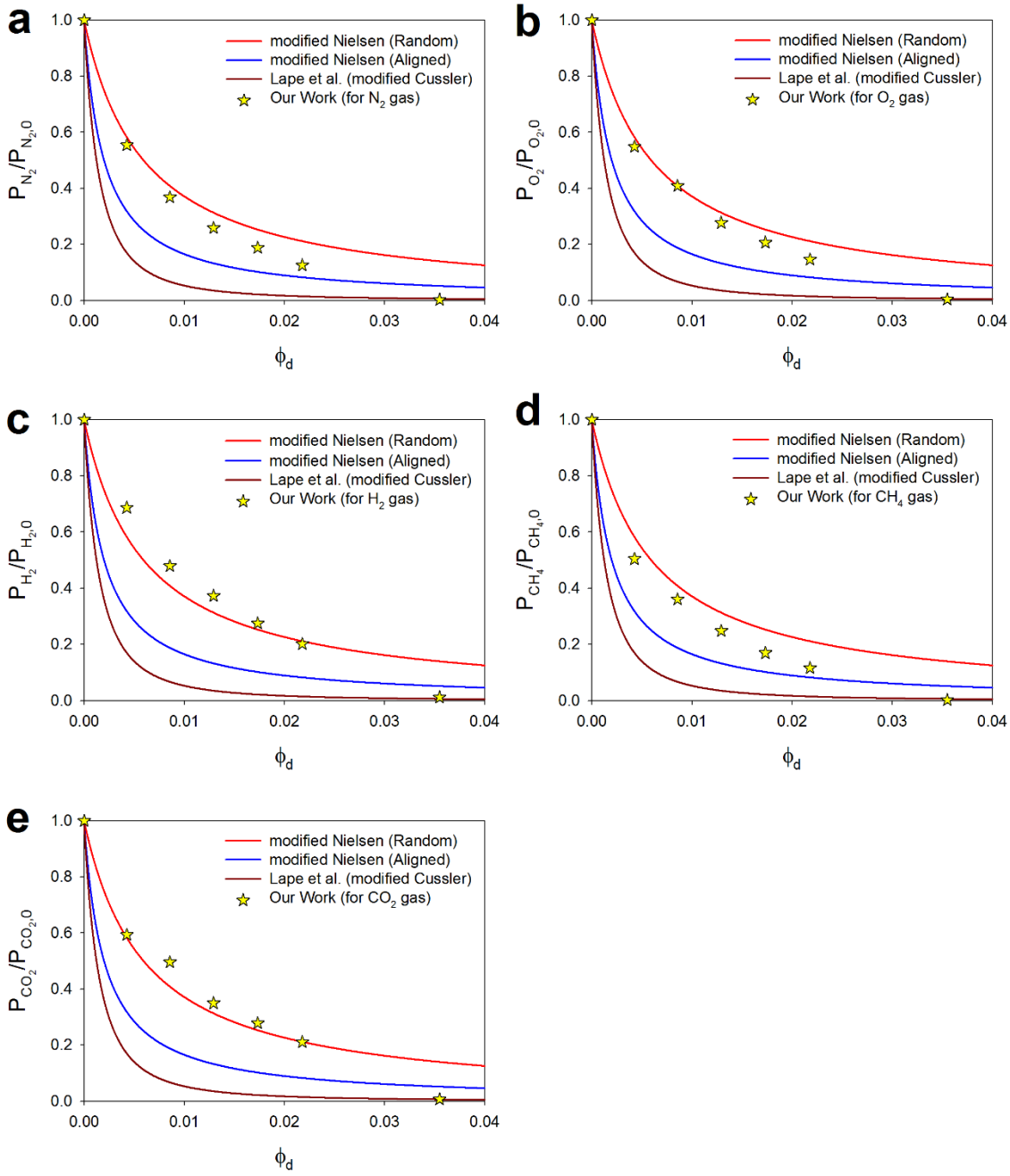

Figure D.8. Modeling results for various single gases at 35 °C, 10 atm. α was assumed to be 1000 and showed reasonable agreements for all cases.

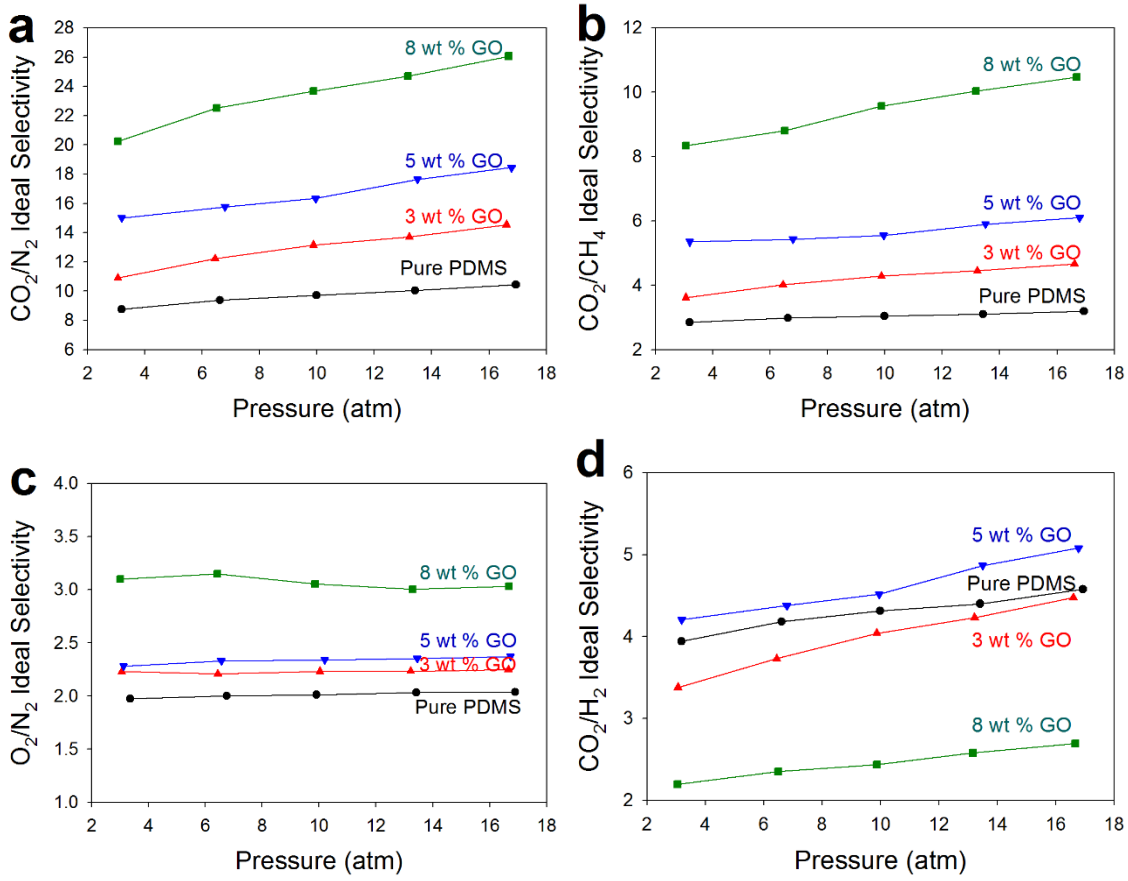

Figure D.9. Various gas selectivities as a function of pressure and GO content.

REFERENCES

[1] Maxwell, J. C. A Treatise on Electricity and Magnetism; Cambridge University Press: Cambridge, 2010.

[2] Su, Y.; Kravets, V. G.; Wong, S. L.; Waters, J.; Geim, A. K.; Nair, R. R. Impermeable Barrier Films and Protective Coatings Based on Reduced Graphene Oxide. Nat. Commun. 2014, 5, 4843.

[3] Choudalakis, G.; Gotsis, A. D. Permeability of Polymer/clay Nanocomposites: A Review. Eur. Polym. J. 2009, 45 (4), 967–984.

[4] Yoo, B. M.; Shin, H. J.; Yoon, H. W.; Park, H. B. Graphene and Graphene Oxide and Their Uses in Barrier Polymers. J. Appl. Polym. Sci. 2014, 131 (1), 39628.

[5] Lape, N. K.; Nuxoll, E. E.; Cussler, E. L. Polydisperse Flakes in Barrier Films. J. Memb. Sci. 2004, 236 (1-2), 29–37.

[6] Paul, D. R.; Robeson, L. M. Polymer Nanotechnology: Nanocomposites. Polymer (Guildf). 2008, 49 (15), 3187–3204.

[7] Baker, R. W. Membrane Technology and Applications; John Wiley & Sons, Ltd: Chichester, UK, 2012.

[8] Ha, H.; Park, J.; Ha, K.; Freeman, B. D.; Ellison, C. J. Synthesis and Gas Permeability of Highly Elastic Poly(dimethylsiloxane)/graphene Oxide Composite Elastomers Using Telechelic Polymers. Polymer (Guildf). 2016.

Bibliography

Akbarzadeh K, Bressler DC, Wang J, Gawrys KL, Gray MR, Kilpatrick PK, et al. Association behavior of pyrene compounds as models for asphaltenes. Energy and Fuels 2005;19:1268–71. doi:10.1021/ef0496698.

Bae S, Lee Y, Sharma BK, Lee H, Kim J, Ahn J. Graphene-based transparent strain sensor. Carbon N Y 2013;51:236–42. doi:10.1016/j.carbon.2012.08.048.

Bay Carbon Inc., SP-1 Graphite Powder http://www.baycarbon.com/SP1Summary.htm.

Bharadwaj RK. Modeling the barrier properties of polymer-layered silicate nanocomposites. Macromolecules 2001;34:9189–92. doi:10.1021/ma010780b.

Bi H, Xie X, Yin K, Zhou Y, Wan S, He L, et al. Spongy graphene as a highly efficient and recyclable sorbent for oils and organic solvents. Adv Funct Mater 2012;22:4421–5. doi:10.1002/adfm.201200888.

Bi H, Xie X, Yin K, Zhou Y, Wan S, Ruoff RS, et al. Highly enhanced performance of spongy graphene as an oil sorbent. J Mater Chem A 2014;2:1652–6. doi:10.1039/C3TA14112H.

Blanco-Fuente H, Anguiano-Igea S, Otero-Espinar FJ, Blanco-Méndez J. Kinetics of anhydride formation in xerogels of poly(acrylic acid). Biomaterials 1996;17:1667–75. doi:10.1016/0142-9612(96)87646-0.

Börner HG, Kühnle H, Hentschel J. Making “smart polymers” smarter: modern concepts to regulate functions in polymer science. J Polym Sci Part A Polym Chem 2010;48:1–14. doi:10.1002/pola.23727.

Bourlinos AB, Gournis D, Petridis D, Szabó T, Szeri A, Dékány I. Graphite Oxide: Chemical Reduction to Graphite and Surface Modification with Primary Aliphatic Amines and Amino Acids. Langmuir 2003;19:6050–5. doi:10.1021/la026525h.

Burattini S, Greenland BW, Merino DH, Weng W, Seppala J, Colquhoun HM, et al. A healable supramolecular polymer blend based on aromatic π-π Stacking and hydrogen-bonding interactions. J Am Chem Soc 2010;132:12051–8. doi:10.1021/ja104446r.

Burnside SD, Giannelis EP. Synthesis and properties of new poly(dimethylsiloxane) nanocomposites. Chem Mater 1995;7:1597–600. doi:10.1021/cm00057a001.

Burnworth M, Tang L, Kumpfer JR, Duncan AJ, Beyer FL, Fiore GL, et al. Optically healable supramolecular polymers. Nature 2011;472:334–7. doi:10.1038/nature09963.

Cabane E, Zhang X, Langowska K, Palivan CG, Meier W. Stimuli-responsive polymers and their applications in nanomedicine. Biointerphases 2012;7:1–27. doi:10.1007/s13758-011-0009-3.

Camenzind A, Schweizer T, Sztucki M, Pratsinis SE. Structure & strength of silica-PDMS nanocomposites. Polymer (Guildf) 2010;51:1796–804. doi:10.1016/j.polymer.2010.02.030.

Carvalho SP, Lucas EF, González G, Spinelli LS. Determining Hildebrand Solubility Parameter by Ultraviolet Spectroscopy and Microcalorimetry. J Braz Chem Soc 2013;24:1998–2007. doi:10.5935/0103-5053.20130250.

Chabot V, Higgins D, Yu A, Xiao X, Chen Z, Zhang J. A review of graphene and graphene oxide sponge: material synthesis and applications to energy and the environment. Energy Environ Sci 2014;7:1564. doi:10.1039/c3ee43385d.

Chen D, Yoon J, Chandra D, Crosby AJ, Hayward RC. Stimuli-Responsive Buckling Mechanics of Polymer Films. J Polym Sci Part B Polym Phys 2014;52:1441–61. doi:10.1002/polb.23590.

Chiou K-C, Chang F-C. Reactive compatibilization of polyamide-6 (PA 6)/polybutylene terephthalate (PBT) blends by a multifunctional epoxy resin. J Polym Sci Part B Polym Phys 2000;38:23–33. doi:10.1002/(SICI)1099-0488(20000101)38:1<23::AID-POLB3>3.0.CO;2-Y.

Choi K, Nam S, Lee Y, Lee M, Jang J, Kim SJ, et al. Reduced Water Vapor Transmission Rate of Graphene Gas Barrier Films for Flexible Organic Field-Effect Transistors. ACS Nano 2015;9:5818–24. doi:10.1021/acsnano.5b01161.

Choi M-C, Kim Y, Ha C-S. Polymers for flexible displays: From material selection to device applications. Prog Polym Sci 2008;33:581–630. doi:10.1016/j.progpolymsci.2007.11.004.

Cholake S, Mada M, Raman R, Bai Y, Zhao X, Rizkalla S, et al. Quantitative Analysis of Curing Mechanisms of Epoxy Resin by Mid- and Near- Fourier Transform Infra Red Spectroscopy. Def Sci J 2014;64:314–21. doi:10.14429/dsj.64.7326.

Choudalakis G, Gotsis AD. Permeability of polymer/clay nanocomposites: A review. Eur Polym J 2009;45:967–84. doi:10.1016/j.eurpolymj.2009.01.027.

Clarizia G, Algieri C, Drioli E. Filler-polymer combination: a route to modify gas transport properties of a polymeric membrane. Polymer (Guildf) 2004;45:5671–81. doi:10.1016/j.polymer.2004.06.001.

Compton OC, Kim S, Pierre C, Torkelson JM, Nguyen ST. Crumpled graphene nanosheets as highly effective barrier property enhancers. Adv Mater 2010;22:4759–63. doi:10.1002/adma.201000960.

Cordier P, Tournilhac F, Soulié-Ziakovic C, Leibler L. Self-healing and thermoreversible rubber from supramolecular assembly. Nature 2008;451:977–80. doi:10.1038/nature06669.

Cui Y, Kundalwal SI, Kumar S. Gas barrier performance of graphene/polymer nanocomposites. Carbon N Y 2016;98:313–33. doi:10.1016/j.carbon.2015.11.018.

Cussler EL, Hughes SE, Ward WJ, Aris R. Barrier membranes. J Memb Sci 1988;38:161–74. doi:10.1016/S0376-7388(00)80877-7.

De Greef TF a., Kade MJ, Feldman KE, Kramer EJ, Hawker CJ, Meijer EW. Spacer-length-dependent association in polymers with multiple-hydrogen-bonded end groups. J Polym Sci Part A Polym Chem 2011;49:4253–60. doi:10.1002/pola.24868.

Decker JJ, Meyers KP, Paul DR, Schiraldi DA, Hiltner A, Nazarenko S. Polyethylene-based nanocomposites containing organoclay: A new approach to enhance gas barrier via multilayer coextrusion and interdiffusion. Polymer (Guildf) 2015;61:42–54. doi:10.1016/j.polymer.2015.01.061.

Dikin DA, Stankovich S, Zimney EJ, Piner RD, Dommett GHB, Evmenenko G, et al. Preparation and characterization of graphene oxide paper. Nature 2007;448:457–60. doi:10.1038/nature06016.

Dong J, Ozaki Y, Nakashima K. Infrared, Raman, and Near-Infrared Spectroscopic Evidence for the Coexistence of Various Hydrogen-Bond Forms in Poly(acrylic acid). Macromolecules 1997;30:1111–7. doi:10.1021/ma960693x.

Dreyer DR, Park S, Bielawski CW, Ruoff RS. The chemistry of graphene oxide. Chem Soc Rev 2010;39:228–40. doi:10.1039/b920539j.

Du P, Lin X, Zhang X. Tunable electrical and mechanical responses of PDMS and polypyrrole nanowire composites. J Phys D Appl Phys 2013;46:195303. doi:10.1088/0022-3727/46/19/195303.

Efimenko K, Wallace WE, Genzer J. Surface Modification of Sylgard-184 Poly(dimethyl siloxane) Networks by Ultraviolet and Ultraviolet/Ozone Treatment. J Colloid Interface Sci 2002;254:306–15. doi:10.1006/jcis.2002.8594.

Faghihi S, Gheysour M, Karimi A, Salarian R. Fabrication and mechanical characterization of graphene oxide-reinforced poly (acrylic acid)/gelatin composite hydrogels. J Appl Phys 2014;115. doi:10.1063/1.4864153.

Feldman KE, Kade MJ, De Greef TF a, Meijer EW, Kramer EJ, Hawker CJ. Polymers with multiple hydrogen-bonded end groups and their blends. Macromolecules 2008;41:4694–700. doi:10.1021/ma800375r.

Feldman KE, Kade MJ, Meijer EW, Hawker CJ, Kramer EJ. Phase behavior of complementary multiply hydrogen bonded end-functional polymer blends. Macromolecules 2010;43:5121–7. doi:10.1021/ma1003776.

Freeman BD, Pinnau I. Separation of gases using solubility-selective polymers. Trends Polym Sci 1997;5:167–73.

Geim AK, Novoselov KS. The rise of graphene. Nat Mater 2007:183–91. doi:http://dx.doi.org/10.1038/nmat1849.

Ghosal K, Freeman BD. Gas separation using polymer membranes: An overview. Polym Adv Technol 1994;5:673–97. doi:10.1002/pat.1994.220051102.

Gomez De Arco L, Zhang Y, Schlenker CW, Ryu K, Thompson ME, Zhou C. Continuous, highly flexible, and transparent graphene films by chemical vapor deposition for organic photovoltaics. ACS Nano 2010;4:2865–73. doi:10.1021/nn901587x.

Grimme S. Do special noncovalent pi-pi stacking interactions really exist? Angew Chemie - Int Ed 2008;47:3430–4. doi:10.1002/anie.200705157.

Ha H, Park J, Ha K, Freeman BD, Ellison CJ. Synthesis and gas permeability of highly elastic poly(dimethylsiloxane)/graphene oxide composite elastomers using telechelic polymers. Polymer (Guildf) 2016;93:53–60. doi:10.1016/j.polymer.2016.04.016.

Ha H, Shanmuganathan K, Ellison CJ. Mechanically Stable Thermally Crosslinked Poly(acrylic acid)/Reduced Graphene Oxide Aerogels. ACS Appl Mater Interfaces 2015;7:6220–9. doi:10.1021/acsami.5b00407.

Ha H, Shanmuganathan K, Fei Y, Ellison CJ. Thermal stimuli-responsive behavior of pyrene end-functionalized PDMS through tunable Π-Π interactions. J Polym Sci Part B Polym Phys 2016;54:159–68. doi:10.1002/polb.23805.

Hong J-Y, Bak BM, Wie JJ, Kong J, Park HS. Reversibly Compressible, Highly Elastic, and Durable Graphene Aerogels for Energy Storage Devices under Limiting Conditions. Adv Funct Mater 2014:n/a – n/a. doi:10.1002/adfm.201403273.

Hu H, Zhao Z, Wan W, Gogotsi Y, Qiu J. Ultralight and highly compressible graphene aerogels. Adv Mater 2013;25:2219–23. doi:10.1002/adma.201204530.

Huang H, Ying Y, Peng X. Graphene oxide nanosheet: an emerging star material for novel separation membranes. J Mater Chem A 2014;2:13772. doi:10.1039/C4TA02359E.

Huang HD, Ren PG, Chen J, Zhang WQ, Ji X, Li ZM. High barrier graphene oxide nanosheet/poly(vinyl alcohol) nanocomposite films. J Memb Sci 2012;409-410:156–63. doi:10.1016/j.memsci.2012.03.051.

Huang HD, Ren PG, Xu JZ, Xu L, Zhong GJ, Hsiao BS, et al. Improved barrier properties of poly(lactic acid) with randomly dispersed graphene oxide nanosheets. J Memb Sci 2014;464:110–8. doi:10.1016/j.memsci.2014.04.009.

Huang Y, Zeng M, Ren J, Wang J, Fan L, Xu Q. Preparation and swelling properties of graphene oxide/poly(acrylic acid-co-acrylamide) super-absorbent hydrogel nanocomposites. Colloids Surfaces A Physicochem Eng Asp 2012;401:97–106. doi:10.1016/j.colsurfa.2012.03.031.

Hummers WS, Offeman RE. Preparation of Graphitic Oxide. J Am Chem Soc 1958;80:1339–1339. doi:10.1021/ja01539a017.

Hung W, Tsou C, De Guzman M, An Q, Liu Y, Zhang Y, et al. Cross-Linking with Diamine Monomers To Prepare Composite Graphene Oxide-Framework Membranes with Varying d -Spacing. Chem Mater 2014;26:2983–90. doi:10.1021/cm5007873.

Jones B a., Torkelson JM. Large melting point depression of 2-3-nm length-scale nanocrystals formed by the self-assembly of an associative polymer: Telechelic, pyrene-labeled poly(dimethylsiloxane). J Polym Sci Part B Polym Phys 2004;42:3470–5. doi:10.1002/polb.20228.

Jones BA, Torkelson JM. Crystallization and Enthalpy Relaxation of Physically Associating, End-Linked Polymer Networks: Telechelic Pyrene-Labeled Polydimethylsiloxane. Polym Bull 2004;51:411–8. doi:10.1007/s00289-004-0241-9.

Kalaitzidou K, Fukushima H, Drzal LT. Multifunctional polypropylene composites produced by incorporation of exfoliated graphite nanoplatelets. Carbon N Y 2007;45:1446–52. doi:10.1016/j.carbon.2007.03.029.

Kang D-W, Shin H-S. Control of size and physical properties of graphene oxide by changing the oxidation temperature. Carbon Lett 2012;13:39–43. doi:10.5714/CL.2012.13.1.039.

Karunakaran M, Shevate R, Kumar M, Peinemann K-V. CO2 -selective PEO–PBT (PolyActiveTM)/graphene oxide composite membranes. Chem Commun 2015;51:14187–90. doi:10.1039/C5CC04999G.

Khan AL, Klaysom C, Gahlaut A, Khan AU, Vankelecom IFJ. Mixed matrix membranes comprising of Matrimid and -SO3H functionalized mesoporous MCM-41 for gas separation. J Memb Sci 2013;447:73–9. doi:10.1016/j.memsci.2013.07.011.

Kim H, Abdala A a., Macosko CW. Graphene/polymer nanocomposites. Macromolecules 2010;43:6515–30. doi:10.1021/ma100572e.

Kim H, Macosko CW. Morphology and Properties of Polyester/Exfoliated Graphite Nanocomposites. Macromolecules 2008;41:3317–27. doi:10.1021/ma702385h.

Kim H, Macosko CW. Processing-property relationships of polycarbonate/graphene composites. Polymer (Guildf) 2009;50:3797–809. doi:10.1016/j.polymer.2009.05.038.

Kim H, Miura Y, MacOsko CW. Graphene/polyurethane nanocomposites for improved gas barrier and electrical conductivity. Chem Mater 2010;22:3441–50. doi:10.1021/cm100477v.

Kim KS, Zhao Y, Jang H, Lee SY, Kim JM, Kim KS, et al. Large-scale pattern growth of graphene films for stretchable transparent electrodes. Nature 2009;457:706–10. doi:10.1038/nature07719.

Kim SD, Torkelson JM. Nanoscale confinement and temperature effects on associative polymers in thin films: Fluorescence study of a telechelic, pyrene-labeled poly(dimethylsiloxane). Macromolecules 2002;35:5943–52. doi:10.1021/ma0200322.

Kovtyukhova NI, Ollivier PJ, Martin BR, Mallouk TE, Chizhik SA, Buzaneva E V, et al. Layer-by-Layer Assembly of Ultrathin Composite Films from Micron-Sized Graphite Oxide Sheets and Polycations. Chem Mater 1999;11:771–8. doi:10.1021/cm981085u.

La Y-H, Edwards EW, Park S-M, Nealey PF. Directed Assembly of Cylinder-Forming Block Copolymer Films and Thermochemically Induced Cylinder to Sphere Transition: A Hierarchical Route to Linear Arrays of Nanodots. Nano Lett 2005;5:1379–84. doi:10.1021/nl0506913.

Lamberti A, Di Donato M, Chiappone A, Giorgis F, Canavese G. Tunable electromechanical actuation in silicone dielectric film. Smart Mater Struct 2014;23:105001. doi:10.1088/0964-1726/23/10/105001.

Lape NK, Nuxoll EE, Cussler EL. Polydisperse flakes in barrier films. J Memb Sci 2004;236:29–37. doi:10.1016/j.memsci.2003.12.026.

Lee S, Lee H, Sim JH, Sohn D. Graphene oxide/poly(acrylic acid) hydrogel by ??-ray pre-irradiation on graphene oxide surface. Macromol Res 2014;22:165–72. doi:10.1007/s13233-014-2025-x.

LeVier RR, Lane TH, Harrison MC, Cook RR. What is silicone? J Clin Epidemiol 1995;48:513–7. doi:10.1016/0895-4356(94)00207-7.

Li M-C, Ho R-M, Lee Y-D. Photo-induced excimer formation of pyrene-labeled polymers for optical recording. J Mater Chem 2011;21:2451. doi:10.1039/c0jm03543b.

Li R, Chen C, Li J, Xu L, Xiao G, Yan D. A facile approach to superhydrophobic and superoleophilic graphene/polymer aerogels. J Mater Chem A 2014;2:3057. doi:10.1039/c3ta14262k.

Li X, Ma L, Zhang H, Wang S, Jiang Z, Guo R, et al. Synergistic effect of combining carbon nanotubes and graphene oxide in mixed matrix membranes for efficient CO2 separation. J Memb Sci 2015;479:1–10. doi:10.1016/j.memsci.2015.01.014.

Lin P, Ma S, Wang X, Zhou F. Molecularly Engineered Dual-Crosslinked Hydrogel with Ultrahigh Mechanical Strength, Toughness, and Good Self-Recovery. Adv Mater 2015;27:2054–9. doi:10.1002/adma.201405022.

Liu H, Kuila T, Kim NH, Ku B-C, Lee JH. In situ synthesis of the reduced graphene oxide–polyethyleneimine composite and its gas barrier properties. J Mater Chem A 2013;1:3739. doi:10.1039/c3ta01228j.

Ma P-C, Siddiqui NA, Marom G, Kim J-K. Dispersion and functionalization of carbon nanotubes for polymer-based nanocomposites: A review. Compos Part A Appl Sci Manuf 2010;41:1345–67. doi:10.1016/j.compositesa.2010.07.003.

Martinez CR, Iverson BL. Rethinking the term "pi-stacking." Chem Sci 2012;3:2191. doi:10.1039/c2sc20045g.

Merkel TC, Bondar VI, Nagai K, Freeman BD, Pinnau I. Gas sorption, diffusion, and permeation in poly(dimethylsiloxane). J Polym Sci Part B Polym Phys 2000;38:415–34. doi:10.1002/(SICI)1099-0488(20000201)38:3<415::AID-POLB8>3.0.CO;2-Z.

Merkel TC, Lin H, Wei X, Baker R. Power plant post-combustion carbon dioxide capture: An opportunity for membranes. J Memb Sci 2010;359:126–39. doi:10.1016/j.memsci.2009.10.041.

Nardecchia S, Carriazo D, Ferrer ML, Gutiérrez MC, del Monte F. Three dimensional macroporous architectures and aerogels built of carbon nanotubes and/or graphene: synthesis and applications. Chem Soc Rev 2013;42:794–830. doi:10.1039/c2cs35353a.

Nawaz K, Khan U, Ul-Haq N, May P, O'Neill A, Coleman JN. Observation of mechanical percolation in functionalized graphene oxide/elastomer composites. Carbon N Y 2012;50:4489–94. doi:10.1016/j.carbon.2012.05.029.

Nollet JA. Investigations on the causes for the ebullition of liquids. J Memb Sci 1995;100:1–3. doi:10.1016/0376-7388(94)00224-M.

Novoselov KS, Geim AK, Morozov S V, Jiang D, Zhang Y, Dubonos S V, et al. Electric field effect in atomically thin carbon films. Science 2004;306:666–9. doi:10.1126/science.1102896.

Osman M a., Mittal V, Morbidelli M, Suter UW. Polyurethane adhesive nanocomposites as gas permeation barrier. Macromolecules 2003;36:9851–8. doi:10.1021/ma035077x.

Ozbas B, O'Neill CD, Register R a., Aksay I a., Prud'Homme RK, Adamson DH. Multifunctional elastomer nanocomposites with functionalized graphene single sheets. J Polym Sci Part B Polym Phys 2012;50:910–6. doi:10.1002/polb.23080.

Park S, Dikin D a., Nguyen ST, Ruoff RS. Graphene oxide sheets chemically cross-linked by polyallylamine. J Phys Chem C 2009;113:15801–4. doi:10.1021/jp907613s.

Parviz D, Das S, Ahmed HST, Irin F, Bhattacharia S, Green MJ. Dispersions of non-covalently functionalized graphene with minimal stabilizer. ACS Nano 2012;6:8857–67. doi:10.1021/nn302784m.

Parviz D, Yu Z, Hedden RC, Green MJ. Designer stabilizer for preparation of pristine graphene/polysiloxane films and networks. Nanoscale 2014;6:11722–31. doi:10.1039/C4NR01431F.

Paul DR, Mark JE. Fillers for polysiloxane ("silicone") elastomers. Prog Polym Sci 2010;35:893–901. doi:10.1016/j.progpolymsci.2010.03.004.

Paul DR, Robeson LM. Polymer nanotechnology: Nanocomposites. Polymer (Guildf) 2008;49:3187–204. doi:10.1016/j.polymer.2008.04.017.

Pei S, Zhao J, Du J, Ren W, Cheng HM. Direct reduction of graphene oxide films into highly conductive and flexible graphene films by hydrohalic acids. Carbon N Y 2010;48:4466–74. doi:10.1016/j.carbon.2010.08.006.

Potts JR, Dreyer DR, Bielawski CW, Ruoff RS. Graphene-based polymer nanocomposites. Polymer (Guildf) 2011;52:5–25. doi:10.1016/j.polymer.2010.11.042.

Prime RB, Sacher E. Kinetics of epoxy cure: 2. The system bisphenol-A diglycidyl ether/polyamide. Polymer (Guildf) 1972;13:455–8. doi:10.1016/0032-3861(72)90113-9.

Qiu L, Liu D, Wang Y, Cheng C, Zhou K, Ding J, et al. Mechanically Robust, Electrically Conductive and Stimuli-Responsive Binary Network Hydrogels Enabled by Superelastic Graphene Aerogels. Adv Mater 2014;26:3333–7. doi:10.1002/adma.201305359.

Qiu L, Liu JZ, Chang SLY, Wu Y, Li D. Biomimetic superelastic graphene-based cellular monoliths. Nat Commun 2012;3:1241. doi:10.1038/ncomms2251.

Reid BD, Ruiz-Trevino FA, Musselman IH, Balkus KJ, Ferraris JP. Gas Permeability Properties of Polysulfone Membranes Containing the Mesoporous Molecular Sieve MCM-41. Chem Mater 2001;13:2366–73. doi:10.1021/cm000931+.

Robeson LM. The upper bound revisited. J Memb Sci 2008;320:390–400. doi:10.1016/j.memsci.2008.04.030.

Roth M. Solubility parameter of poly(dimethyl siloxane) as a function of temperature and chain length. J Polym Sci Part B Polym Phys 1990;28:2715–9. doi:10.1002/polb.1990.090281317.

Ryu SH, Sin JH, Shanmugharaj AM. Study on the effect of hexamethylene diamine functionalized graphene oxide on the curing kinetics of epoxy nanocomposites. Eur Polym J 2014;52:88–97. doi:10.1016/j.eurpolymj.2013.12.014.

Sanders DF, Smith ZP, Guo R, Robeson LM, McGrath JE, Paul DR, et al. Energy-efficient polymeric gas separation membranes for a sustainable future: A review. Polym (United Kingdom) 2013;54:4729–61. doi:10.1016/j.polymer.2013.05.075.

Shen J, Liu G, Huang K, Jin W, Lee KR, Xu N. Membranes with fast and selective gas-transport channels of laminar graphene oxide for efficient CO2 capture. Angew Chemie - Int Ed 2015;54:578–82. doi:10.1002/anie.201409563.

Shen J, Yan B, Li T, Long Y, Li N, Ye M. Mechanical, thermal and swelling properties of poly(acrylic acid)–graphene oxide composite hydrogels. Soft Matter 2012;8:1831. doi:10.1039/c1sm06970e.

Silicone Rubber Chemical Crosslinking Principle http://www.wacker.com/cms/en/products/product_groups/silicone_rubbers_1/vernetzung_1.jsp.

Smith ZP, Freeman BD. Graphene oxide: A new platform for high-performance gas- and liquid-separation membranes. Angew Chemie - Int Ed 2014;53:10286–8. doi:10.1002/anie.201404407.

Stankovich S, Dikin D a., Piner RD, Kohlhaas K a., Kleinhammes A, Jia Y, et al. Synthesis of graphene-based nanosheets via chemical reduction of exfoliated graphite oxide. Carbon N Y 2007;45:1558–65. doi:10.1016/j.carbon.2007.02.034.

Sun H, Xu Z, Gao C. Multifunctional, Ultra-Flyweight, Synergistically Assembled Carbon Aerogels. Adv Mater 2013;25:2554–60. doi:10.1002/adma.201204576.

Sun J-Y, Zhao X, Illeperuma WRK, Chaudhuri O, Oh KH, Mooney DJ, et al. Highly stretchable and tough hydrogels. Nature 2012;489:133–6. doi:10.1038/nature11409.

Sun S, Wu P. A one-step strategy for thermal- and pH-responsive graphene oxide interpenetrating polymer hydrogel networks. J Mater Chem 2011;21:4095. doi:10.1039/c1jm10276a.

Vu DQ, Koros WJ, Miller SJ. Mixed matrix membranes using carbon molecular sieves. J Memb Sci 2003;211:311–34. doi:10.1016/S0376-7388(02)00429-5.

Wang Y, Wang L, Yang T, Li X, Zang X, Zhu M, et al. Wearable and Highly Sensitive Graphene Strain Sensors for Human Motion Monitoring. Adv Funct Mater 2014;24:4666–70. doi:10.1002/adfm.201400379.

Wang Y, Yadav S, Heinlein T, Konjik V, Breitzke H, Buntkowsky G, et al. Ultra-light nanocomposite aerogels of bacterial cellulose and reduced graphene oxide for specific absorption and separation of organic liquids. RSC Adv 2014;4:21553. doi:10.1039/c4ra02168a.

Wang Z, Nelson JK, Hillborg H, Zhao S, Schadler LS. Graphene oxide filled nanocomposite with novel electrical and dielectric properties. Adv Mater 2012;24:3134–7. doi:10.1002/adma.201200827.

Waqas Anjum M, de Clippel F, Didden J, Laeeq Khan A, Couck S, Baron G V., et al. Polyimide mixed matrix membranes for CO2 separations using carbon–silica

nanocomposite fillers. J Memb Sci 2015;495:121–9. doi:10.1016/j.memsci.2015.08.006.

White EM, Yatvin J, Grubbs JB, Bilbrey J a., Locklin J. Advances in smart materials: Stimuli-responsive hydrogel thin films. J Polym Sci Part B Polym Phys 2013;51:1084–99. doi:10.1002/polb.23312.

Wojtecki RJ, Meador M a, Rowan SJ. Using the dynamic bond to access macroscopically responsive structurally dynamic polymers. Nat Mater 2011;10:14–27. doi:10.1038/nmat2891.

Yang C-C, Hsu Y-L. A Review of Accelerometry-Based Wearable Motion Detectors for Physical Activity Monitoring. Sensors 2010;10:7772–88. doi:10.3390/s100807772.

Yang D, Velamakanni A, Bozoklu G, Park S, Stoller M, Piner RD, et al. Chemical analysis of graphene oxide films after heat and chemical treatments by X-ray photoelectron and Micro-Raman spectroscopy. Carbon N Y 2009;47:145–52. doi:10.1016/j.carbon.2008.09.045.

Yang J, Wei D, Tang L, Song X, Luo W, Chu J, et al. Wearable temperature sensor based on graphene nanowalls. RSC Adv 2015;5:25609–15. doi:10.1039/C5RA00871A.

Yoo BM, Shin HJ, Yoon HW, Park HB. Graphene and graphene oxide and their uses in barrier polymers. J Appl Polym Sci 2014;131:39628. doi:10.1002/app.39628.

Yu Y-H, Lin Y-Y, Lin C-H, Chan C-C, Huang Y-C. High-performance polystyrene/graphene-based nanocomposites with excellent anti-corrosion properties. Polym Chem 2014;5:535–50. doi:10.1039/C3PY00825H.

Zang J, Ryu S, Pugno N, Wang Q, Tu Q, Buehler MJ, et al. Multifunctionality and control of the crumpling and unfolding of large-area graphene. Nat Mater 2013;12:321–5. doi:10.1038/nmat3542.

Zeng W, Shu L, Li Q, Chen S, Wang F, Tao X-M. Fiber-Based Wearable Electronics: A Review of Materials, Fabrication, Devices, and Applications. Adv Mater 2014;26:5310–36. doi:10.1002/adma.201400633.

Zhang J, Yang H, Shen G, Cheng P, Zhang J, Guo S. Reduction of graphene oxide via L-ascorbic acid. Chem Commun (Camb) 2010;46:1112–4. doi:10.1039/b917705a.

Zhang Y, Liu C, Shi W, Wang Z, Dai L, Zhang X. Direct measurements of the interaction between pyrene and graphite in aqueous media by single molecule force spectroscopy: Understanding the π-π interactions. Langmuir 2007;23:7911–5. doi:10.1021/la700876d.

Zhang Y, Yuan S, Zhou W, Xu J, Li Y. Spectroscopic evidence and molecular simulation investigation of the pi-pi interaction between pyrene molecules and carbon nanotubes. J Nanosci Nanotechnol 2007;7:2366–75. doi:10.1166/jnn.2007.412.

Zhu J, Lim J, Lee CH, Joh HI, Kim HC, Park B, et al. Multifunctional polyimide/graphene oxide composites via in situ polymerization. J Appl Polym Sci 2014;131:1–7. doi:10.1002/app.40177.

Zurutuza A, Marinelli C. Challenges and opportunities in graphene commercialization. Nat Nanotechnol 2014;9:730–4. doi:10.1038/nnano.2014.225.